POLITECNICO DI TORINO

Master of Science in Automotive Engineering

EXPERIMENTAL AND NUMERICAL ANALYSIS OF LIGHT-EMITTING DIODE (LED) HEADLAMP

Politecnico supervisor:

Prof. Anna Pellegrino

Windsor supervisors:

Dr. Vesselina Roussinova

Dr. Majed Etemadi

Candidate:

Yuan Fang

March 2025

ABSTRACT

Light-emitting diodes (LEDs) have become the preferred light source for automotive headlamps due to their excellent durability, fast response times, higher efficiency, and superior optical performance compared to traditional halogen bulbs. However, their high power output, compact design, and positioning within the headlamp assembly pose significant thermal management challenges. Prolonged operation leads to a rise in LED temperature, resulting in reduced light output—a phenomenon known as LED derating. This decrease in light output can compromise visibility, posing safety risks to drivers and road users. Additionally, the proximity of the headlamp to the vehicle's engine further elevates the surrounding temperature, worsening the LED derating. This thesis investigates the thermal and optical performance of LED headlamp under various ambient conditions and LED current control methods, including convective fan cooling and forced current derating. Experimental temperature measurements at 14 locations, along with luminous flux measurements of a headlamp model, were conducted at the Stellantis Automotive Research and Development Center (ARDC). In parallel, a computational fluid dynamics (CFD) model of a simplified LED headlamp assembly was analyzed to evaluate temperature distributions on the LEDs and the detailed flow patterns within the headlamp. The CFD results align within ±10% of the quasi-steady temperature measurements obtained for forced convection cases. The CFD analysis reveals that the flow around the LED heatsinks is significantly influenced by the position of the cooling fan. Furthermore, internal components within the headlamp obstruct the flow, creating a stagnation zone near the second LED unit. This stagnation zone results in elevated temperature distributions, indicating a potential hotspot in the system that could impact performance and reliability.

TABLE OF CONTENTS

LIST OF TABLES

LIST OF FIGURES

LIST OF ABBREVIATIONS/SYMBOLS

CAD	Computer Aided Design
CAE	Computer Aided Engineering
CFD	Computational Fluid Dynamics
EPF	Expanded Polystyrene Foam
LED	Light Emitting Diode
FMVSS	Federal Motor Vehicle Safety Standards
HB	High Beam Light
HID	High-Intensity Discharge
IIHS	Insurance Institute for Highway Safety
LB	Low Beam Light
LB1	Low Beam No.1
LB2	Low Beam No.2
NTC	Negative Temperature Coefficient
PCB	Printed Circuit Board
PID	Property Identification
PMMA	Polymethylmethacrylate
SAE	Society of Automotive Engineering

SLM	Smart Lighting Module
β	Coefficient of thermal expansion (1/K)
C_p	Specific heat capacity [J/kg·K]
Gr	Grashof number
k	Thermal conductivity [W/m·K]
K_{max}	Maximum Spectral Luminous Efficacy of Radiation for Photopic Vision
L	Characteristic Length [m]
μ	Dynamic viscosity [kg/ms]
Nu	Nusselt number
p	Pressure [kPa]
$P_{electrical}$	Electrical Power [W]
$P_{heating}$	Heating Power [W]
$P_{optical}$	Optical Power [W]
$P_{opt,\lambda}$	Spectral Optical Power at Wavelength λ (W/nm)
$P_{opt,rel,\lambda}$	Relative Spectral Power Distribution
Q	Heat Dissipation (J)

Ra	Rayleigh number
Re	Reynolds number
Ri	Richardson number
ρ	Density [kg/m^3]
T_{front}	Temperature at front chamber [°C]
T_j	LED Junction Temperature [°C]
T_{rear}	Temperature at rear chamber [°C]
υ	Kinematic viscosity [m^2/s]
$V(\lambda)$	Spectral Luminous Efficiency Function
λ	Wavelength (nm)
ϕ	Luminous flux (lm)
ε	Emissivity

CHAPTER 1 INTRODUCTION

This chapter explores the significance of light-emitting diode (LED) headlamps and the critical role of effective thermal management in LED performance. It examines the thermal transfer pathways within LED systems and highlights the challenges involved in maintaining optimal performance and reliability. Additionally, this chapter outlines the objectives of the research and provides an overview of the headlamp model used in the study.

1.1.Research Background

1.1.1 Light Emitting Diode (LED) Headlamp Overview

LEDs are the new generation of automotive light sources. They are widely used in automotive lighting systems due to their high efficiency, durability, compact size, and environmental benefits. Compared to halogen or high-intensity discharge (HID) systems, which typically achieve luminous efficacy of 20–50 lm/W, LEDs can reach up to 160 lm/W (Roberts, 2009). Additionally, LEDs have a much longer lifespan, up to 60,000 hours, making them cost-effective and reducing the environmental impact of frequent replacements. These advantages have made LEDs a preferred choice for automotive headlamps. A 2019 Consumer Reports study found that 86% of tested car models were equipped with LED headlights (Linkov, 2019).

The junction temperature (T_j), which refers to the temperature at the interface between the LED chip and its substrate, is critical for LED performance and reliability. T_j directly affects LED optical performance and lifespan. Exceeding the recommended T_j can accelerate light degradation, cause color shifts, and lead to LED failure. Typically, the absolute maximum rating of T_j on data sheets ranges from 125°C to 135°C (Chang et al., 2011). Maintaining the T_j below this limit is vital to ensure optimal performance and longevity.

Thermal management in automotive LED headlamps poses unique challenges. The compact design of headlamp assemblies, combined with their proximity to the engine compartment, results in elevated ambient temperatures. Under high-load conditions, heat from the engine can raise the headlamp rear housing temperature up to 105°C. Meanwhile, the front of the headlamp is exposed to external ambient air, which can vary depending on environmental conditions. This creates two distinct ambient environments for the headlamp: T_{front}, representing the external temperature at the front of the headlamp; T_{rear}, representing the temperature at the rear of the headlamp, which is under the hood, influenced by engine heat from multiple directions, including the top, sides, and rear.

Figure 1.1 provides a side-view schematic of the headlamp, highlighting T_{front} and T_{rear} as separate thermal environments divided by the vehicle's front fascia. These distinct environments are critical for effective thermal management of the headlamp system.

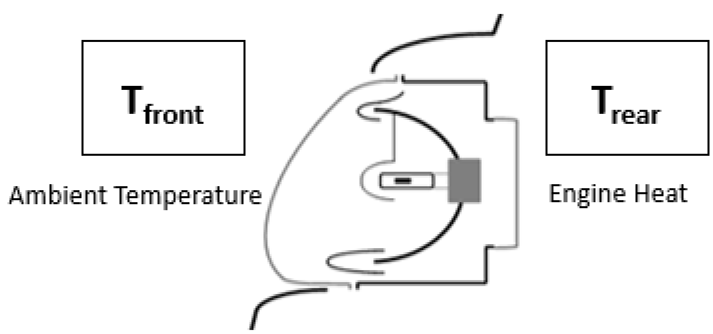

Figure 1.1 Schematic of the headlamp showing T_{front} /T_{rear} separated by the vehicle front fascia

For experimental testing and numerical simulation, four different ambient temperature settings for T_{front} /T_{rear} are applied to replicate real-world conditions and accurately assess thermal and optical performance of the LED headlamp.

The temperature conditions in this research are based on Stellantis-defined cases. Four T_{front} /T_{rear} scenarios are considered, ranging from room temperature to elevated temperature conditions:

- 20°C/20°C
- 50°C/50°C
- 50°C/85°C
- 50°C/105°C

High ambient temperatures, limited ventilation, and suboptimal headlamp cooling design can significantly reduce the LED's light output and lifespan. For instance, increasing the LED ambient temperature from 60°C to 70°C can reduce its lifespan from 40,000 to 17,500 hours (Roberts, 2009). To address these thermal challenges, various cooling methods are used to dissipate heat efficiently. Passive cooling solutions, such as heatsinks and heat pipes, are widely employed. Active cooling methods, including forced air and pumped liquid cooling, offer better performance but increase costs and energy consumption (Fan et al., 2012). When cooling systems fail to maintain the LED's temperature within its operating range, modern headlamps incorporate smart lighting modules (SLMs) to protect the LED. These modules monitor the T_j and regulate the input power to prevent T_j from exceeding safe limits. This protective mechanism is known as forced LED derating.

1.1.2 LED Derating

LED derating involves operating an LED below its maximum rated power to extend its lifespan, maintain reliability, and ensure consistent performance. This practice is necessary when the LED cannot dissipate heat effectively, causing T_j to exceed its maximum operating limit. Elevated T_j degrades LED optical performance and significantly shorten its lifespan.

LED derating can be categorized into two types: natural derating and forced derating.

Natural derating refers to the gradual decline in LED performance and efficiency over time due to physical and chemical changes during operation. This process typically occurs over thousands of hours but can be accelerated by high temperature condition. As the LED ages, its thermal efficiency decreases, light output diminishes, and color shifts occur, reducing its reliability.

Forced derating applies to high-power LEDs, such as low-beam (LB) and high-beam (HB) lights in automotive applications, to protect them from thermal damage. These LEDs are controlled by SLMs that monitor T_j and regulate the current or voltage supplied to the LED. If the T_j exceeds the safe operating range, SLM reduces input power to prevent overheating (Ribas, 2022). However, lowering the input power causes reduction in LED's light output, resulting illumination levels to fall below photometric standards, such as the Federal Motor Vehicle Safety Standards (FMVSS) and Insurance Institute for Highway Safety (IIHS) requirements.

1.1.3 Basic Principles of LED Heat Transfer

LEDs have high luminous efficacy, but their thermal efficiency is relatively low. Between 60% and 80% of the input electrical power is converted into heat rather than light (Lasance & Poppe, 2014). Figure 1.2(a) illustrates this division, where input power produces both light output and waste heat. The heat output is waste energy that can cause the LED to overheat if not effectively managed.

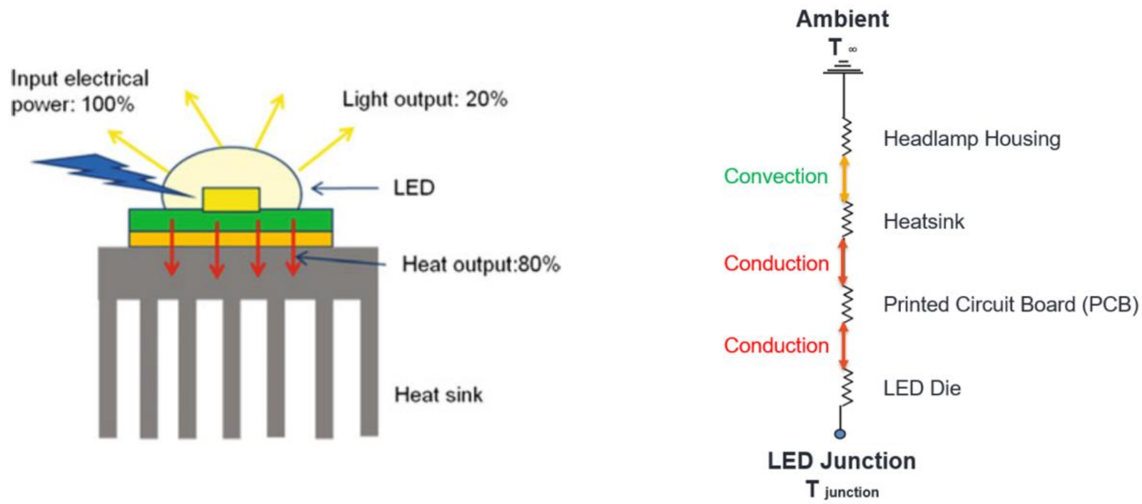

(a) (b)

Figure 1.2 (a) LED energy distribution in a LED (Lasance & Poppe, 2014) (b) LED thermal transfer path

Effective thermal management is critical for maintaining optimal LED performance. Figure 1.2(b) illustrates the typical thermal transfer path in an LED system. Thermal management focuses on three key components: the LED, the printed circuit board (PCB), and the cooling unit. The cooling unit typically includes conductive elements, such as heatsinks or heat pipes, and may also employ forced convection methods like fans or liquid cooling. Heat generated at the LED junction is transferred through the solder joints to the PCB, then to the heatsink, and finally dissipated into the surrounding environment.

1.2.Research Objectives

This research aims to investigate and analyze the optical and thermal behavior of LED headlamps under different temperature conditions and various thermal management methods, employing both experimental and numerical methodologies. The following sections outline the objectives for the experimental and numerical methodologies.

1.2.1 Experimental Objectives

The primary objective of experimental approach is to investigate the thermal and optical performance of the LED, under different ambient condition and thermal management methods. Using the experimental approach, key variables are controlled to measure LED, heatsink temperatures, and light output over time. These variables include:

- Number and position of LED units (LB1, LB2 and LB1+LB2)
- Different ambient temperature conditions (T_{front} / T_{rear})
- Natural / forced convection modes (cooling fan off / on)
- LED forced derating modes (natural / forced derating)

Based on the experiment data collected, comparative studies were conducted to evaluate the effects of ambient temperature, the number and position of LEDs and the effectiveness of various cooling methods.

The secondary objective is to collect experimental data for setup, calibration, and validation of numerical CFD models. This includes measuring the LED's optical power to calculate heating power and collecting quasi-steady-state data for LED and heatsink temperatures to validate simulation results.

To achieve these objectives, three categories of experiments were conducted:

- Heatsink temperature and light output measurement of the LED headlamp
- LED temperature measurement

- LED optical power measurement

1.2.2 Numerical Objectives

The numerical simulations aim to replicate the headlamp's operating conditions as the experimental approach and analyze the airflow behavior and temperature distribution within the headlamp. CFD simulations using STAR CCM+ software are performed under the same variables as the experiments:

- Different ambient temperature conditions (T_{front} / T_{rear})
- Natural / forced convection heat transfer modes (cooling fan off / on)

This numerical approach evaluates airflow velocity and direction within the headlamp, identifies flow stagnation zones and thermal hotspots, and assesses the impact of components such as the heatsink and cooling fan airflow distribution.

1.3.Headlamp Model

The headlamp model used in this study is the 2021 Jeep Grand Cherokee passenger-side headlamp. Figure 1.3 shows the front, top, right-side, and isometric views of the headlamp, along with its key dimensions. This model was selected due to its representative design and relevance to modern automotive headlamp systems.

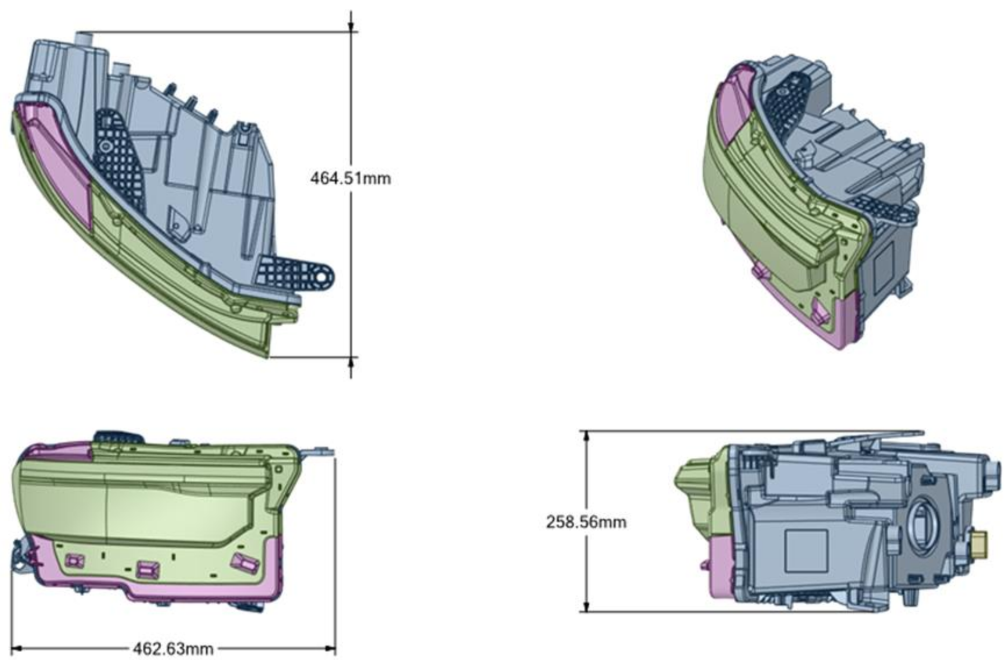

Figure 1.3 Dimensions and design layout of the 2021 Jeep Grand Cherokee headlamp

Table 1.1 provides the dimensions of key components relevant to LED thermal management, including the headlamp housing, heatsink, PCB, and LED. These dimensions give an overview of the physical scale of the headlamp and its components, helping to contextualize the thermal management challenges discussed in this study.

Table 1.1 Dimensions of the headlamp assembly, LED, PCB and heatsink

	Headlamp	Heatsink	PCB	LED
Length	464.5 mm	76 mm	51.8 mm	5 mm
Width	462.6 mm	60 mm	22 mm	3 mm
Height/Thickness	254.6 mm	50.5mm/2.5 mm	1.2 mm	0.84 mm

The headlamp assembly consists of multiple light sources, including the daytime running light (DRL), signal lights, LB lights, and HB lights. This study focuses specifically on the LB lights, which utilize high-power LEDs for illumination.

The key components associated with the LB lights include the LED assemblies, reflector, bezel, and cooling fan, as shown in Figure 1.4. The LB function is achieved using two identical LED assemblies, referred as LB1 and LB2 in this study. These LED assemblies are mounted on top of the reflector, adjacent to the HB LED assembly. Reflector reflects the LED light onto the road, ensuring proper beam patterns to meet the illumination requirements.

The bezel connects the internal components of the headlamp to the housing and aligns the light direction for optimal performance. Positioned beneath the LED assemblies and reflector, the cooling fan, with a blade diameter of 39 mm, generates upward airflow at a velocity of 3.56 m/s, cooling the LED assemblies.

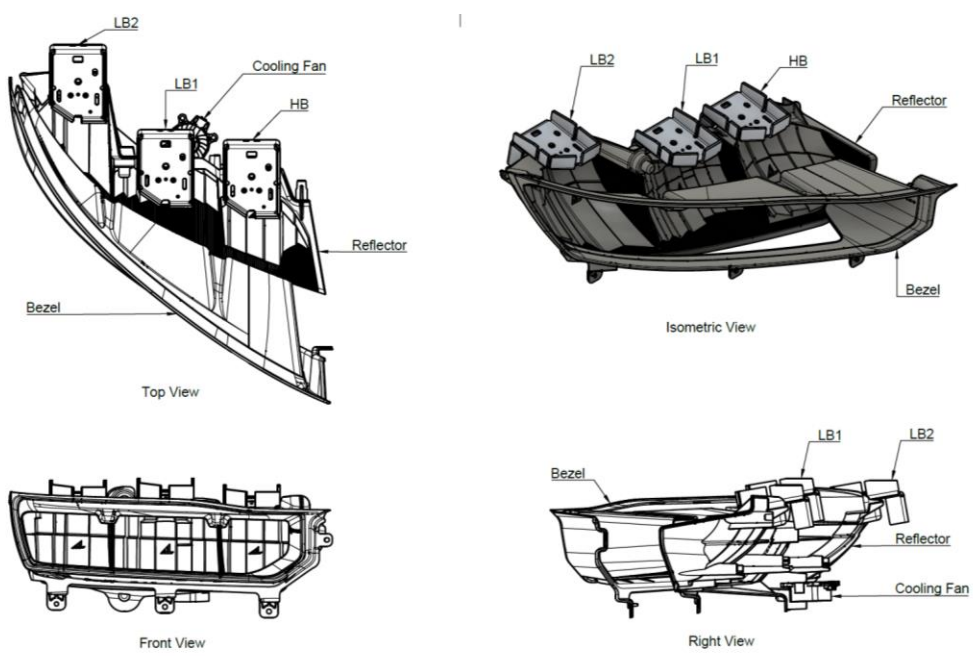

Figure 1.4 Drawing of key headlamp components, including three LED assemblies, reflector, bezel, and cooling fan

Figure 1.5 presents the drawing of the LB LED assembly, which includes the LED chip, PCB, and heatsink. The LED chip consists of four dies with a combined power of 13.1 W. The LED chip measures 5 mm (L) × 3 mm (W) × 0.84 mm (H). The PCB provides electrical connectivity and acts as a thermal interface, transferring heat generated from the LED to the heatsink. Both the LED and PCB are mounted on the lower horizontal surface of the heatsink.

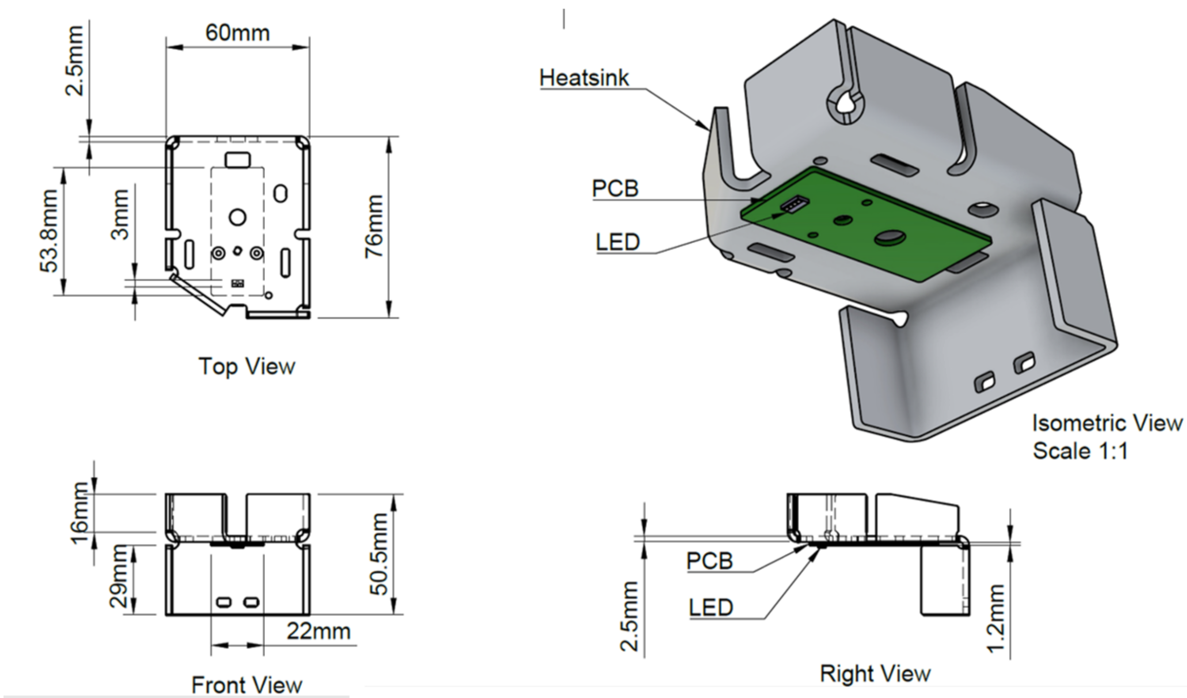

Figure 1.5 Drawing of LB LED assembly

CHAPTER 2 LITERATURE REVIEW

LED headlamp performance testing rely on two primary methodologies: physical experiments and numerical simulations. Each approach has distinct strengths and limitations in addressing the complexities of thermal management in LED headlamps.

Physical experimentation involves testing actual headlamp assemblies to assess performance under real-world conditions. This method ensures compliance with regulatory standards and verifies its performance in operational environments. However, physical testing is costly, time-consuming, and typically conducted during the later stages of design and development. It requires manufacturing prototypes, which are evaluated in vehicles or controlled chambers simulating environmental conditions such as different temperature. Thermal analysis in physical experiments is challenging due to limited access to the internal components of the headlamp for temperature and airflow measurements. Furthermore, applying and testing various LED cooling strategies can be labor-intensive and expensive, as each cooling methods often requires re-engineering and producing improved designs.

Numerical simulation, by contrast, is highly advantageous during the early stages of headlamp design. Simulations enable rapid iteration of design variations, detailed analysis of operating conditions, and generation of results such as flow fields and temperature distributions inside of the headlamp fluid domain. This approach is both cost-effective and efficient, enabling designers to evaluate headlamp performance before physical prototypes are built. Early identification of potential issues saves time and resources while offering insights into thermal and optical performance. However, simulation model must be calibrated and validated against experimental data to ensure accuracy and reliability, bridging the gap between numerical predictions and real-world performance.

This literature review examines key studies within these methodologies, focusing on experimental techniques and CFD models relevant to LED thermal analysis. It highlights the contributions and challenges of each approach while identifying current research gaps in the field.

2.1 Experimental Approach

Effective thermal management is a critical aspect of designing high-power LEDs due to the significant impact of junction temperature (T_j) on their performance, reliability, and lifespan (Van Driel et al., 2011). Liu et al. (2011) discovered that the conversion efficiency of electrical input power into light decreases as T_j rises. This inefficiency leads to an increase in heating power ($P_{heating}$), worsening the LED thermal management challenges.

Various cooling methods have been investigated to regulate T_j in high-power LEDs. Traditional approaches include natural or forced convection using cooling fan with heatsinks, heat pipes, and thermal conduction through components such as PCBs and solder layers with thermal interface materials. While advanced cooling systems, such as liquid-cooled plates and vapor chamber plates, offer improved heat dissipation, they are often complex, expensive, and less stable (Treurniet, 2014).

Ngo et al. (2018) conducted experiments using a custom test chamber equipped with thermocouples to investigate the impact of heatsink size, chamber configuration, and ambient temperature on T_j and thermal resistance. Their findings revealed that larger heatsinks significantly reduce both T_j and thermal resistance, thereby improving LED thermal performance and longevity. Additionally, they found that optimizing LED chamber configurations for airflow, such as removing the inner lens, increased the internal fluid volume, further enhanced cooling efficiency.

Wang et al., (2014) compared various cooling methods, including natural convection, heatsink, and a combined heatsinks with heat pipes. They found that natural convection alone was insufficient to maintain T_j within its safe limit when the ambient temperature reached 80°C. In contrast, combining heatsinks with heat pipes reduced LED temperature by approximately 50% compared to natural convection and 35% compared to standalone heatsinks. The study also emphasized that the heat pipe's liquid fill ratio significantly impacts the heat transfer coefficient, with an optimal fill ratio of 30%. Additionally, T_j showed a linear increase with LED input power and ambient temperature, highlighting the critical need for effective thermal management.

These experimental studies highlight the importance of optimizing cooling methods, heatsink design, and environmental conditions to mitigate thermal challenges in high-power LED applications.

2.2 Numerical Approach

Tang et al. (2019) utilized the finite element analysis (FEA) to investigate the effects of heatsink design on LED junction temperature (T_j). Their findings showed that heatsink spacing and fin height significantly influence thermal performance, with longer fins enhancing heat dissipation due to improved thermal conduction. Additionally, the researchers tested various heatsink and PCB substrate materials, concluding that high thermal conductivity materials are more effective in reducing LED temperatures. For example, copper has the thermal conductivity of 398 W/m·K, which is significantly higher than die-cast aluminum and aluminum alloy, which range from 130 W/m·K to 220 W/m·K.

Using copper as the heatsink material can improve the conductive heat transfer, resulting in a lower LED T_j. However, copper's higher cost and weight present notable disadvantages.

Wu et al. (2020) used CFD simulations to analyze PCB heat dissipation with materials of varying thermal conductivity. Their study highlighted the critical role of high-conductivity PCBs in reducing LED chip temperatures. Specifically, materials like aluminum nitride (AlN) ceramic substrates, with a thermal conductivity of 350 W/m·K, and metal matrix composites (MMC) were found to be highly effective in preventing overheating in high-power LED lamps.

Zhao et al. (2015) combined FloEFD software simulations with experimental data and found that the maximum T_j of LED varies linearly with the ambient temperature or the heating power. They also performed experiments to confirm the effectiveness of combining heatsink and integrated heat conductive plates (HCPS). Another study by Qin et al. (2021) discovered that LED has strong humidity sensitivity. High humidity decreases the luminous flux and life span of the LED.

Tripathy and Dash (2024) used numerical simulations to evaluate how heatsink design parameters, such as fin length, height, inclination angle, and number influence the heat transfer performance of branching radial heat sinks. Results indicated that fin height and length significantly affect the thermal resistance and heat transfer rates, with branching angles above 25° and fin heights over 19 mm showing the most efficient cooling performance compared to flat plate-fin designs.

In summary, the numerical literature review highlights four fundamental areas of focus in LED headlamp thermal management for numerical approaches:

- Cooling methods (heatsink, heat pipes, convective cooling, HCPS)
- Heatsink design and geometry (cooling fin design)
- The use of high-conductivity materials for PCBs and heatsinks
- The influence of environmental factors (ambient temperature, humidity)

2.3 Research Gaps and Justification for Current Study

Most prior studies on LED thermal management have primarily focused on single LED units in room environment or simplified test chambers. These studies often neglect the thermal interactions between multiple LEDs positioned within enclosed spaces. Automotive headlamps typically house multiple LEDs operating simultaneously, creating complex thermal dynamics due to interactions between multiple heat sources in a confined assembly.

Most prior experiments were conducted at room temperature, while automotive headlamps operate in elevated ambient temperatures caused by engine heat. These higher temperatures pose severe heat dissipation challenges and can greatly impact LED performance. Understanding the thermal and optical behavior of LEDs under these real-world conditions is essential for developing reliable and effective thermal management strategies.

The test chambers used in prior studies are significantly different from the actual geometry and environment of automotive headlamps. Many experiments relied on simplified, box-shaped chambers or temperature-controlled ovens, which fail to replicate the complex design of headlamp assemblies. LED headlamps feature smaller volumes, more complex geometries, and additional components such as reflectors, wirings, and housings. These complexities introduce unique thermal challenges that simplified chamber experiments cannot account for, underscoring the need for more realistic simulations and experimental setups.

A critical gap in existing research is the lack of LED optical performance measurements. Thermal and optical performance of LEDs are linked, as elevated T_j can significantly reduce the LED's luminous flux and efficiency. Without considering optical measurements, previous studies failed to capture the full impact of thermal management strategies on the LED's functionality, particularly in automotive headlamp applications, where optical performance is critical.

Furthermore, existing research has primarily focused on heatsink designs and natural convection cooling. However, many modern automotive LED headlamps utilize forced convection cooling, such as cooling fans, to enhance heat dissipation. Despite its widespread adoption in the industry, effects of forced convection cooling on LED performance and overall headlamp design have not been extensively investigated, leaving a critical gap in the literature.

Another overlooked factor is the use of single ambient temperature settings in test chambers. Real-world automotive headlamps experience a dual thermal environment. As section 1.1.1 mentioned, the front side of the headlamp is exposed to external environmental conditions, while the rear is near the engine compartment, where temperatures are significantly higher. This environmental temperature gradient introduces additional complexities in heat dissipation that current research has not sufficiently addressed.

To bridge these gaps, the current study focuses on comprehensive thermal and optical analysis using a combination of experimental methods and numerical simulations. The experiments in this study utilize a production vehicle headlamp assembly tested in a dual thermal-controlled chamber that replicates the real-world temperature environment between the front and rear of the headlamp. The study investigates the operation of two LED units, compares various cooling methods (e.g., forced convection cooling and forced derating), and measures both temperature and luminous flux. Computational fluid dynamics (CFD) simulations are also performed to further analyze the temperature distribution and fluid flow within the headlamp. By addressing real-world operating conditions and bridging the gaps in existing research, this study aims to provide a more comprehensive understanding of LED thermal management in automotive headlamps.

CHAPTER 3 EXPERIMENTAL METHODOLOGY

This chapter provides a comprehensive overview of the experiments conducted in this study, covering the experimental apparatus setup, controlled variables, testing cases, data collection, and post-processing methods. Three series of experiments were conducted to address specific research objectives, categorized into system-level and component-level testing.

The first series of experiments focused on system-level testing, utilizing a complete LED headlamp to evaluate the overall thermal and optical performance under various operating conditions. Thermocouples and a camera-based photometry system were employed to measure temperature and luminous flux, offering insights into the headlamp's integrated system performance.

The second series of experiments focused on component-level testing, using a single LED unit to directly measure the LED surface temperature under varying thermal environments. These measurements validated numerical simulation results, ensuring accuracy and alignment with experimental data.

The final series also employed a component-level approach to measure the spectral power distribution (SPD) and luminous flux of a single LED unit. These measurements were used to calculate the optical power and heating power of the LED. The calculated heating power value serves as boundary condition for the simulation models.

Collectively, these experiments provide a comprehensive understanding of the LED thermal and optical performance at both system and component level, creating the foundation and preparation for improving and validating the simulation used in this study.

3.1 LED Headlamp Thermal and Optical Measurement Experiment Setup

3.1.1 Thermal Chamber

To effectively control and maintain steady ambient temperatures for the front and rear sections of a headlamp, a specialized thermal chamber was designed and constructed. The chamber encapsulates the headlamp and includes a divider to separate the front and rear of the headlamp, enabling independent temperature control. Heat is supplied by temperature-programmed heat guns, maintaining steady ambient temperatures in the two chamber sections.

The thermal chamber aims to represent the physical model of the real-world scenarios where the headlamp's front section (T_{front}) is range from 20°C to 50°C while its rear section (T_{rear}) resides from 20°C to 105°C. Figure 3.1 shows the CAD geometry of the chamber, with dimensions and material specifications detailed in Table 3.1.

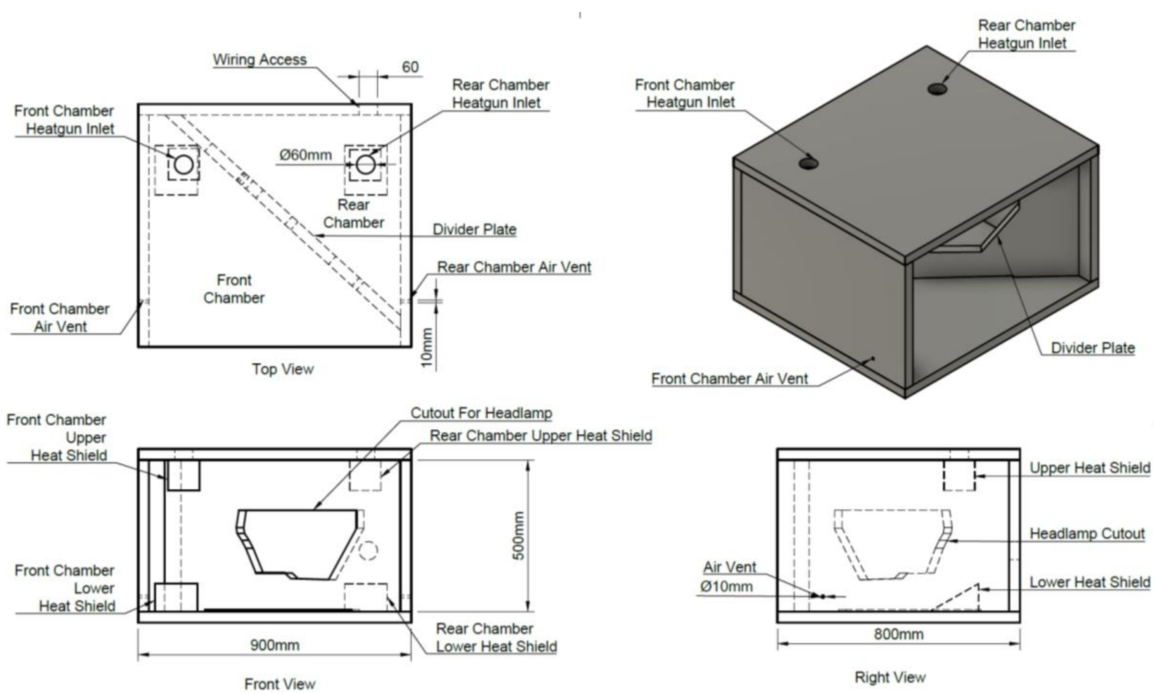

Figure 3.1 Drawing of thermal chamber

Table 3.1 Technical specification of the thermal chamber

Material	Expanded Polystyrene Foam (top, bottom and side walls) plexiglass (front) Aluminum Foil Tape (sealing)
Length	900 mm
Width	800 mm
Height	500 mm
Thickness of the walls	38.1 mm (1.5 inch)

As shown in figure 3.2, the design of thermal chamber provides sufficient space for headlamp, wiring and adequate air circulation, while minimizing the time needed to reach target ambient temperature. The headlamp is positioned at a 44° angle relative to the vehicle's lateral axis, with the divider aligned to this angle to separate the front and rear sections.

Figure 3.2 Thermal chamber on the fixture, equipped with two heat guns and testing headlamp.

The chamber is constructed from expanded polystyrene foam (EPF), chosen for its low thermal conductivity of 0.035 W/m·K and high melting point of 240°C (Triyono et al., 2023). Aluminum foil tape is used to seal gaps between EPF panels, preventing airflow between compartments and the external environment. This tape ensures an airtight seal and withstands the chamber's high temperatures.

Two circular openings with a diameter of 60 mm are created on the top of the thermal chamber to allow hot air from heat guns to enter. The heat guns are connected to a programmable power supply that turns on or off automatically based on the experimental temperature settings (T_{front}/T_{rear}).

To mitigate the risk of inner wall damage caused by the heat gun, which blows hot air at approximately 300°C, aluminum plates are positioned near the outlets and along the inner bottom surface of the chamber to serve as heat shields. These plates are painted matte black to reduce light reflection, ensuring accurate light output measurements.

The chamber's front features a polymethyl methacrylate (PMMA) panel, commonly known as plexiglass, to allow the emitted headlamp light to exit. PMMA transmits 93–94% of visible light, ensuring minimal optical interference (Prasad et al., 2019). Power and signal control wires for the LED lamp pass through a 60 mm rear opening in the chamber wall, which is sealed with aluminum foil tape after installation to maintain insulation.

3.1.2 Wiring

Since the experiment is conducted with the headlamp detached from the vehicle, headlamp wiring is modified to control the cooling fan switch, SLM forced derating feature, and individual LED operation. Instead of using signals and power inputs from the body control module (BCM), the headlamp is controlled via Chrysler Diagnose Tool software, which activates only the low-beam (LB) LEDs. Power is supplied by an external AC/DC converter to provide a constant supply for the LED headlamps.

Each LB LED unit is equipped with a negative temperature coefficient (NTC) thermistor for temperature monitoring. To deactivate SLM forced derating feature, a secondary "dummy" headlamp, which is an exact replica of the experimental model, is used. A simplified wiring diagram is shown in Figure 3.3, explaining the wiring connection from SLM to experiment headlamp and dummy headlamp for individual LED control and forced derating control.

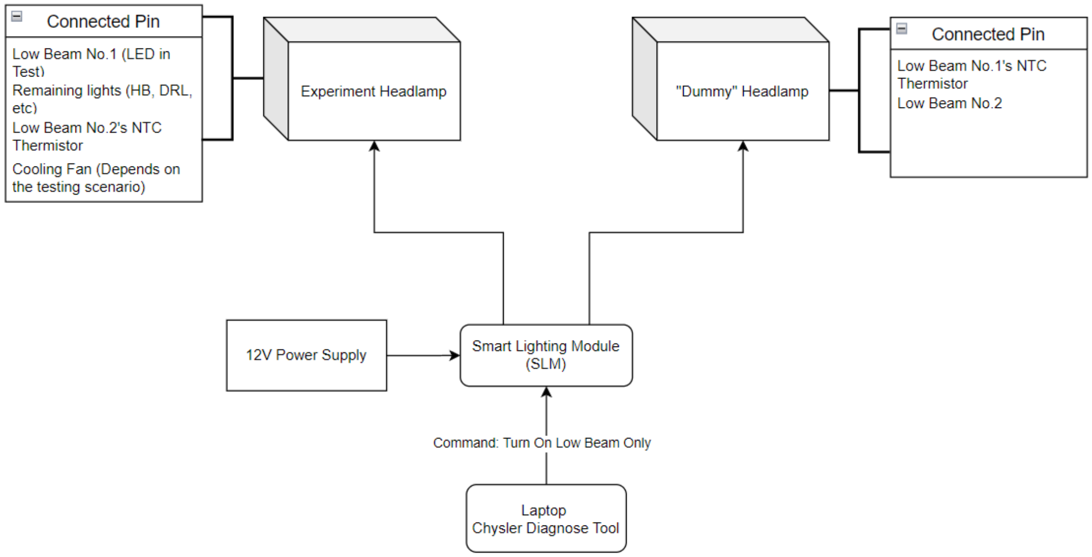

Figure 3.3 Simplified wiring diagram for LED and forced derating control

This dual-headlamp setup isolates and activates a single LB LED in the experimental headlamp by connecting the power cable of the other LB LED to the dummy headlamp. This configuration eliminates light output discrepancies between the two LB LEDs caused by differences in temperature or reflector design.

The dummy headlamp is also used to bypass the forced derating algorithm in the experimental headlamp. By rerouting the NTC thermistor from the active LED in the experimental headlamp to the dummy headlamp and connecting it to the SLM, the system measures the temperature of the inactive LED in the dummy headlamp, which remains at room temperature. This feedback prevents the activation of the forced derating algorithm, as the SLM detects the LED is sufficiently cool.

To implement this setup, the factory headlamp wiring is modified by extending the wires between the LED units and the SLM. Electrical connectors are added to facilitate quick swapping and reconnections for different testing scenarios, as illustrated in Figure 3.4. This figure illustrates the wiring and dummy headlamp setup, which is positioned at the rear of the thermal chamber. During the experiments, the dummy headlamp is covered to prevent its active LED from affecting the luminous flux readings of the testing LED headlamp.

Figure 3.4 Wiring connection and dummy headlamp

3.1.3 Thermocouple Attachments

The K-type thermocouples are installed on the experimental headlamp to measure and record the temperature distributions during each experiment case. These thermocouples have a wide temperature measurement range, from –200°C to +1350°C, and accuracy of ± 0.35% (Manjhi & Kumar, 2019). A total of 14 thermocouples are placed at various locations on the headlamp model. Table 3.2 lists all thermocouples, including their locations and intended functions.

Table 3.2. List of thermocouples

Thermocouple Number	Location	Functionality
T1	Front chamber ambient	Measure the front and rear section air temperature of thermal chamber for heat gun on/off control.
T2	Rear chamber ambient	
T3	Front lens cover (left)	Measure the temperature on the headlamp surface to determine whether it has reach targeted temperature required to start the experiment. (location is shown on Figure 3.5)
T4	Front lens cover (center)	
T5	Front lens cover (right)	
T6	Rear housing (left)	
T7	Rear housing (center)	
T8	Rear housing (right)	
T9	LB1 heatsink (center)	Used for thermal performance analysis and numerical simulation result validation. (location is shown on Figure 3.6)
T10	LB1 heatsink (corner)	
T11	LB2 heatsink (center)	
T12	LB2 heatsink (corner)	
T13	Headlamp internal ambient (near the LB1)	Measure the ambient temperature inside of the headlamp during experiment. Used for numerical calculation and result analysis.
T14	Headlamp internal ambient (near the LB2)	

Figure 3.5 illustrates the thermocouples mounting location T3 – T6 on the headlamp’s front and rear housing. These thermocouples measure the housing temperature to confirm whether the starting criteria for the experiment are met. To access the LB1 and LB2 heatsinks, two cutouts were made on the top surface of the headlamp housing. The locations of these cutouts are also highlighted in the figure.

Figure 3.6 shows the thermocouple mounting locations T9–T12 on the upper surfaces of the LB1 and LB2 heatsinks. T9 and T11, referred to as the LB1/LB2 Heatsink Center, are positioned directly above the LED on the heatsink's upper surface. These locations are chosen because they represent the hottest points on the heatsink due to their proximity to the LED. This placement provides critical data for assessing the maximum operating temperature of the LED, which is essential for evaluating thermal performance and identifying potential overheating risks. T10 and T12, known as the LB1/LB2 Heatsink Corner, are positioned at the corners of the heatsink's upper surface. These secondary measurement points offer additional data for validating numerical simulations.

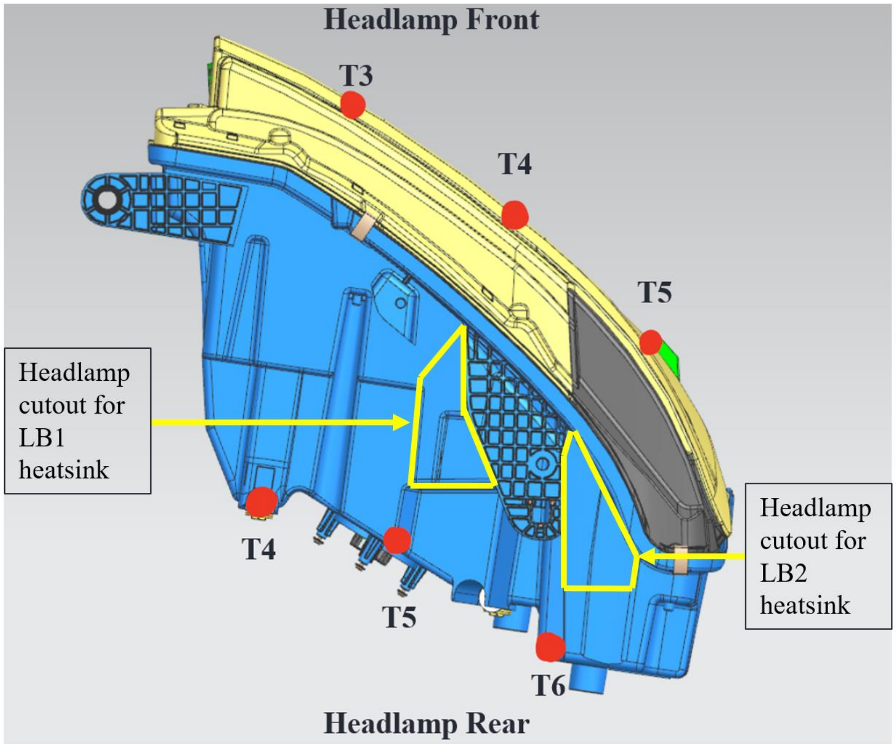

Figure 3.5 Thermocouples T3 - T6 locations (red dots) and cutouts on the top of the headlamp housing

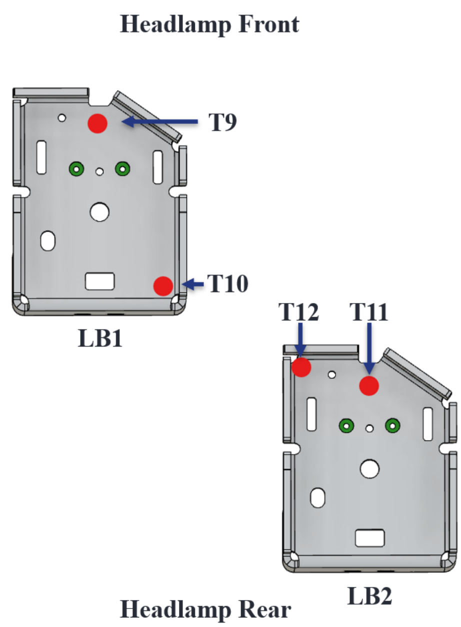

Figure 3.6 Thermocouples T9 - T12 (red dots) locations on the upper surface of the LED Heatsink

The thermocouples were attached to the upper surfaces of the two heatsinks using aluminum foil tape. After installation, the cutout sections of the headlamp housing were reassembled and sealed with aluminum foil tape to restore the housing. Figure 3.7 illustrates the installation of front housing T3 – T5 and the reassembly of the headlamp housing cutouts. Figure 3.8 highlights the mounting of thermocouples T9 and T11 on the upper surface of the LB1 heatsink.

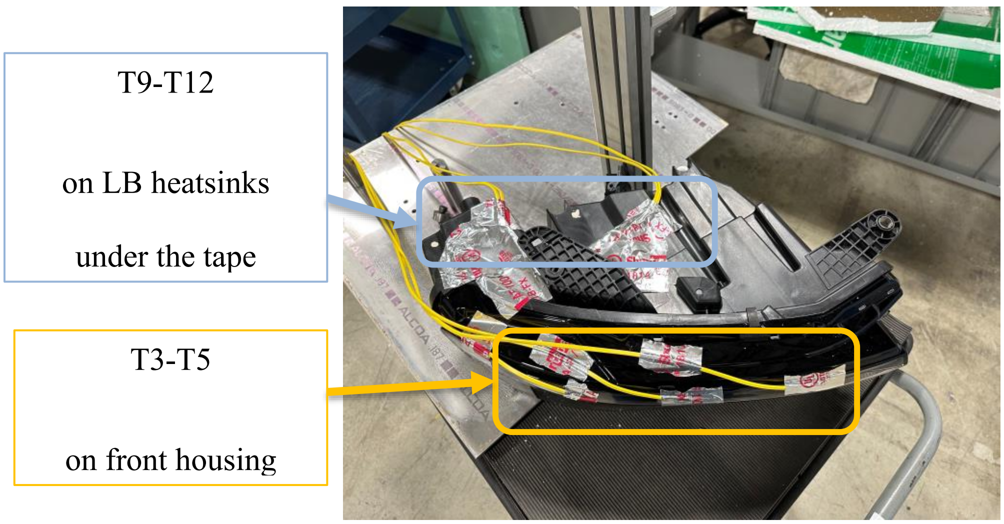

Figure 3.7 Thermocouples T3-T5 and T9-T11 on the headlamp

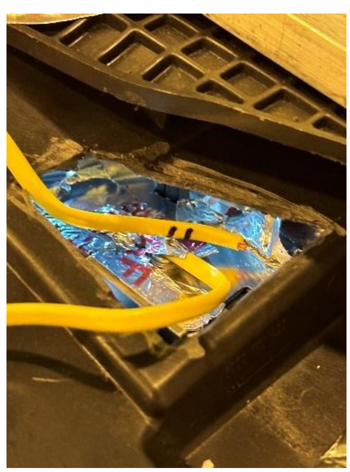

Figure 3.8 Thermocouples T9 and T11 on the LED heatsink

The thermocouples record temperature readings at a frequency of 2 Hz, transmitting the data to a data acquisition unit for recording and conversion into a data file for post-processing. Figure 3.9 provides an example of the results from Test 1, displayed as a scatter plot. The plot shows data points recorded at 30-second intervals, offering a clear visualization of temperature variations over time.

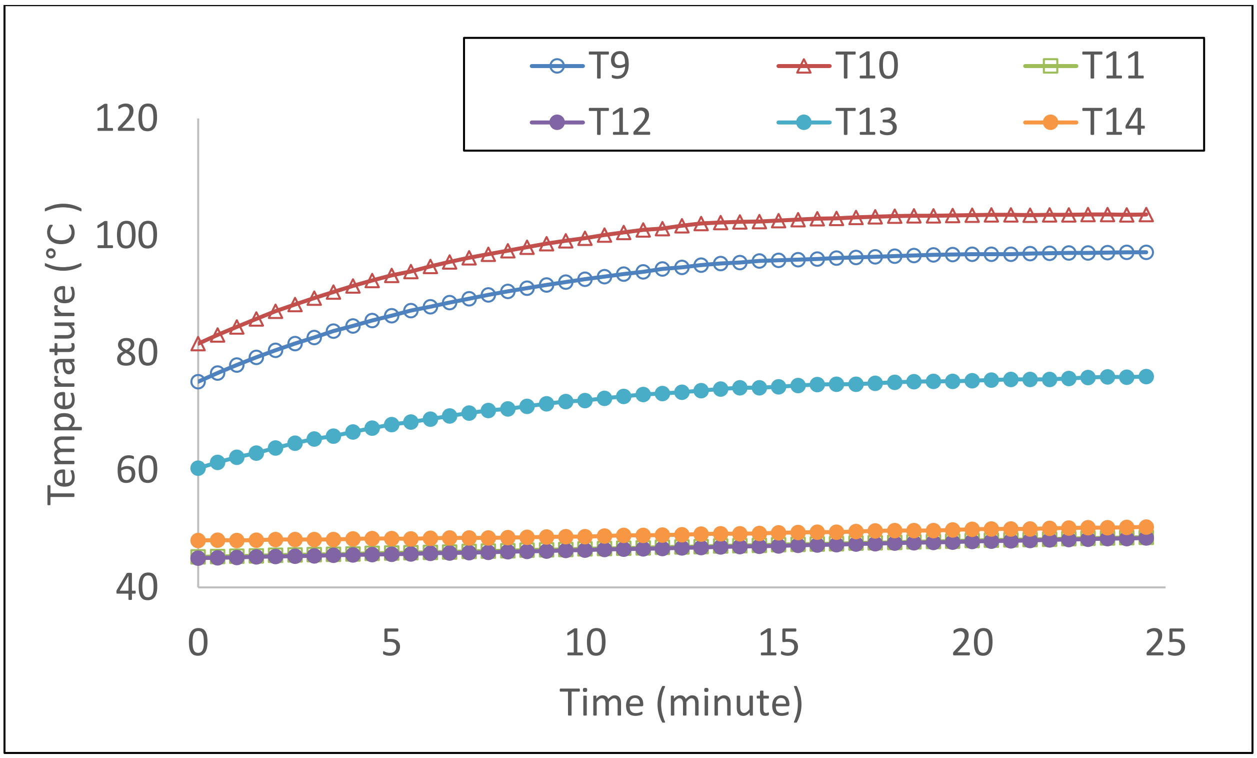

Figure 3.9 Temperature measurement of T9 – T14 over time with sampling frequency of 0.033Hz (Test 1)

Data collection stops when the measured LED heatsink center temperature reaches a quasi-steady-state, defined as a rate of temperature change (dT/dt) of less than 0.1°C/min. Achieving an absolute steady-state, where there is temperature remains constant, is impractical due to the excessive time required. The quasi-steady state criterion balances experimental efficiency and reliable data collection, maintaining a sufficient level of stability for analysis. Detailed experimental procedures are provided in Appendix B.

3.1.4 Light Output Measurement Device

A camera-based photometry system is employed to measure the light output of the headlamp. This system includes three components: a calibrated camera-based photometry device, a measurement screen, and software for real-time data processing. The measurement screen serves as a reference surface for light distribution and intensity measurement. The photometry device captures the light emitted onto the screen by the headlamp and the software processes the data in real-time, providing immediate feedback on the total luminous output of the beam pattern (Sapphire Technical Solutions, 2019).

During the experiment, the total luminous flux is recorded at 30-second intervals. The data is converted into spreadsheet and scatter plots for post processing. Figure 3.10 provides an example of the measured luminous flux over time, displayed as a scatter plot.

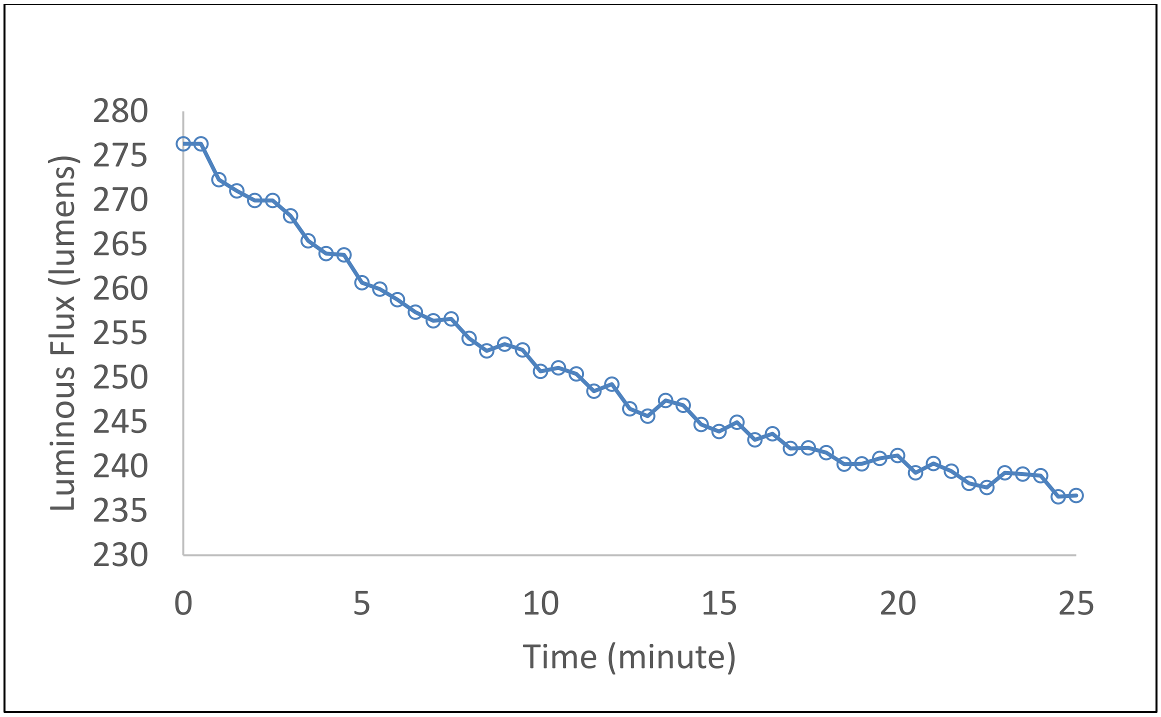

Figure 3.10 Measured luminous flux over time with sampling frequency of 0.03Hz (Test 1)

3.2 Testing Scenarios

Based on the research objectives of the experiment, four key variables were identified to thoroughly investigate the thermal and optical performance of the LED headlamp under varying conditions. Table 3.3 summarizes these experimental variables and its parameters, including testing LEDs, T_{front}/T_{rear} setting, SLM forced derating control and cooling fan. Each variable plays a critical role in evaluating specific aspects of the headlamp's thermal management.

To accurately measure the light output of each LED unit, the experiment is designed to allow independent control of the LB1 and LB2 LED using wiring control. Under different test conditions, LB1 and LB2 may exhibit distinct temperature and light output behaviors. Isolating each LED minimizes measurement errors caused by temperature differences between the two LEDs, ensuring the measured light output reflects only the performance of the testing LED.

Variable temperature conditions (T_{front}/T_{rear}) based on Stellantis headlamp testing standard. These conditions enable performance testing under a range of ambient scenarios, from room temperature (20°C/20°C) to elevated temperature condition (50°C/105°C).

The cooling fan's effectiveness in providing forced convection cooling was evaluated by alternating between ON and OFF states. This comparison between natural and forced convection cooling allowed the study to assess the fan’s impact on the thermal performance of both LB units.

The SLM forced derating algorithm was tested using wiring modifications, as explained in Section 3.1.2. Although the detailed derating logic is proprietary, this approach enabled an evaluation of the SLM’s effectiveness in managing LED thermal and optical performance under various conditions.

Table 3.3 Experiment controlled variables and parameters

Testing LED	Temperature (Front/Rear)	Smart Light Module (SLM)	Fan
LB1	20 ° C / 20° C	ON	ON
LB2	50 ° C / 50° C		
	50 ° C / 85° C	OFF	OFF
LB1 + LB2	50 ° C / 105° C		

The test headlamp contains two identical LB LEDs. However, due to their positions within the headlamp, LB1 and LB2 resulted in different thermal behaviors and light output. Additionally, as the beam patterns of these two LEDs overlap, individual light output measurements required activating each LED separately. Combined testing of both LEDs was conducted to evaluate their interaction and collect data for simulation correlation.

The experiment began with LB1 activated under the lowest ambient temperature conditions (20°C/20°C), with varying the Fan On/Off and SLM Forced Derating On/Off settings. The ambient temperature was then gradually increased to test higher temperature conditions. Once all scenarios for LB1 were completed, wiring adjustments were made to begin testing for LB2. These tests verified that LB2 behaved similarly to LB1 under identical conditions, particularly the Fan Off cases. Finally, both LB LEDs were tested simultaneously to evaluate the interaction between the two LEDs and collect data for simulation correlations.

Tables 3.4, 3.5, and 3.6 outline the experimental cases, specifying the LED unit under test, temperature conditions, fan control settings, SLM forced derating settings and additional explanatory notes. While most tests were conducted once, three consistency tests were performed to evaluate the experiment's repeatability. These consistency tests were repeated three times.

- LB1 Experiment Cases:

Table 3.4 List of LB1 experiments (Test 1 – 13)

Test Number	T_{front}/T_{rear}	Fan ON/OFF	SLM ON/OFF	Notes
1	20°C / 20°C	ON	ON	
2		OFF	ON	
3		OFF	OFF	
4		ON	OFF	
5	50°C / 50°C	ON	ON	
6		OFF	ON	
7		OFF	OFF	Consistency Test
8		ON	OFF	
9	50°C / 85°C	ON	ON	Exceed the safety limit, test stopped.
10		OFF	ON	
11		OFF	OFF	

12		ON	OFF	
13	50°C / 105°C	ON	ON	

- LB2 Experiment Cases:

Table 3.5 List of LB2 experiments (Test 14 – 17)

Test Number	$\mathbf{T_{front}/T_{rear}}$	**Fan ON/OFF**	**SLM ON/OFF**	**Notes**
14	20°C / 20°C	ON	OFF	
15		OFF	OFF	
16	50°C / 50°C	ON	OFF	
17		OFF	OFF	Consistency Test

- Combined Both Low Beams (LB1 + LB2) Experiment Cases:

Table 3.6 List of LB1 and LB2 combined experiments (Test 18 – 21)

Test Number	$\mathbf{T_{front}/T_{rear}}$	**Fan ON/OFF**	**SLM ON/OFF**	**Notes**
18	20°C / 20°C	ON	OFF	
19		OFF	OFF	
20	50°C / 50°C	ON	OFF	
21		OFF	OFF	Consistency Test

3.3 LED Temperature Measurement Experiment Setup

The previous experimental setup focused on system-level thermal and optical performance measurement, evaluating the LED's behavior within the headlamp assembly. However, due to limited access to the LED and the requirement for luminous flux measurements, it was not feasible to install thermocouples on the LED surface for direct temperature measurements.

To address these challenges, a component-level experiment was designed specifically to measure the LED temperature. An identical LB LED unit with it heatsink assembly was tested individually. The objective of this experiment is to measure the LED's quasi-steady-state temperature under various thermal conditions and provide LED temperature for validating numerical simulations.

This experiment utilized the thermal chamber to replicate the internal air environment of the headlamp under different test cases. In previous system-level experiments, air temperatures near the LED unit (T13 and T14) were recorded. For this experiment, the average value of T13 and T14 from test case No. 19 and No. 21 was used as the target temperature to replicate the internal air temperature of the headlamp, as shown in the Table 3.7.

Figure 3.11 illustrates the experimental setup prior to placement in the thermal chamber. The LED unit is mounted on a fixture with silicone rubber insulators placed between the heatsink and the fixture to reduce conductive heat transfer to the fixture. A thermocouple is directly attached to the LED chip to measure its temperature, as shown in Figure 3.12.

The fixture was then placed inside the thermal chamber, and the heat gun was set to achieve the target ambient temperature. Once the chamber reached the target ambient temperature, the LED unit was turned on, and data collection began.

Data collection from the thermocouple continued until the measured LED temperature reached a quasi-steady-state defined as a rate of temperature change (dT/dt) of less than 0.1°C/min.

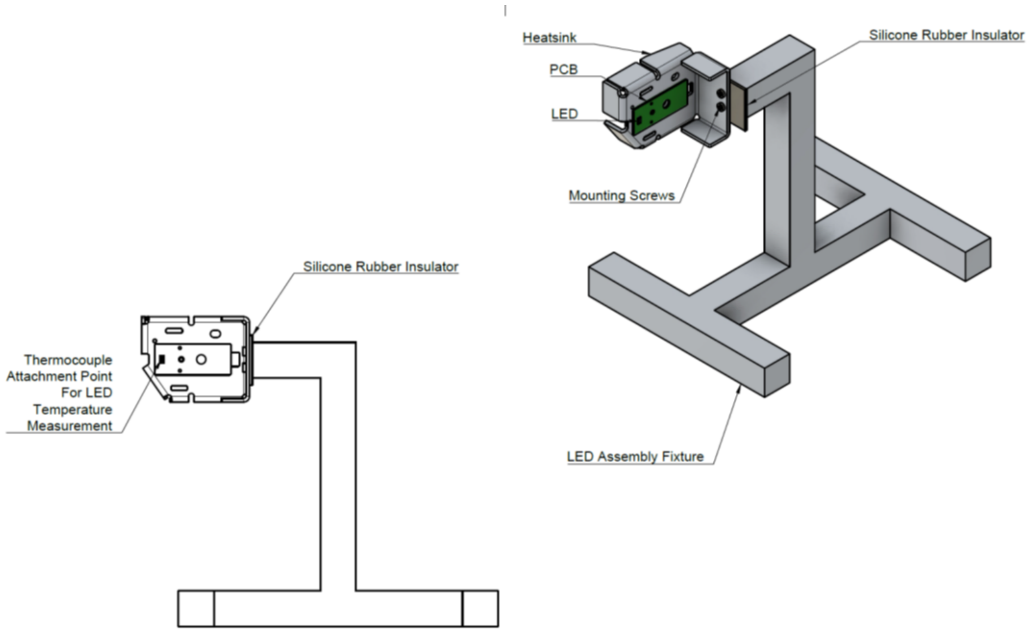

Figure 3.11 Schematic of LED temperature measurement setup

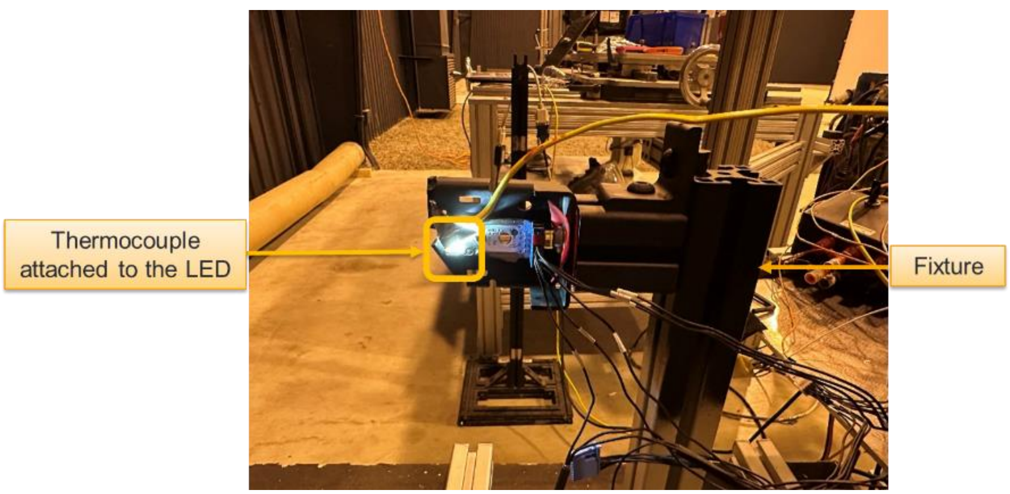

Figure 3.12 LED temperature measurement location

Table 3.7 Thermal chamber temperature setting for LED component-level testing

Experiment Scenarios	**Internal mean air temperature of headlamp at quasi-steady-state**
20°C / 20°C Fan Off	55.2°C
50°C / 50°C Fan Off	78.0°C

However, the component-level experiment was unable to replicate forced convection (Fan On) conditions due to differences in fluid volume and geometry between the thermal chamber and the actual headlamp assembly. To prevent exceeding the LED's maximum temperature rating, high-temperature scenarios were excluded from this experiment. Additionally, the forced derating algorithm from the SLM was disabled to allow a direct assessment of the LED's thermal performance under steady-state conditions.

3.4 LED Optical Power Measurement Experiment Setup and Calculation

This experiment aims to measure the spectral power distribution (SPD) and luminous flux (ϕ) of the LED to calculate its optical power (P_{opt}) and heating power ($P_{heating}$). $P_{heating}$ value is crucial for setting accurate boundary conditions of LED in CFD simulations. The same LED from the previous experiments is used, powered at its nominal operating voltage and current, with a total electrical input power ($P_{electrical}$) of 13.1 W.

A GL Spectis 1.0 Touch spectral light meter was employed to measure the LED's SPD and luminous flux (ϕ). This device, with a measurement tolerance of < 3% (GL Optic, n.d.), ensures high accuracy and repeatability. The experiment was conducted by performing 10 repeated measurements, and the average SPD results and luminous flux were used for calculations. The SPD was measured across wavelengths ranging from 380 nm to 780 nm, capturing the entire visible light spectrum. This range aligns with human vision sensitivity while excluding irrelevant ultraviolet (UV) and infrared (IR) wavelengths. The SPD results were normalized into relative SPD values, as shown in Figure 3.13, for further calculations. The total luminous flux (ϕ) of the LED was measured to be 1397 lm.

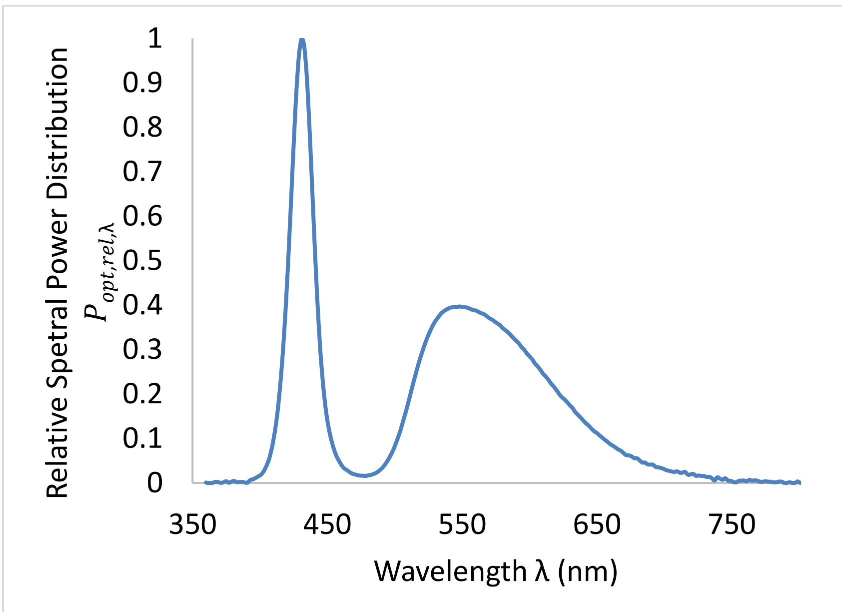

Figure 3.13 Relative Spectral Power Distribution (SPD) of LED at wavelength from 360 nm to 780 nm

Spectral Optical Power ($P_{opt,\lambda}$) at each wavelength (λ) was calculated using the equation:

$$P_{opt,\lambda} = \frac{\phi}{K_{max}} * \frac{P_{opt,rel,\lambda}}{\sum P_{opt,rel,\lambda} * V_{\lambda}} \tag{3.1}$$

In Eq. 3.1, $P_{opt,\lambda}$ is spectral optical power at wavelength λ (W/nm), ϕ is luminous flux (lm) measured by the spectral light meter, K_{max} is maximum spectral luminous efficacy of radiation for photopic vision (Kozai et al., 2016), as 683 lm/W (Ohno, 1997), $P_{opt,rel,\lambda}$ is relative spectral power distribution shown in the Figure 3.14 and V(λ) is spectral luminous efficiency function, representing the average human eye's sensitivity to light, as defined by the CIE Standard Photometric Observer (Rongier et al., 2022).

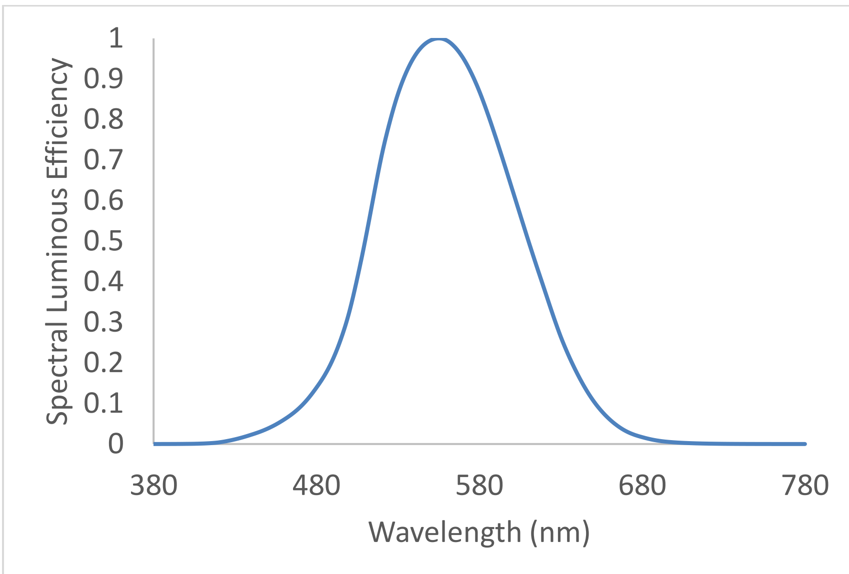

Figure 3.14 Spectral luminous efficiency V(λ) for human eyes, peaked at 555 nm

After calculating $P_{opt,\lambda}$ for all wavelengths from 380 nm to 780 nm, the total optical power (P_{opt}) of the LED was determined by summing $P_{opt,\lambda}$ across the spectrum.

$$P_{opt} = \sum P_{opt,\lambda} \tag{3.2}$$

The heating power ($P_{heating}$), was then calculated as the difference between the $P_{electrical}$ and P_{opt}:

$$P_{heating} = P_{electrical} - P_{opt} \tag{3.3}$$

Table 3.8 Experimental data, equation parameters, and calculated results for optical and heating power

Parameter	**Value**
Electrical input power ($P_{electrical}$)	13.1 W
Measured luminous flux (ϕ)	1398 lm
Maximum spectral luminous efficacy (K_{max})	683 lm/W
Optical power (P_{opt})	4.4 W
Heating power ($P_{heating}$)	8.7 W

The experiment determined the LED's heating power to be 8.7 W, which serves as a volumetric heating source in the CFD simulations for the headlamp's thermal analysis.

CHAPTER 4 NUMERICAL METHODOLOGY

This chapter outlines the numerical methodology employed to analyze the thermal and fluid dynamics of the headlamp system through Computational Fluid Dynamics (CFD) simulations using STAR CCM+ software. The methodology includes headlamp geometry creation, mesh generation, a grid independence study, simulation assumptions, boundary condition setup, and the list of simulation cases.

4.1 Headlamp Geometry

Computational geometry involves simplifying the headlamp assembly while preserving essential features to enable accurate and efficient simulation. To simplify the model and reduce mesh complexity, small features such as screws, clips, internal support structures, and LED wiring were removed. The LED and soldering were combined and represented as a rectangular prism to avoid issues caused by the thin dimensions of the soldering layer and LED chips, which would otherwise complicate the meshing process. The PCB and heatsink, being the primary focus of this study, were retained in their original form, with all details preserved to ensure accurate thermal analysis. However, the mounting holes on the PCB and heatsink were filled in the geometry to reflect the real-world scenario where screws occupy these spaces during assembly. This adjustment not only ensures a more realistic simulation of thermal behavior but also simplifies the mesh generation process. The headlamp fluid domain was created using Space Claim CAD software to replicate the general shape and dimensions of the original headlamp assembly. This approach ensured that the fluid domain accurately reflected the physical characteristics of the headlamp, enabling realistic airflow and thermal simulations.

Once the CAD geometry was created, the files were imported into STAR-CCM+. Components such as the reflector and bezel were removed from the fluid domain using boolean subtraction operations. This approach retained the geometric influence of these components on the flow field while simplifying the simulation by treating their surfaces as boundary conditions rather than modeling them as solid parts. This method effectively reduced mesh complexity and computational demand, ensuring an accurate representation of the flow field while enhancing computational efficiency.

Figures 4.1 and 4.2 present the front and rear isometric views of the simplified headlamp CAD model, displayed in both opaque and transparent views.

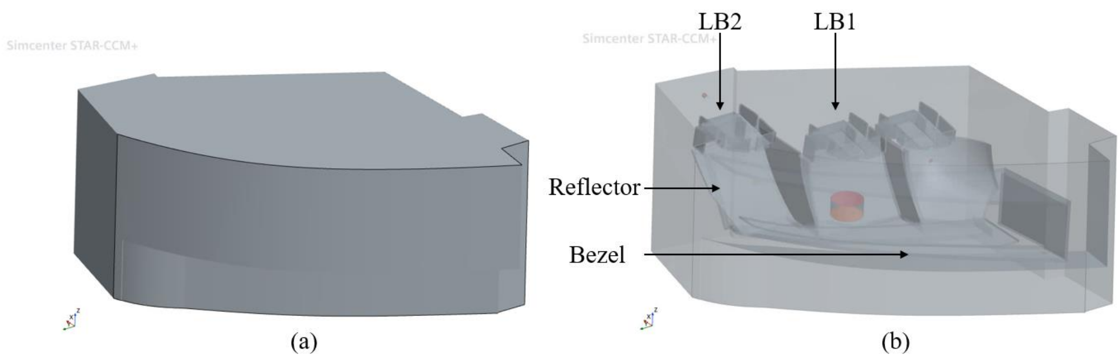

Figure 4.1 Front isometric view of the headlamp fluid domain (a) opaque view (b) transparent view

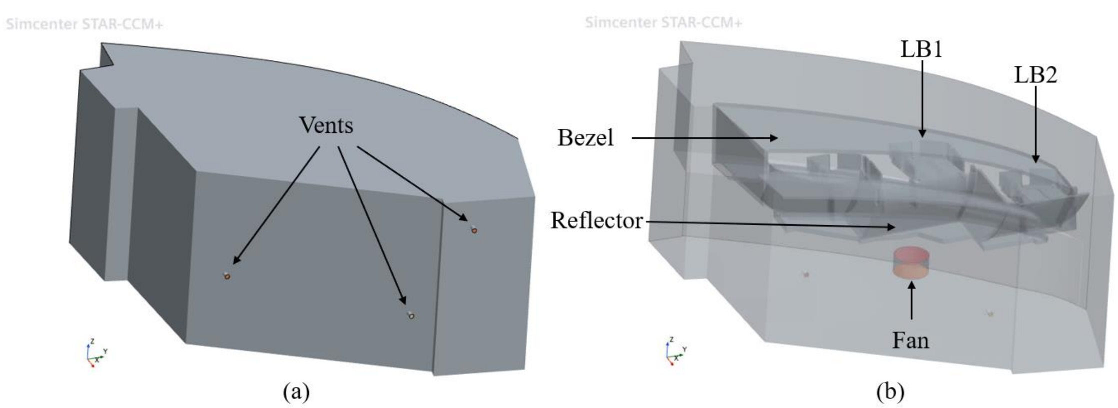

Figure 4.2 Rear isometric view of the headlamp fluid domain (a) opaque view (b) transparent view

4.2 Mesh Generation and Grid Independency Test

Both fluid and solid domains were discretized using a polyhedral, unstructured mesh. Polyhedral elements were selected for their ability to adapt to complex geometries while providing a balance between mesh quality and computational efficiency. The fluid domain contains narrow gaps around the reflector and bezel. These regions required mesh refinement to accurately capture temperature and flow behaviors. To address this, volumetric control was applied to the lower section of the fluid domain, reducing the mesh size by 50% relative to the base fluid domain mesh.

For the solid domain, consisting of the LED, PCB, and heatsink, a mesh resolution of 0.4 mm was applied. This resolution ensures at least 4 - 6 cells across the thickness of the heatsink, effectively captures steep temperature gradients, particularly in areas near heat sources, and ensures accurate results for the thermal analysis.

Figure 4.3 illustrates both the opaque and transparent views of the volume mesh generated for the fluid domain, showcasing the overall mesh distribution and refinement. Additionally, Figure 4.4 presents a right-side cross-sectional view of headlamp simulation near LB1 heatsink and cooling fan, emphasizing the mesh cells around critical components such as the heatsink, bezel, and reflector, emphasizing the refinement in key regions.

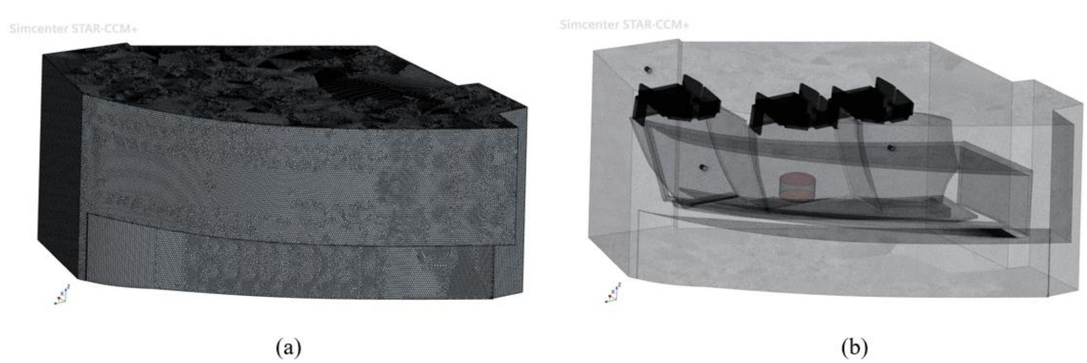

Figure 4.3 Isometric view of fluid domain mesh (a) opaque view (b) transparent view

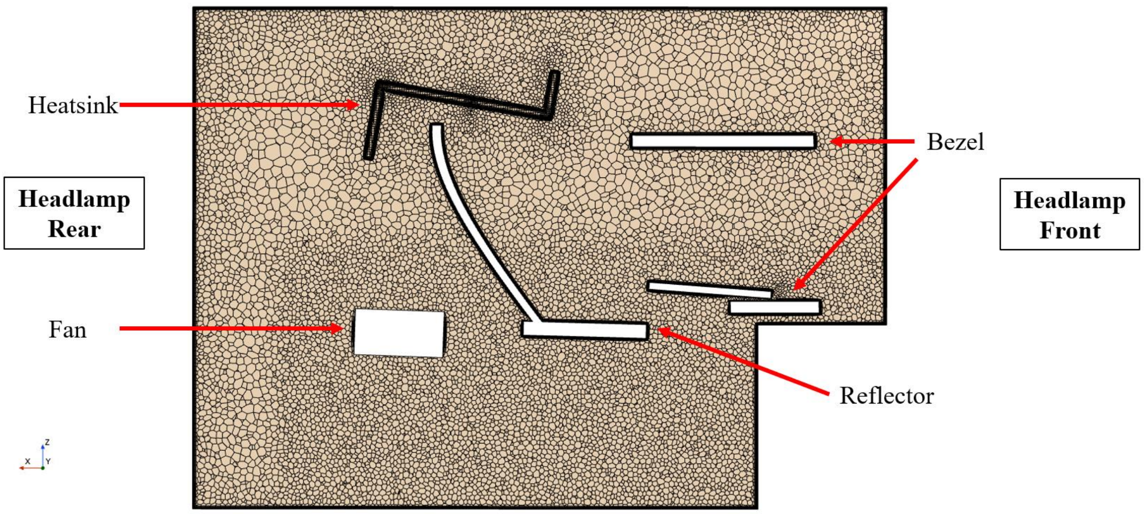

Figure 4.4 Right side cross-sectional view of volume mesh

Table 4.1 Comparison of simulation results across mesh resolutions and extrapolated solution [20°C/20°C Fan On]

Fluid Domain Mesh Size	Number of cells (million)	LB1 T_{center} (°C)	Relative Error (%)	LB1 T_{corner} (°C)	Relative Error (%)
32 mm	0.42	48.1	4.5	38.7	5.1
16 mm	0.69	47.6	3.4	38.1	3.5
8 mm	1.55	47.1	2.3	37.7	2.4
4 mm	4.41	46.3	0.6	37.0	0.5
Extrapolated Solution	∞	46.0		36.8	

A grid independence test was conducted to evaluate the effect of mesh resolution on simulation results, and to ensure the results were sufficiently refined to approach the extrapolated solution. Using 20°C/20°C Fan On case as the testing condition, four different mesh configurations for the fluid domain were generated, where the mesh was progressively refined by a factor of 2. Mesh size of fluid domain chose for this test are 32 mm, 16 mm, 8 mm, and 4 mm. While the rest of the simulation setup remains identical, the CFD simulation results for four mesh configurations are generated.

Estimating temperatures at an infinitely fine mesh is essential for quantifying discretization errors and ensuring that the simulation results are not significantly influenced by mesh resolution. To achieve this, the simulation results for T_{center} and T_{corner} were plotted against the reciprocal of the mesh cell number ($\frac{1}{Mesh\ Cell\ Number}$) for each mesh cell size. A second-order polynomial regression model was fitted to the four data points.

Extrapolation was performed to predict the temperatures when the reciprocal of the mesh cell number approaches zero ($\frac{1}{\infty} \approx 0$), representing an infinitely fine mesh. The calculated temperature values obtained from the regression model at $\frac{1}{Mesh\ Cell\ Number} = 0$ are recorded in Table 4.1 for both LB1 T_{center} and T_{corner}.

The relative error for each data point shown in Table 4.1 across different mesh resolutions was calculated by comparing the simulation results to the extrapolated solution. The finest mesh with mesh size of 4 mm yielded the lowest relative error, within 0.6% of the extrapolated prediction, indicating that it has sufficient numerical accuracy. While the results are not entirely independent of mesh resolution, the grid independence test confirms that the 4 mm mesh size provides results that are sufficiently accurate and reliable for the objectives of this study.

For the fluid domain, the mesh near the wall boundaries is assessed by computing the dimensionless viscous length scale, Y^+. The Y^+ value is used to assess the mesh quality, particularly in simulations involving boundary layers. The Y^+ value represents the dimensionless distance from the wall to the first layer of cells, expressed in terms of the local viscous length scale, which is critical for accurately resolving near-wall flow behavior. The SST k-ω turbulence model requires $Y^+ < 1$ to signify a sufficient resolution of the near wall mesh capable of resolving both flow and thermal gradients at the boundaries with precision. The present $Y^+ = 0.07$ which ensures that the mesh is well-suited for high-fidelity thermal and flow simulations.

4.3 Simulation Assumption

For the current numerical study, the following assumptions are considered:

1. The flow is steady.

2. Air is treated as an incompressible ideal gas for density calculations.

3. Radiation heat transfer is neglected because its contribution to the overall heat transfer is negligible compared to conduction and convection.

4. The thermal properties of all solid components, including the LED, PCB, and heatsink, are assumed to be constant. The LED is modeled as gallium nitride (GaN), the PCB as FR4 epoxy with a copper layer, and the heatsink as aluminum. Thermal properties for these materials at room temperature are provided in Table 4.2.

Table 4.2 Material properties of LED, PCB and heatsink for CFD simulations

Solid Domain	LED	PCB	Heatsink
Material	Gallium nitride (GaN)	FR4 Epoxy + Copper	Aluminum
Density (kg/m^3)	6100	1900	2702
Specific Heat (J/kg K)	370	1150	903
Thermal Conductivity (W/m-K)	253	9	260

5. Boundary conditions of fluid domain, air velocity of cooling fan are considered constant value. The fluid domain boundary is modeled with a constant heat flux condition to simulate heat transfer from the surrounding environment into the system. The fan top surface is set as velocity inlet, fan bottom surface is set as pressure outlet. Air velocity setting is shown in Table 4.3.

Table 4.3 Fan top surface boundary condition setting for CFD simulations

Fluid Domain	Air Velocity (m/s)
Cooling Fan at Fan On case	3.56
Cooling Fan at Fan Off case	0 (wall as boundary condition)

6. Based on the LED experiments and calculation explained in Chapter 3.4. The heating power of the LED is defined as constant value of 8.7 W, representing the amount of electrical power converted into heat during LED operation.

4.4 Simulation Setup

In this study, the CFD simulation was conducted using STAR-CCM+ software, which employs the Finite Volume Method (FVM) to solve the governing equations of fluid flow and heat transfer, including the continuity, momentum, and energy equations.

Constant density models were applied for solid domains, with material properties listed in Table 4.2. For the fluid domain, the ideal gas model was implemented to account for density variations with temperature, which is crucial for accurately capturing natural convection and buoyancy-driven flows. To simulate buoyancy effects, gravity was included in the model. The selection of the turbulence model for the CFD simulation was based on the calculated Reynolds number (Re), which characterizes the flow regime. The Re is defined as:

$$Re = \frac{\rho\, v\, L}{\mu} \tag{4.1}$$

In Eq. 4.1, ρ is the air density, v is the air velocity, L is the characteristic length, and μ is the dynamic viscosity of air. These parameters were determined using the measured internal air temperature obtained from experiment, the inlet velocity of the fan, and the length of the heatsink, as summarized in Table 4.3. Using data based on 20°C/20°C Fan On case, the calculated Re of LB1 heatsink exceeds the critical value of 4000, confirming that the flow is turbulent.

Table 4.4 Reynolds number calculation for LB1 heatsink [20°C / 20°C, Fan On]

Experiment case: 20°C / 20°C, Fan On	**Parameter values**
Air temperature	28.8 °C
ρ: Density of air @ 28.8 °C	1.153 kg/m³

v: Velocity of fan outlet	3.56 m/s
L: Characteristic length of heatsink	0.0724 m
μ: Dynamic viscosity of air @ 28.8 °C	1.81×10^{-5} kg/ms
Calculated Re	16428.5
Flow type	Turbulent flow

The Reynolds-Averaged Navier-Stokes (RANS) approach was utilized with k-ω SST turbulence model employed to resolve the near-wall turbulence. The k-ω SST turbulence model is capable of capturing full range of flow behavior, including laminar and transition flows and it is used for both force convection (Fan On) and natural convection model (Fan Off).

The simulation was conducted under steady-state conditions, employing a segregated flow solver for velocity and pressure fields and a segregated energy solver for temperature distribution.

The front and rear surfaces of the fluid boundary were assigned constant values according to the specific simulation cases. The initial internal ambient temperature of the fluid domain was set to match the experimentally measured ambient temperature.

For simulations involving forced convection (Fan On cases), the fan's top surface was defined as a velocity inlet with an air velocity of 3.56 m/s, while the fan's bottom surface was modeled as a pressure outlet. The temperature of the velocity inlet was aligned with the pressure outlet temperature through a fan interface configuration. In contrast, for natural convection simulations (Fan Off cases), the fan's top and bottom surfaces were set as walls, effectively eliminating active airflow generated by the fan operating conditions.

The temperature monitoring locations shown in Figure 4.5 correspond to the designated points on the upper surfaces of the LB1 and LB2 heatsinks (center and corner), as well as both LEDs, highlighted in Figure 4.5 (b). These locations are identical to the experimental temperature measurement points, ensuring a direct correlation between the simulation and experimental data. This alignment allows for direct comparison of the results, providing a reliable foundation for validating the simulation and assessing the consistency of the CFD model.

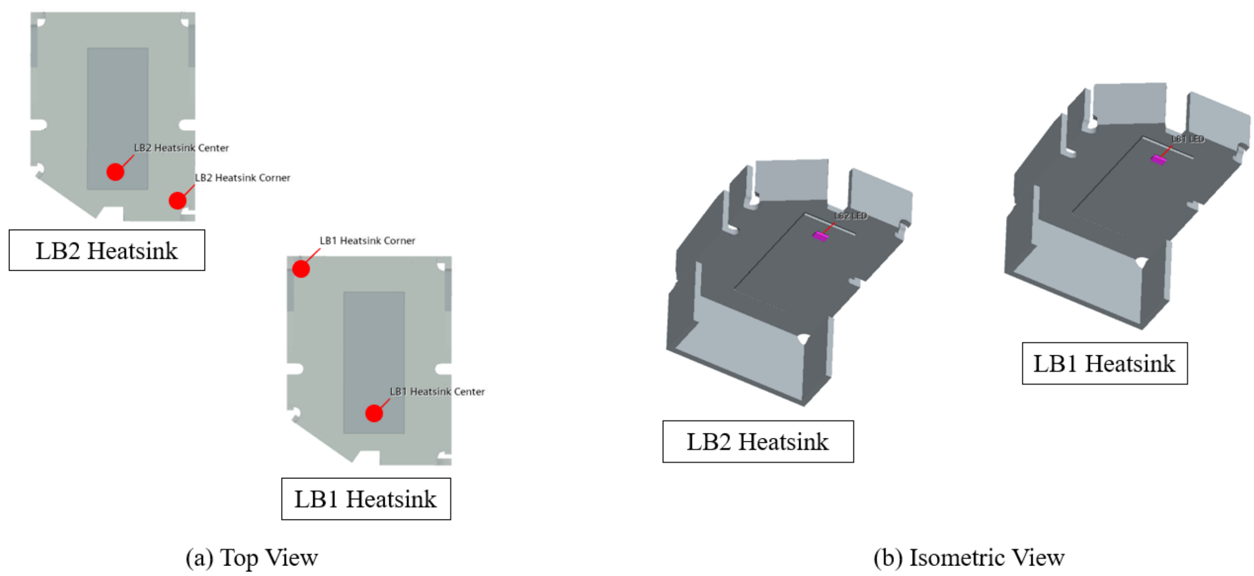

Figure 4.5 Temperature monitor location on LB1 and LB2 in CFD simulation (a) Top view (b) Isometric view

Table 4.5 Axial position of each cross-sectional planes with explanation

Plane View Number	Axial Position	Explanation
V1	Y = 0.664	Right side view of LB1 and cooling fan
V2	Y = 0.777	Right side view of LB2
V3	X = -0.487	Front view of LB1 and cooling fan

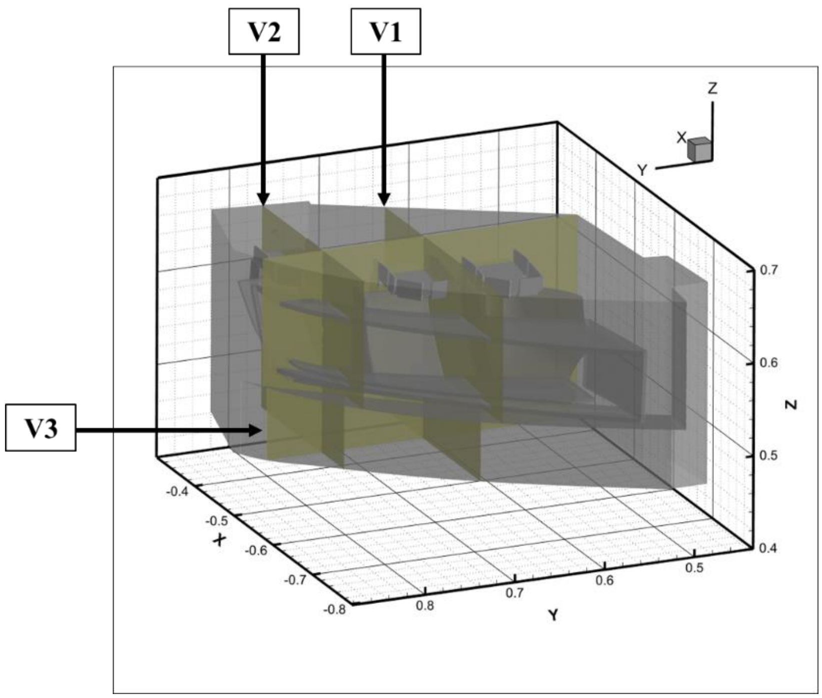

Figure 4.6 Transparent isometric view of the headlamp fluid domain showing labeled cross-sectional planes for post analysis

Three cross-sectional planes, labeled as V1, V2, and V3 in Figure 4.6, were selected for fluid flow field analysis to investigate airflow within the headlamp fluid domain. The axial positions and descriptions of these planes are summarized in Table 4.6. Planes V1 and V2 provide right-side cross-sectional views, with V1 focusing on LB1 and the cooling fan, and V2 focusing on the LB2, capturing the flow field along the longitudinal direction of the LED heatsinks. Plane V3 offers a front cross-sectional view of the heatsinks and cooling fan, enabling the evaluation of airflow distribution surrounding the LB heatsinks. These plane views were chosen to analyze critical regions near LB1 and LB2 units, offering insights into temperature patterns, flow uniformity, and cooling effectiveness within the system.

To investigate and compare the temperature distribution across the LB1 and LB2 heatsinks, temperature data points were extracted from the upper surface s of both heatsinks. The data were recorded along the longitudinal and transverse axes above the LED, as illustrated in Figure 4.7. The extracted temperature data were then converted into scatter plots, providing a clear visualization of temperature variations across the heatsinks for detailed analysis.

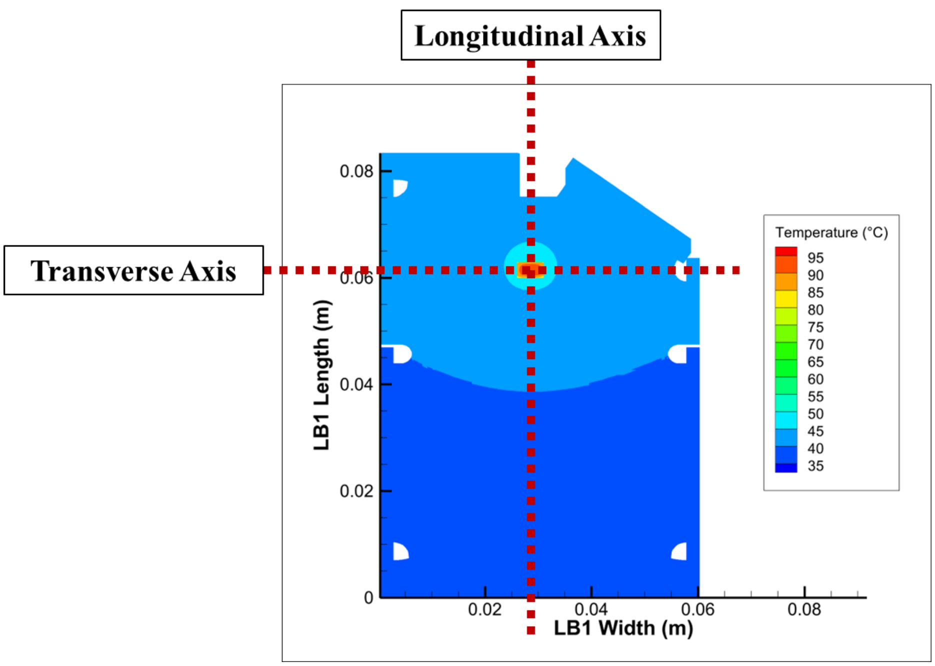

Figure 4.7 Temperature data extraction points along the longitudinal axis and transverse axis on the heatsink upper surface

4.5 Simulation Cases

The simulation cases were designed to replicate the boundary conditions of experimental cases (Test No.18 - 21) to ensure validation and facilitate direct comparisons between numerical and experimental results. In all cases, both LB LEDs (LB1 and LB2) were activated , each assigned a constant heating power of 8.7 W. The study investigated the thermal and flow behavior under varying ambient temperatures and fan conditions, reflecting realistic operating environments for the headlamp system. The specific cases are shown in Table 4.6.

Table 4.6 Simulation cases with variable boundary temperatures and cooling fan settings

Simulation Case Number	Fluid Boundary Temperature (T_{Front}/T_{Rear})	Cooling Fan Setting
1	20°C/20°C	Fan On
2	20°C/20°C	Fan Off
3	50°C/50°C	Fan On
4	50°C/50°C	Fan Off

CHAPTER 5 EXPERIMENTAL RESULTS

This chapter presents a comprehensive analysis of the experimental results evaluating the thermal and optical performance of LED headlamps. The experiments were conducted with controlled variables to ensure accurate and reliable findings. Each experiment case focused on specific factors influencing the thermal and optical behavior of LED units under different operational conditions. A comparative analysis method was used to evaluate the effects of each controlled variable across the experimental cases, enabling a clear assessment of the differences and their impact on the results.

The chapter begins by compiling quasi-steady-state temperatures from each experimental case, which are analyzed and used to validate the numerical simulations. Next, the experimental results are organized into sections based on the controlled variables. The center temperature of the LB1 and LB2 heatsinks was selected for comparative analysis due to its short thermal transfer path, making it highly representative of the LED junction's thermal behavior. Positioned directly above the LED, it is only 3.7 mm away from the LED chip, ensuring accurate and reliable correlation with the heat generated at the junction.

Section 5.2 analyzes the effect of environmental temperature on the thermal performance of the LED units, focusing on how ambient conditions affect LED temperature. This is followed by Section 5.3 investigates the effects of fan cooling and the LED position within the headlamp, highlighting the role of convective cooling strategies and physical placement in thermal management.

Next, Section 5.4 explores the thermal differences between single and dual LED units during operation, assessing the effect of additional LEDs increases the thermal load. Furthermore, Section

5.5 compares LED light output under natural and forced derating, explaining how rising LED temperatures reduce light output and the difference between natural derating of LED and forced derating algorithm from the SLM.

Lastly, an uncertainty and error analysis are conducted, identifying systematic and random uncertainties, and providing a detailed understanding of the experimental limitations.

5.1 Heatsink Quasi-Steady-State Temperature Measurements

The temperature measurements of the LED headlamp, obtained using the testing methodology described in Section 3.1, are summarized in Tables 5.1, 5.2, and 5.3, categorized by the testing LEDs. These tables present the steady-state temperatures recorded at three critical locations (refer to Section 3.1.3): the heatsink center, the heatsink corner, and the internal air temperature within the headlamp assembly. The test cases presented in the tables include only those where the SLM forced derating is disabled, to accurately evaluate the temperature behavior of the LED unit with constant power input. These measurements are used as validation data for the numerical simulation.

During the experimental process, it was observed that under high-temperature conditions, such as the 50°C / 85°C Fan Off case, steady-state temperature for the LED heatsink could not be achieved due to exceeding the temperature limitations of both the LED and the thermal chamber. The excessive heat generated by the heat gun caused deformation of the thermal chamber walls, and the testing LED began flickering, indicating signs of LED overheating. To prevent permanent damage to the LED and the thermal chamber, the high-temperature experiments were discontinued. Consequently, high-temperature test cases No. 11, No. 12, and No. 13 (refer to Table 3.4) could not be completed.

Table 5.1 Measured quasi-steady-state temperature of LB1 heatsink under different test scenarios [SLM Off]

LB1 ON ONLY			
Test case (SLM Off)	Heatsink Center	Heatsink Corner	Internal Ambient
20°C / 20°C, Fan On	42.5 °C	36.0 °C	28.8 °C
20°C / 20°C, Fan Off	87.3 °C	80.1 °C	50.7 °C
50°C / 50°C, Fan On	69.3 °C	62.6 °C	55.9 °C
50°C / 50°C, Fan Off	105.0°C *	97.7 °C *	77.0 °C *
50°C / 85°C, Fan On	90.6 °C	83.7 °C	77.5 °C
50°C / 85°C, Fan Off *	119.4 °C *	112.5 °C *	92.7 °C *

**For the 50°C / 50°C and 50°C / 85°C Fan-Off scenario, the experiment was terminated before the heatsink temperature reached a steady-state due to the temperature exceeding the predefined safety limit of 105°C at heatsink center.*

Table 5.2 Measured quasi-steady-state temperature of LB2 heatsink under different test scenarios [SLM Off]

LB2 ON ONLY			
Test case (SLM Off)	Heatsink Center	Heatsink Corner	Internal Ambient
20°C / 20°C, Fan On	58.1°C	52.5°C	26.2°C
20°C / 20°C, Fan Off	82.3°C	76.0°C	42.3°C
50°C / 50°C, Fan On	85.6°C	80.2°C	55.0°C
50°C / 50°C, Fan Off	110.5°C	104.2°C	70.4°C

Table 5.3 Measured quasi-steady-state temperature of combined LB1 and LB2 heatsink under different test scenarios [SLM Off]

COMBINED LOW BEAMS					
Test case (SLM Off)	Heatsink Center		Heatsink Corner		Average Internal Ambient
	LB1	LB2	LB1	LB2	
20°C / 20°C, Fan On	43.6°C	64.5°C	39.8°C	59.0°C	36.2°C
20°C / 20°C, Fan Off	89.3°C	89.8°C	86.1°C	83.9°C	55.2°C
50°C / 50°C, Fan On	69.1°C	88.8°C	65.4°C	83.5°C	58.0°C
50°C / 50°C, Fan Off	114.7°C	115.2°C	111.3°C	109.3°C	78.0°C

Table 5.4 presents the experimental results of the LED surface temperature measurements, as described in Section 3.3. The measured steady-state LED surface temperatures can be combined with the results for the 20°C/20°C, Fan Off and 50°C/50°C, Fan Off cases from Table 5.3 to validate the simulation results.

Table 5.4 Measured quasi-steady-state temperature of single LED surface temperature under different ambient condition

SINGLE LED	
Test case (SLM Off)	LED Surface Temperature
20°C / 20°C, Fan Off	105.0 °C
50°C / 50°C, Fan Off	130.6 °C

5.2 Impact of Environmental Temperature on the LED Thermal Behavior

This section compares the experimental results for the LED headlamp under varying environmental temperatures. These experiments specifically monitor the temperature at the center of the LB1 LED heatsink, with data collected at one-minute intervals to capture the dynamic thermal response. Throughout these tests, the headlamp's cooling fan was disabled to isolate the effects of forced convection cooling on the LED heatsink's thermal behavior.

Figure 5.1 presents the temperature of the LED heatsink center over time under three different ambient temperature conditions: 20°C/20°C, 50°C/50°C, and 50°C/85°C. The results indicate a correlation between ambient temperature and heatsink temperature. As the ambient temperature increases, the heatsink starts at a higher initial temperature and reaches a higher temperature at the same time step during the heating process. Heat dissipation (Q) is driven by the temperature gradient between the heatsink and the surrounding environment. A higher ambient temperature reduces this gradient, making it less effective for the heatsink to transfer heat to the surrounding air. Consequently, the LED heatsink retains more heat, leading to a higher steady-state temperature.

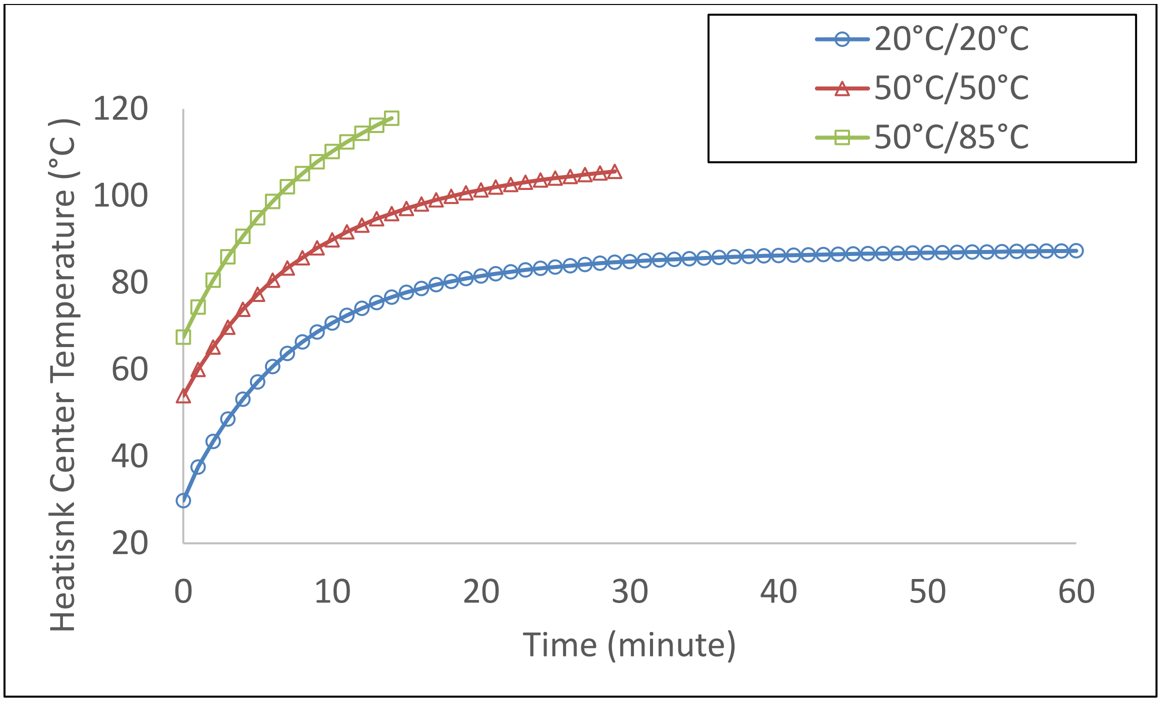

Figure 5.1 LB1 LED heatsink center temperature response under different environmental temperature conditions [20°C/20°C, 50°C/50°C, and 50°C/85°C; fan off]

For the cases with ambient temperatures of 50°C/50°C and 50°C/85°C, the experiments were terminated before reaching steady-state to prevent potential irreversible damage to the LED units caused by excessive heat. Despite the early termination, the temperature rate of change (dT/dt) for these two conditions shows similar trends, as depicted in Figure 5.2.

Figure 5.2 shows the rate of temperature change (dT/dt) at the heatsink center under three ambient conditions. The general trend for all three conditions follows a similar pattern, where the dT/dt initially peaks between 6°C and 8°C per minute at first minute of operation, indicating rapid temperature changes during the initial starting phase. This initial dT/dt variation may because of the initial starting condition of the experiment, where the heatsink temperature did not match the internal ambient temperature of headlamp, creating a temperature gradient which changes Q and consequently affect dT/dt. As the heatsink temperature approaches steady-state, dT/dt gradually decreases, eventually stabilizing close to 0°C per minute after approximately 30 minutes. This dT/dt trend remains similar across different ambient temperature condition.

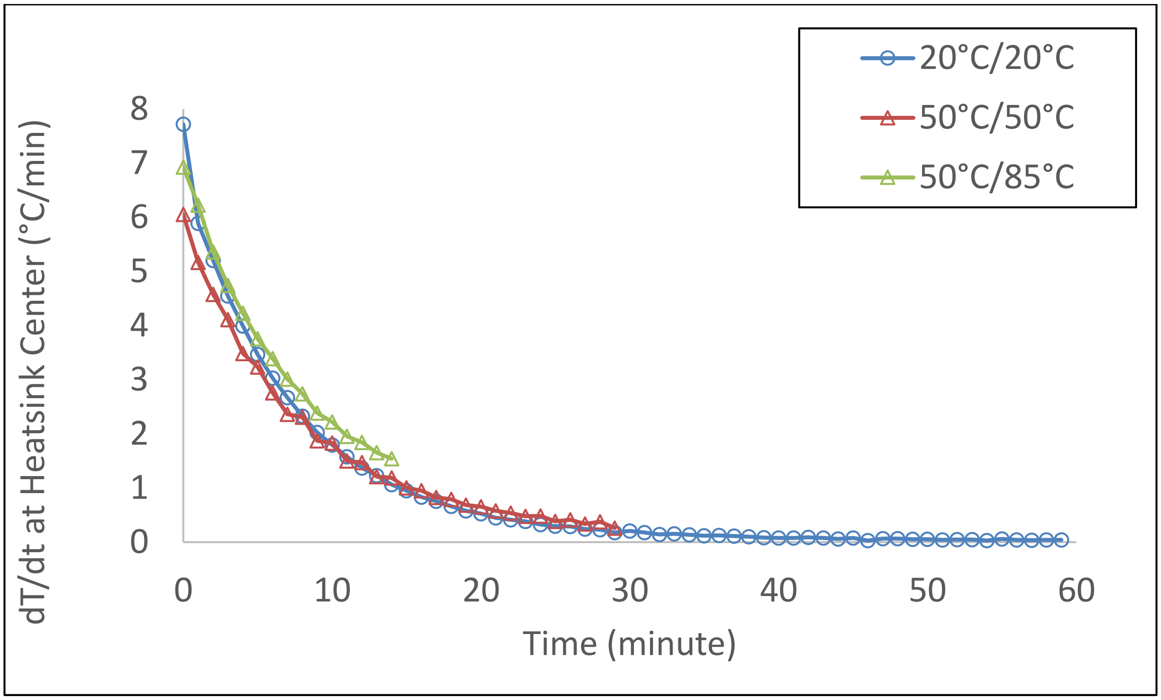

Figure 5.2 Temperature rate of change at the LED Heatsink Center under Different Ambient Conditions [20°C/20°C, 50°C/50°C, and 50°C/85°C; fan off]

These experiments demonstrate higher environmental temperatures lead to increased heatsink temperatures, presenting significant challenges for LED headlamp thermal management. While reducing the ambient temperature is often unfeasible, particularly for the front side of the headlamp, which is directly exposed to external environmental conditions, managing the rear side temperature presents opportunities. The rear side of headlamp is influenced by the heat from the engine compartment, which could potentially be mitigated through improved headlamp positioning or the application of cooling systems and thermal insulation methods. Implementing these strategies could help reduce the thermal load on the system and reduce the LED temperature.

5.3 Effects of Fan Cooling and LED Position in Headlamps

This section presents an analysis of the effects of headlamp fan cooling and LED location on the thermal performance of LED headlamps by comparing experimental data under two different conditions: with the cooling fan activated (Fan On) and deactivated (Fan Off). The primary parameters monitored are the LED heatsinks center temperature, as both LB LED units have identical power outputs and heatsink dimensions. Consequently, the variation in LED heatsink temperature can be primarily attributed to the airflow generated by the cooling fan, given the different positions of the LB1 and LB2 LED units relative to the fan (see Figure 1.4 for headlamp geometry). By examining the heatsink temperatures of LB1 and LB2 under these controlled conditions, this study aims to identify potential thermal hotspot within the headlamp structure and the limitations of the current cooling airflow design.

Figure 5.3 compares the center temperature of the LB1 and LB2 heatsinks under both natural convection (Fan Off) and forced convection (Fan On) conditions over time. When the cooling fan is deactivated, natural convection becomes the primary mechanism for dissipating heat to the ambient air, while heat from the LED to the heatsink is transferred by conduction. The heatsink temperatures of both LB1 and LB2 are identical under the natural convection case. This observation indicates that the position of the LED units within the headlamp has negligible effect on their thermal performance under natural convection conditions.

In contrast, when the cooling fan is activated, forced convection becomes the dominant cooling mechanism, significantly enhancing heat dissipation from the system. Heatsink temperatures for both LB1 and LB2 are significantly lower compared to the natural convection scenario. At steady-state conditions, the LB2 heatsink is 25.5°C cooler, and the LB1 heatsink is 46.3°C cooler than their respective temperatures in the natural convection case. These results underscore the critical role that active airflow plays in enhancing the thermal performance of the headlamp system.

A comparison between the heatsink temperatures of LB1 and LB2 under forced convection reveals that the LB1 heatsink is 20.8°C cooler than the LB2 heatsink. This significant difference can be attributed to the positioning of the LED units relative to the cooling fan. The LB1 unit is positioned directly above the fan, resulting in direct, perpendicular airflow across the LB1 heatsink and the printed circuit board (PCB). In contrast, the LB2 unit is not aligned with the fan's direct airflow path, and its airflow is further obstructed by the design of the reflector and other headlamp components, which blocks the air stream. This finding can be further analyzed and validated through fluid flow field studies using CFD simulations.

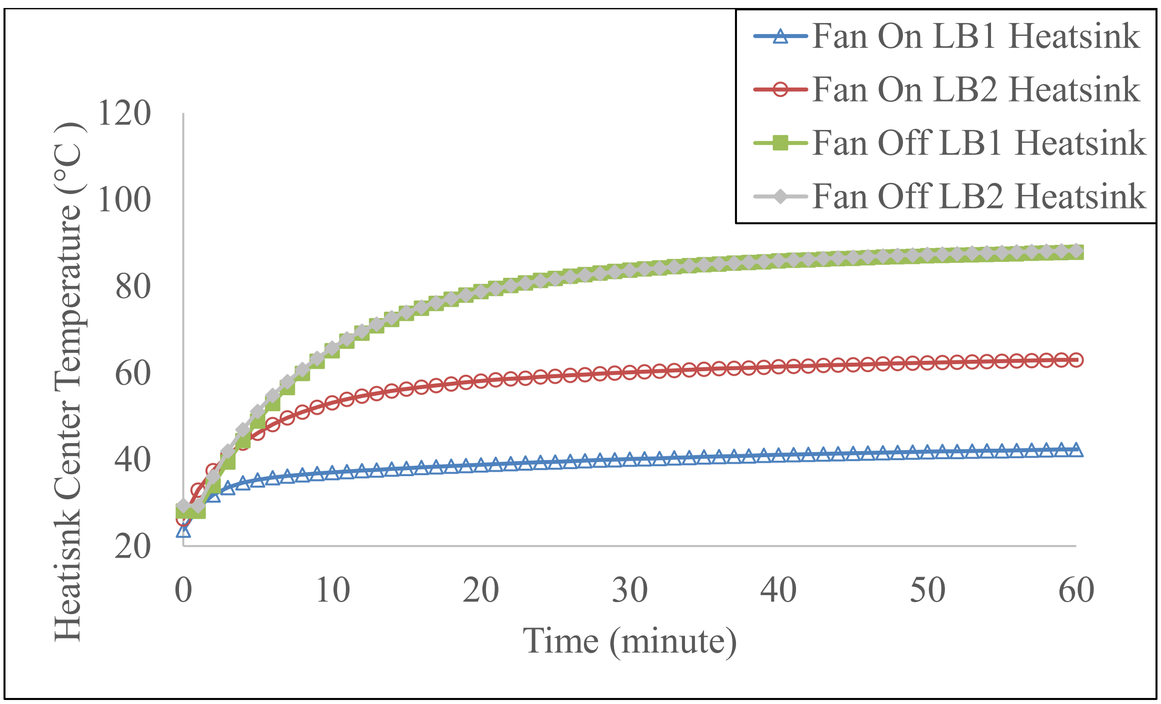

Figure 5.3 LB1 and LB2 LED heatsink temperature over time under natural convection and forced convection [20°C/20°C]

This section of the convective cooling analysis highlights the importance of forced convection in effectively reducing the LED heatsink temperature. Additionally, the relative positioning of the LED unit and the cooling fan plays a critical role in determining the overall convective cooling performance.

5.4 Impact of LB1 and LB2 on the Headlamp Thermal Performance

This section analyzes the temperature behaviors of two LED units, LB1 and LB2, under varying operational conditions: individual operation and combined operation, at an ambient temperature of 20°C, with the cooling fan either activated (Fan On) or deactivated (Fan Off).

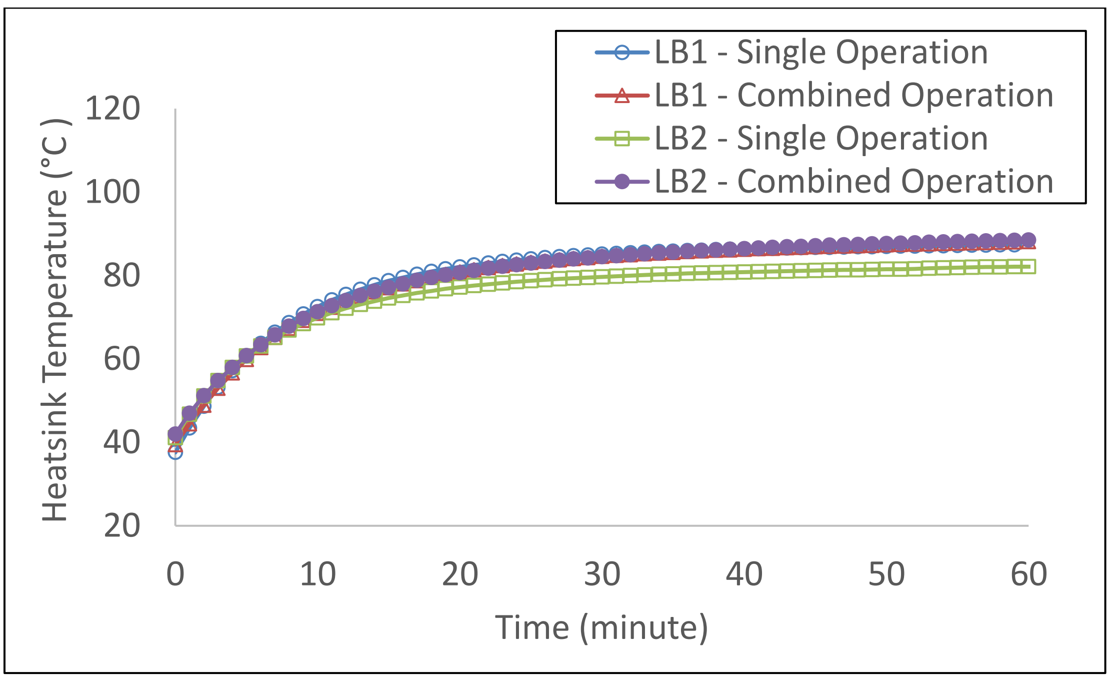

Figure 5.4 LB1 and LB2 LED heatsink center temperature over time under individual LED tests and combined test [20°C/20°C]

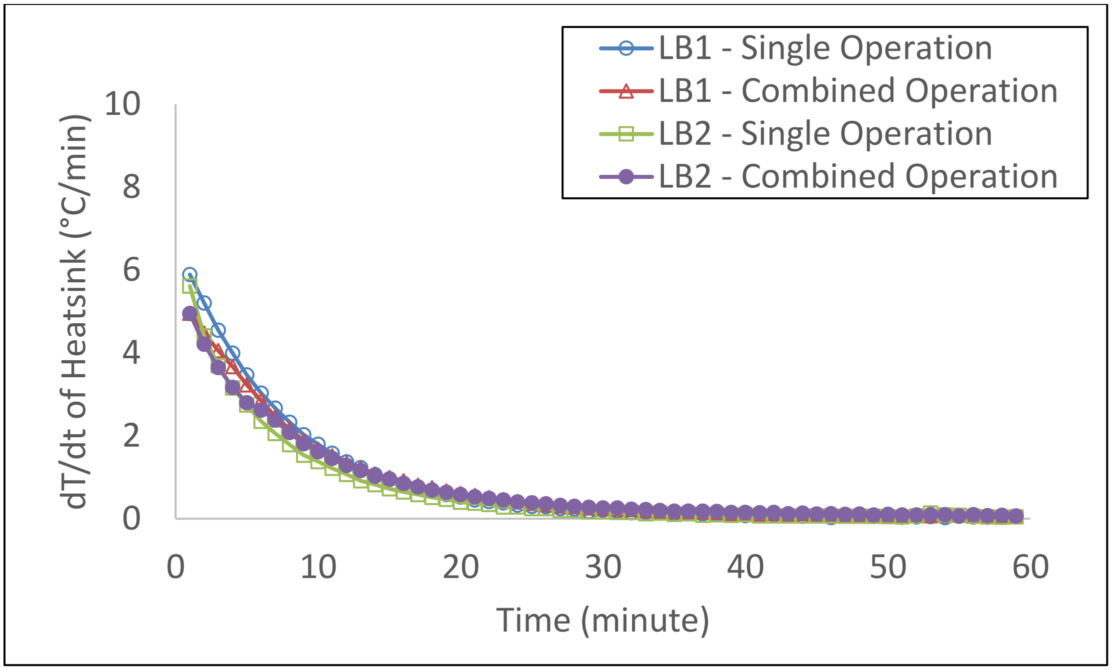

Figure 5.5 Heatsink temperature rate of change of LED LB1 and LB2 under single and combined operation [20°C/20°C]

The experimental results presented in Figure 5.5 compare the heatsink temperature variation of LB1 and LB2 over time under these conditions where the cooling fan is deactivated. The thermal behavior of the LED heatsinks indicates that the absence of a cooling fan does not significantly affect the temperature trends of LB1 and LB2 when evaluated separately or in combination. The data show that the temperature profiles of LB1 are nearly identical whether it operates individually or in conjunction with LB2. This indicates that the thermal performance of LB1 remains stable and is not significantly influenced by the activation of LB2.

LB2 exhibits a slightly different thermal response when influenced by the operation of LB1. Experimental results indicate that LB2 reaches a steady-state temperature approximately 6°C lower during single operation compared to combined operation. However, this difference may be attributed to uncertainties or errors in the experimental readings.

The graph presented in Figure 5.6 shows the heatsink dT/dt for LB1 and LB2 have high similarity between each other and single/combined operations.

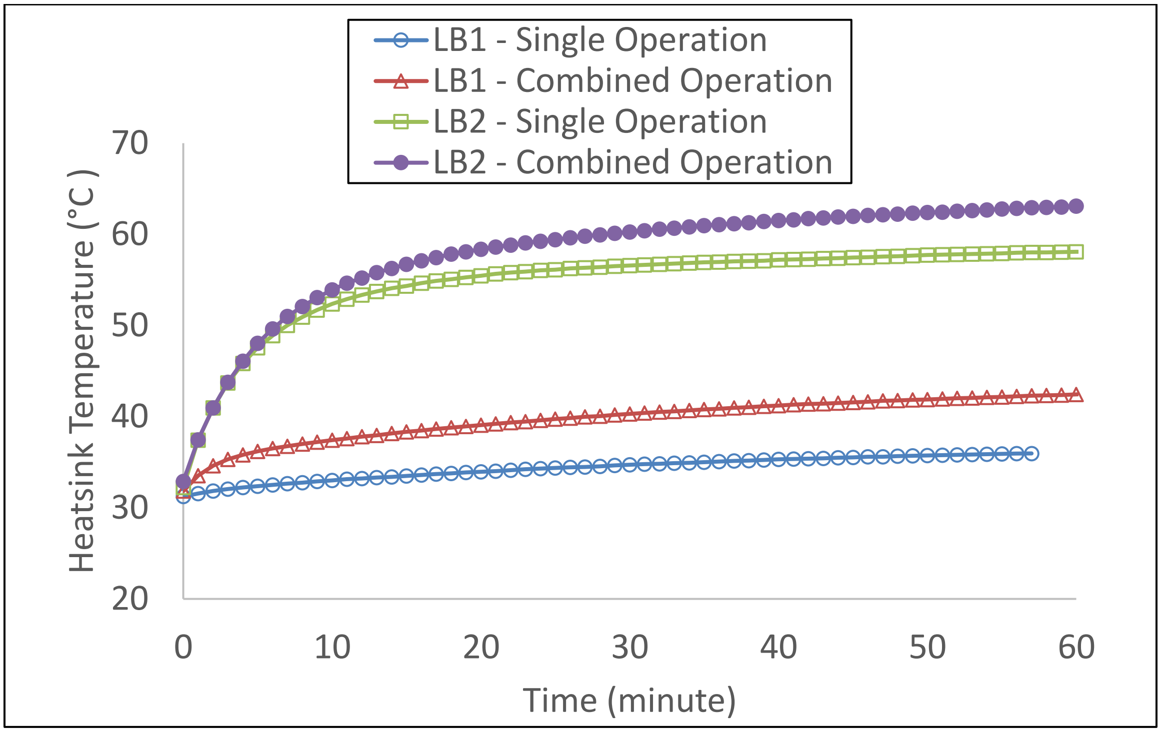

Figure 5.6 LED LB1 and LB2 heatsink center temperature over time under individual LED tests and combined test [20°C/20°C, fan on]

When the cooling fan is activated, the LB1 and LB2 heatsinks temperature deviates significantly, as demonstrated in Figure 5.7. The data indicate that LB2 reached a higher steady-state temperature compared to LB1, under both single and combined LED operations. These results highlight the reduced effectiveness of forced convection cooling for the LB2 unit, identifying it as the thermal weak point in the headlamp system.

In the case of single LED operation, the steady-state temperature of LB2 heatsink is 15.7°C higher than that of LB1 heatsink, highlighting a substantial difference in the convective cooling performance between two LED units. This suggests that under forced convection cooling, the positioning or airflow conditions around LB2 may be less effective, leading to reduced cooling efficiency for LB2 relative to LB1.

When both LEDs are operating simultaneously (combined LED operation), the results show that the heatsink temperatures for both LB1 and LB2 are higher in the combined operation compared to their respective single-operation scenarios. Specifically, in combined operation, LB1 is 1.15°C hotter than when it operates individually, while LB2 exhibits a more pronounced increase of 6.4°C. The internal ambient temperature is also approximately 9°C higher compared to individual LED operation cases. This indicates that when there are two LED as heat source, it increases the internal ambient temperature, result in higher steady-state temperature for both LED units. This effect is more pronounced for LB2, as its position farther from the fan limits its convective cooling performance, result in a higher temperature.

These findings suggest that while the cooling fan enhances overall thermal management, LB2 remains a thermal hotspot. Its higher temperature under both individual and combined operation is due to its position and air flow obstruction in the headlamp. Improving airflow distribution or optimizing the heatsink design could reduce the LB2 temperature and enhance the overall headlamp performance.

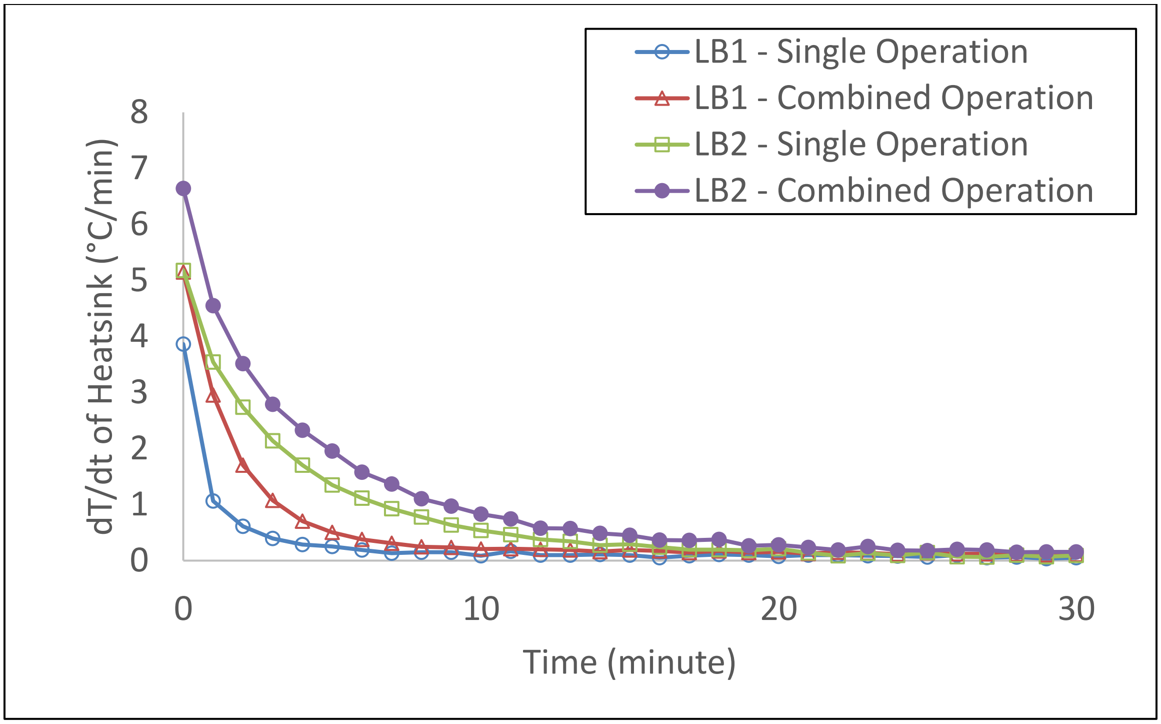

Figure 5.7 Heatsink temperature rate of change of LED LB1 and LB2 under single and combined operation [20°C/20°C, fan on]

The rate of temperature change (dT/dt) for the heatsinks of LED units LB1 and LB2 under both single and combined operation at a 20°C ambient temperature with fan cooling is displayed in Figure 5.8. The figure illustrates the transient thermal response of the LEDs from the initial stages of operation until unit approaches steady-state temperature.

LB2 in combined operation exhibits the highest initial temperature rise rate, peaking at approximately 7°C per minute, and corresponds to the previously observed highest steady-state temperature. This suggests that LB2 experiences significant thermal load from increased internal ambient temperature when both LEDs are active, combined with less effective convective cooling.

In single operation case, both LB1 and LB2 shows a lower dT/dt, stabilizing earlier at a lower temperature compared to combined operation. Single LED operation generates half of the heat compared to combined operation, without thermal coupling, the internal ambient temperature is reduced, leading to lower overall temperatures.

These findings reinforce the need for improved thermal management of LB2, particularly under combined operation, to address the higher thermal load and optimize cooling performance.

5.5 Natural and Forced Derating Luminous Flux Analysis

The luminous flux performance of the LB1 LED under natural and forced derating conditions was analyzed using experimental data collected in high temperature environments (50°C/85°C, Fan Off). This experimental setup allowed for a comprehensive analysis of LED thermal and optical behaviors under high temperature conditions, while avoiding interference from LB2, ensuring the results were solely attributable to single LED unit thermal and optical behavior.

Figure 5.9 illustrates the LB1 heatsink center temperature over time under a 50°C/85°C ambient condition with the cooling fan disabled (fan-off). This experimental setup is designed to maximize the LED temperature, serving as a stress test to evaluate the optical performance under elevated thermal conditions. Initially, the thermal behavior of the LED under both derating modes was highly similar until the LB1 heatsink temperature reached 100°C. At approximate 100°C heatsink temperature, a clear separation in temperature trend is shown. While natural derating case shows a gradual and consistent increase in temperature, forced derating case exhibits a noticeable change in behavior, with dT/dt slowing down and stabilizing at approximately 109.5°C.

This temperature trend highlights the significant effectiveness of the forced derating algorithm in controlling LED temperature. While the exact control logic of the forced derating algorithm built into the SLM is proprietary and not explicitly known, its basic operation can be inferred. The forced derating mechanism relies on temperature feedback from an NTC thermistor integrated into the LED chip. Once the temperature reaches a predefined threshold, the algorithm actively reduces the power supplied to the LED based on this feedback.

Reducing power towards LED directly lowering its heat generation, as well as optical power. The reduction in heating power minimizes the amount of heat introduced into the headlamp system, thereby reducing the thermal load. As a result, the forced derating algorithm prevents excessive temperature rise, stabilizing the system and protecting the LED from thermal damage while maintaining operational reliability.

However, the reduction in optical power results in a corresponding decrease in luminous flux. Figure 5.10 illustrates the luminous flux reduction over time for both cases. The normalized luminous flux reduction value is defined as the ratio of the absolute change in luminous flux at a given time step relative to the luminous flux at the initial time step of the experiment, divided by the initial luminous flux value. This normalization provides a dimensionless measure of the reduction in luminous flux over time, as expressed in the following equation:

$$Normalized\ \phi\ reduction\ (\%) = \frac{|\phi\ at\ each\ time\ step - \ \phi_{initial}|}{\phi_{initial}} \qquad (5.1)$$

This method helps to visualize the percentage of luminous flux reduction over temperature variation for both natural and forced derating.

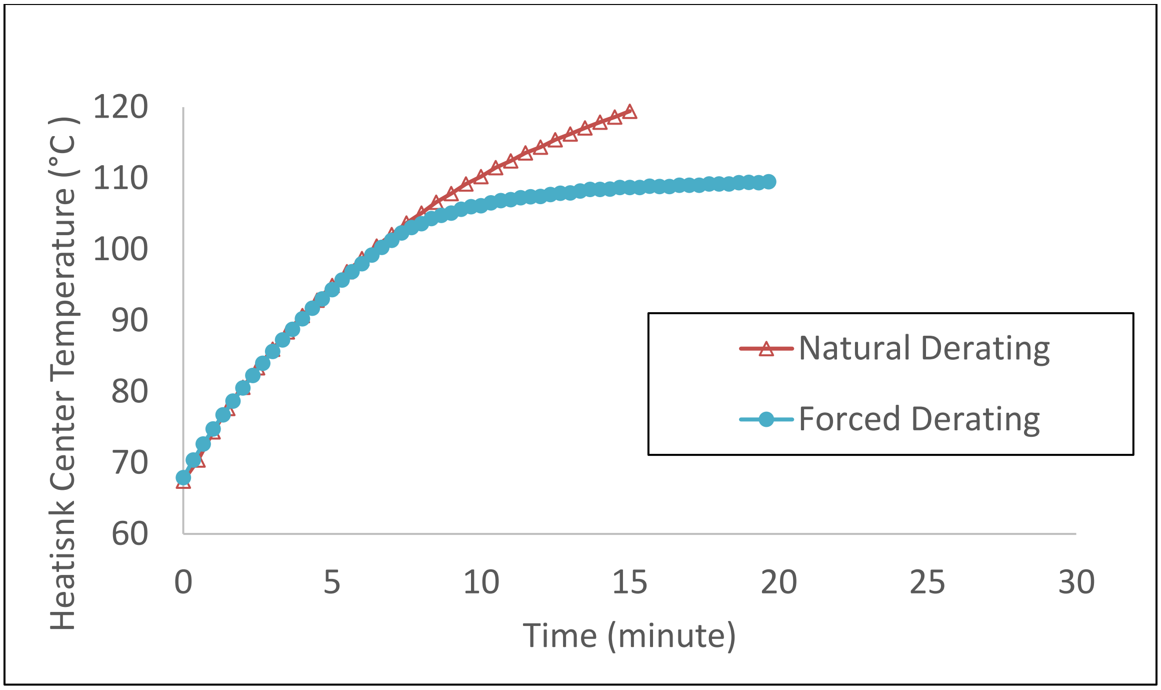

Figure 5.8 LB1 LED heatsink center temperature variation over time under different cooling and derating configurations [50°C/85°C, fan off]

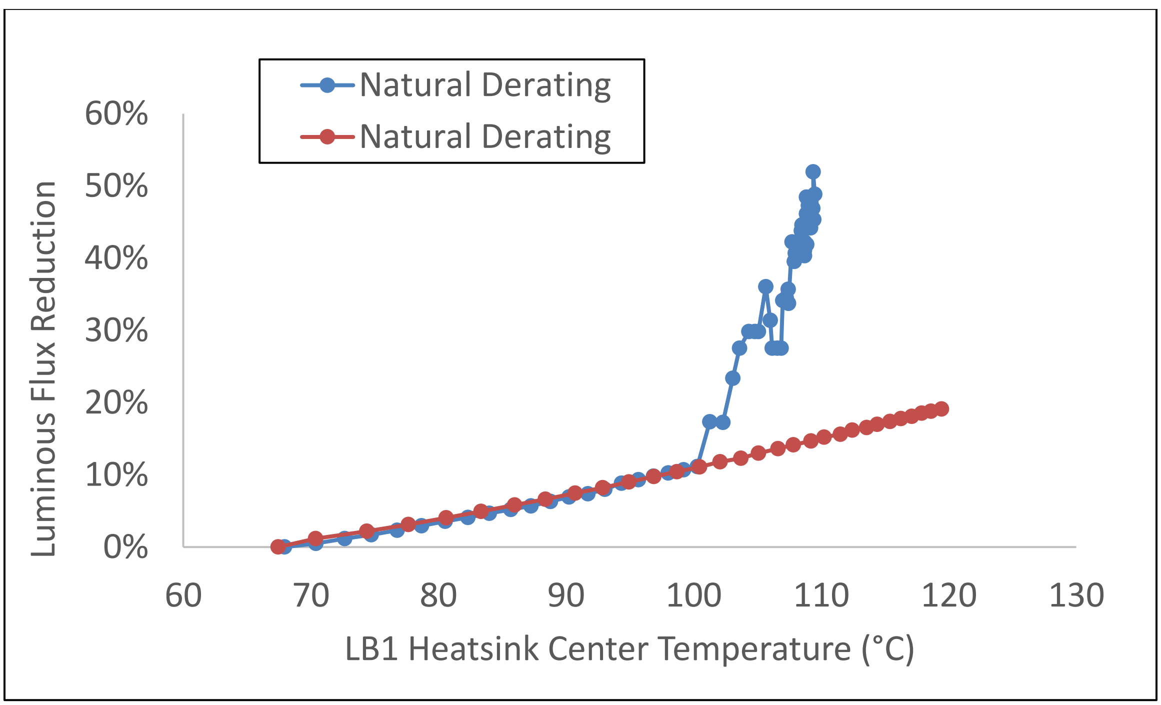

Figure 5.9 Luminous flux reduction percentage of LED under different cooling and derating configurations over time [50°C/85°C, fan off]

The natural derating process is characterized by a gradual and quasi-linear decline in luminous output as the temperature rises. In this experiment, LB1's heatsink temperature increased by 55°C in 15 minutes, eventually reached 120°C. As shown in the Figure 5.9, the temperature was still increasing steadily at 120°C. To prevent potential damage to the LED, the test had to be halted. This indicates that natural derating does not effectively limit temperature rise, especially at elevated temperature operating conditions. Although the luminous flux gradually decreased, the LED system did not take any active steps to manage the rising thermal load beyond the passive reduction in light output based on LED's which includes LED's efficiency degradation, shift in wavelength and increased resistance or thermal stress (Liu et al.,2009, Chang et al.,2012).

In contrast, the forced derating algorithm implemented within the LED system is designed to actively manage the thermal behavior of the LED by reducing power input when the LED reaches a critical temperature. Once the heatsink temperature crossed the 100°C threshold, the SLM reduced the LED's power input, which caused a 5% drop in light output compared to natural derating at the same temperature. The gap in illuminance performance widened as the temperature continued to rise. When the heatsink reached 110°C, the forced derating algorithm had reduced the luminous flux by 52%, whereas under natural derating, the reduction was only 14.7% at the same temperature. The distinct difference in illuminance performance at the same LED heatsink temperature shows how forced derating prioritizes temperature control over luminous performance, particularly at elevated temperatures, sacrificing light output to preserve the LED's thermal integrity.

Another notable effect of forced derating is the high-frequency light flicker observed during the transition period. Once forced derating was triggered, the rate of luminous flux variation was

±6%/minute, which caused a noticeable flicker in the light output, a side effect not observed under natural derating.

Despite this flicker, forced derating demonstrates significant advantages in thermal management. At the 15-minute mark, the heatsink temperature under forced derating was 10.6°C cooler compared to natural derating case. Additionally, the dT/dt reduces significantly, approaching a quasi-steady-state . This suggests that forced derating offers superior thermal control by limiting the rate of temperature rise and effectively stabilizing heatsink temperature. However, it sacrifices significant luminous output which can be safety hazard for real world application.

5.6 Uncertainty Analysis

The reliability and consistency of the experimental results were assessed by repeating tests under identical conditions and comparing the temperature and luminous flux data. Each LED operating configuration (LB1, LB2, and LB1 + LB2) was tested three times to ensure reproducibility. Key measurements included the LED heatsink temperature and luminous flux over time.

This uncertainty analysis quantifies the uncertainties associated with temperature and luminous flux measurements, incorporating both systematic uncertainty (*b*), such as sensor calibration inaccuracies, and random uncertainty (*a*) due to measurement variability of the repetitive experiment results. The random uncertainty is calculated as the standard deviation of the measurement results at each time step. The total uncertainty (*U*) is calculated using the following equation:

$$U = \sqrt{a^2 + b^2} \tag{5.2}$$

Additionally, potential errors from the apparatus and procedures, are discussed to provide a comprehensive understanding of the results.

5.6.1 Temperature Repeatability

Temperature measurement uncertainty includes both systematic uncertainty and random uncertainty. Systematic uncertainty is the accuracy of temperature measurement device, the K-type thermocouples which is ± 0.35% (Manjhi & Kumar, 2019). Random uncertainty is determined by calculating the standard deviation of the heatsink center temperature across repeated experimental measurements at each time step. For all trials, the standard deviation was below 1.53°C. The combined uncertainty was calculated using the root sum square (RSS) method, with the maximum value of ±1.5%. This indicates that the variation in temperature readings between trials is small.

Figure 5.10 illustrates the averaged LB1 heatsink center temperature from three repeated trials over time under the 50°C/50°C Fan Off case (Test No. 21). For better clarity, data points are shown at 2-minute intervals. The error bars at each data point represent the combined uncertainty.

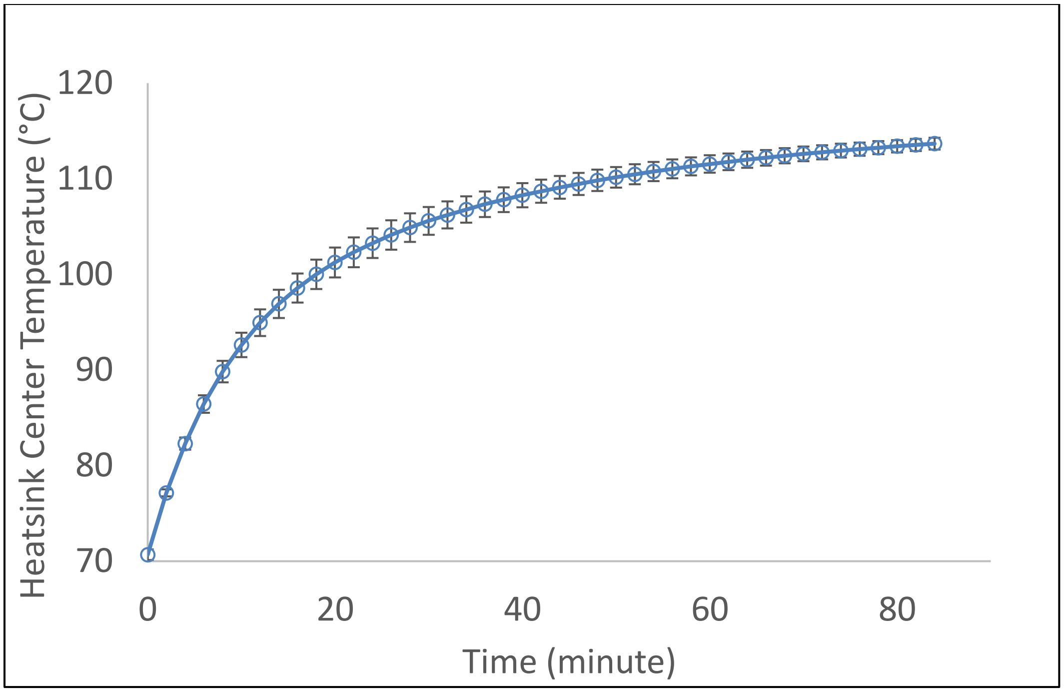

Figure 5.10 Averaged LB1 heatsink center temperature over time, with error bars, data points recorded at 2-minute intervals [50°C/50°C, fan off]

The initial heatsink temperature variation across the three experiments is ±0.79% due to limitations in precisely controlling the starting temperature. Temperature variation increases during the initial phase of the experiment, where the temperature rises more rapidly, leading to an increase in random error. As the heatsink temperature begins to stabilize over time, the random error decreases due to reduced temperature variation across trials, resulting in improved consistency in the measurements.

In summary, the maximum combined uncertainty of ±1.5% demonstrates that the experimental measurements are reliable and consistent, with variations in temperature readings remaining minimal across repeated trials.

5.6.2 Light Output Repeatability

Combined LB LED test data are used to demonstrate the repeatability of the light output measurement. The experiment involved three repeated trials, measuring the total luminous flux of combined LED units LB1 and LB2 as a function of heatsink center temperature under 50°C/50°C fan-off case. Since the luminous flux was recorded at different temperature points across the three trials, three polynomial models were generated to interpolate the luminous flux values between 70°C and 110°C at 2°C intervals. The interpolated luminous flux values at each temperature among the three trials were then used to calculate the standard deviation, representing the random uncertainty of the light output measurement. The systematic uncertainty for the light output measurement remains unknown due to the lack of accuracy data for the camera-based photometric system.

Figure 5.14 illustrates the total luminous flux as a function of average heatsink center temperature of LB1 and LB2, with error bars indicating the uncertainty. The vertical error bars represent the uncertainty in light output measurements, while the horizontal error bars represent the uncertainty in temperature measurements, as explained in Section 5.6.1. The maximum light output uncertainty was calculated to be 0.5%. This minor variation is likely due to calibration of the light measurement device, which was recalibrated at the start of each testing day.

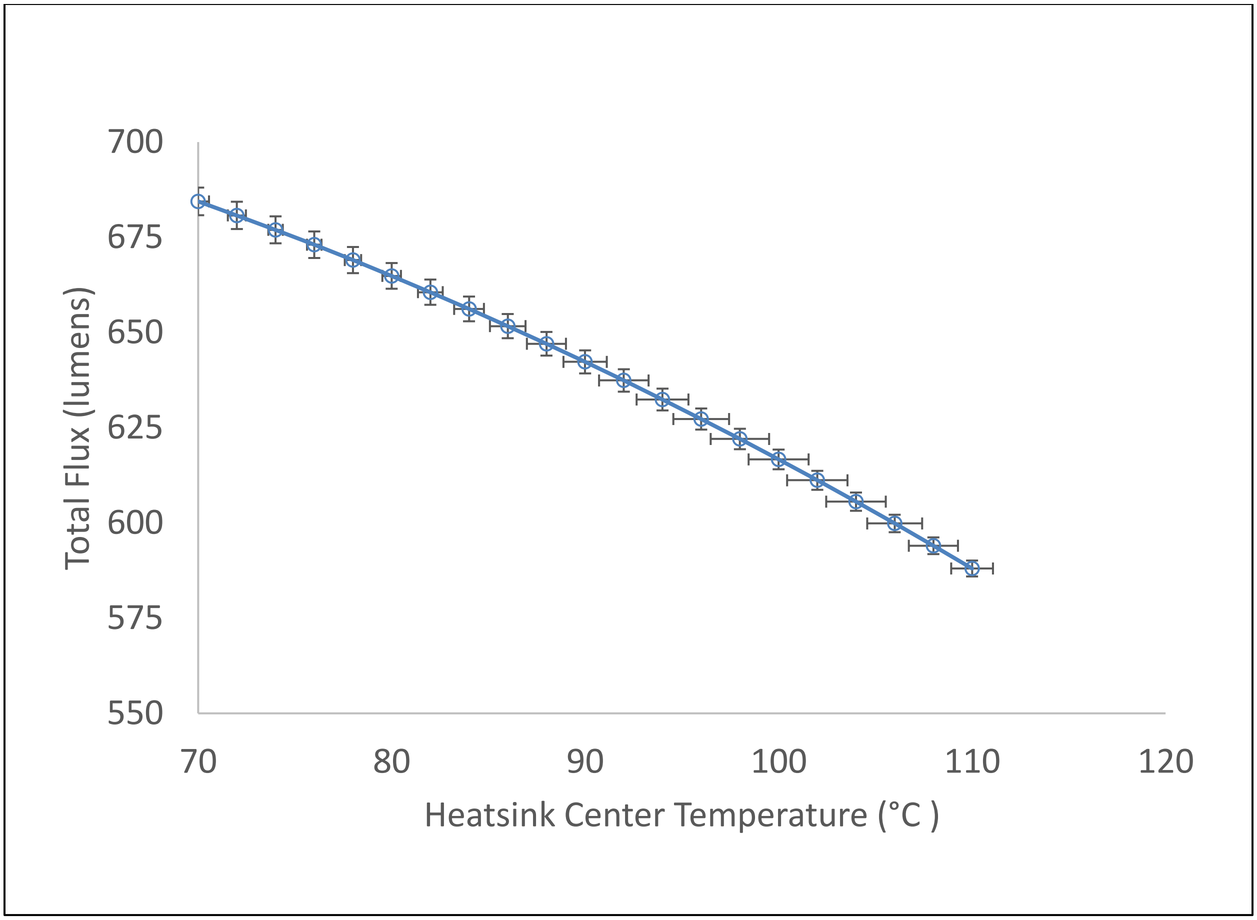

Figure 5.11 Averaged luminous flux over heatsink center temperature, with error bars, data points recorded at 2-minute intervals [50°C/50°C, fan off]

The repeatability analysis demonstrates a high level of consistency across all trials. The data trends from all trials closely align, with the percentage difference remaining below 0.5% throughout. This confirms the LED's optical behavior is consistent under the tested conditions. Furthermore, this analysis was performed across all LED operating configurations, yielding similar results and validating the reliability of the experimental setup for both temperature and light output measurements.

5.6.3 Experimental Limitations

The experimental setup presented several limitations that impacted the execution and scope of the tests. One significant limitation was the thermal limits of styrofoam wall on thermal chamber. Although styrofoam was chosen for its insulation properties, it exhibited structural instability under high-temperature testing scenarios, particularly at the 50°C/85°C ambient condition. The high temperatures air from heat guns caused the styrofoam to deform, creating gaps between panels that compromised the chamber's ability to maintain a stable temperature environment, ultimately affecting the reliability of the experiments. Additionally, the heated styrofoam emitted an odor, raising potential health concerns. Consequently, the maximum temperature conditions for the experiments were reduced to 50°C/50°C to ensure safety and experimental consistency.

Another critical limitation was the operational safety boundary of the LED system. During high-temperature experiments, particularly at the 50°C/85°C ambient condition, the LED heatsink temperature exceeded the 105°C safety limit. This posed a significant risk to the LED units' longevity and performance. To prevent potential damage and preserve the LEDs for future tests, several experiments were prematurely aborted upon reaching this temperature threshold. This safety limitation restricted the ability to fully explore the thermal performance range under more extreme conditions.

Furthermore, the ability to measure temperature within the LED headlamp was constrained by the positioning of thermocouples. Direct temperature measurement at the LED junction was not feasible, as placing a thermocouple in that location would obstruct the light output, thereby affecting the experiment's primary measurements. Due to limited access to the heatsink and the experimental setup, only two thermocouples were attached to each heatsink, restricting the granularity of temperature data available for simulation validation and result analysis.

A further limitation was related to defining and achieving a true steady-state condition. For this experiment, quasi-steady-state was defined as the point where the rate of temperature change (dT/dt) fell below 0.1°C/minute. However, due to time restrictions at the testing facility, it was challenging to reach an absolute steady state with dT/dt equals 0°C/minute for each experiment. Consequently, it is possible that the theoretical steady-state temperature is slightly higher than the experimentally measured value, potentially impacting the completeness of the thermal assessment.

Despite these limitations, the experiments provided valuable data within the defined operational boundaries, offering insights into the thermal behavior and performance of the LED system under varied conditions.

CHAPTER 6 NUMERICAL RESULTS

This chapter presents the numerical results obtained from the CFD simulations, focusing on model validation and the analysis of temperature and flow characteristics within the headlamp. The present results are compared with experimental data to provide a detailed understanding of the system's behavior under various operating conditions.

The flow field analysis examines the velocity and direction of airflow within the headlamp fluid domain under both forced convection (Fan On) and natural convection (Fan Off) conditions. This analysis evaluates the effectiveness of convective cooling by analyzing the flow speed around the LED heatsink and identifying regions of uneven or restricted airflow that could hinder cooling performance. Additionally, the position and geometry of key components, such as the heatsink, reflector, bezel, and cooling fan, are evaluated to determine their impact on airflow distribution and their effect on convective cooling efficiency.

The thermal distribution analysis involves generating detailed temperature distributions across the headlamp fluid domain and the LED heatsink to identify thermal hotspots. These enable a comparison of the thermal performance of the LB1 and LB2 heatsinks under various ambient conditions and convective cooling settings. Furthermore, the analysis quantifies the impact of convective cooling on the thermal distribution within the headlamp.

Based on the flow field and thermal distribution analyses, the weaknesses of the current headlamp design are summarized, the areas where airflow obstructions or insufficient cooling are identified. Key geometric factors such as LED heatsink design, cooling fan position are evaluated for their influence on thermal management. To address these challenges, potential improvement design ideas are proposed. These recommendations aim to improve the thermal performance and reliability of the headlamp system.

6.1 Simulation Validation

Table 6.1 presents a comparison of the simulation results with experimental data, focusing on LED, heatsink center and corner temperatures for LB1 and LB2. The relative errors between the two are included to quantify the accuracy of the simulation.

The simulations and experiments were conducted under identical testing conditions, ensuring consistency in the comparison. Additionally, the temperature monitoring points in the CFD simulations correspond directly to the experimental measurement locations, providing a reliable basis for validation.

For the Fan On (forced convection) cases, LB1 temperature predictions show minor discrepancies, with relative errors within 12% when compared to experimental results. According to Lasance and Poppe (2014), errors in the range of 10–20% are within acceptable limits given the presence of experimental uncertainties, multiphysics interactions, and the use of simplified assumptions and geometries. However, the LB2 temperatures from the simulations are 20–27% higher than the experimental values. This discrepancy can be attributed to differences in the fluid domain design, such as the omission of certain components in the simulation that could influence the airflow, and the exclusion of radiation heat transfer modeling, which may affect the overall heat dissipation.

For the Fan Off (natural convection) cases, the simulations demonstrate low relative errors across all six parameters for both 20°C/20°C and 50°C/50°C conditions. The maximum relative error is 10% for the 20°C/20°C case and 14% for the 50°C/50°C case. These results validate the accuracy of the simulation setup, including the mesh configuration and boundary condition definitions, for predicting natural convection behavior.

Overall, the simulation results align well with the experimental data, except for the LB2 heatsink temperature under the Fan-On conditions. The observed discrepancy may be attributed to uncertainties in material properties, inaccuracies in the fluid domain representation, such as the omission of components that could impact airflow, the exclusion of radiation effects which may have influenced the heat transfer behavior and assumptions of constant LED heating power which neglect the natural derating effect, where the LED heating power changes as the LED temperature increases.

Table 6.1 Comparison of simulation results with experimental data

	LB1			**LB2**		
	Heatsink Center	*Heatsink Corner*	*LED*	*Heatsink Center*	*Heatsink Corner*	*LED*
20°C/20°C Fan On						
Experiment Result (°C)	43.6	39.8	-	64.5	59.0	-
Simulation Result (°C)	46.3	37.0	99.4	77.7	73.6	131.4
Δ Difference (°C)	2.7	-2.8	-	13.2	14.6	-
% Error	6%	-7%	-	20%	25%	-

20°C/20°C Fan Off						
Experiment Result (°C)	89.3	86.1	150.0	89.8	83.9	150.0
Simulation Result (°C)	96.8	86.9	150.6	96.4	92.2	150.5
Δ Difference (°C)	7.5	0.8	0.6	6.6	8.3	0.5
% Error	8%	1%	0%	7%	10%	0%
50°C/50°C Fan On						
Experiment Result (°C)	69.1	65.4	-	88.8	83.5	-
Simulation Result (°C)	77.2	67.8	130.6	110.4	106.3	164.5
Δ Difference (°C)	8.1	2.4	-	21.6	22.8	-
% Error	12%	4%	-	24%	27%	-
50°C/50°C Fan Off						
Experiment Result (°C)	114.7	111.3	172.5	115.2	109.3	172.5
Simulation Result (°C)	129.7	120.2	184.0	129.3	125.1	183.4
Δ Difference (°C)	15.0	8.91	11.5	14.1	15.7	10.9

% Error	13%	8%	7%	12%	14%	6%
*LED temperature was measured from a single LED component-level experiment, only scenarios with the fan off could be performed.						

The simulation results show that the residual values converged, and the temperatures at monitoring points on the heatsinks stabilized, confirming that the system reached steady-state conditions after approximately 25,000 iterations.

6.2 Convective Heat Transfer Analysis

This section focuses on the convective heat transfer analysis of the LED, using calculated *Nu* of LB1 LED as parameter to compare with the STAR CCM+ simulation generated value to validate the physical fidelity of the CFD results. *Nu* is a dimensionless parameter provides a measure of conductive heat transfer occurring at the surface (Bergman et al., 2019, p. 284). This comparison ensures that the simulation accurately predicts the convective heat transfer behavior of the LED under experimental conditions. The analysis covers all four simulation cases: 20°C/20°C Fan On, 20°C/20°C Fan Off, 50°C/50°C Fan On, and 50°C/50°C Fan Off, representing variations in ambient and internal air temperatures as well as forced and natural convection scenarios.

Forced convection and natural convection cases require different approaches to calculate the *Nu*. In forced convection, heat transfer is influenced by external flow from a cooling fan. The Re and Prandtl number (Pr) are used to determine the convective heat transfer regime. These values are calculated using Equations (6.1) and (6.2):

$$Re = \frac{\rho\, v\, L}{\mu} \tag{6.1}$$

where ρ is the air density and μ is the dynamic viscosity at corresponding internal ambient temperature from experiment measurement, v is the air velocity at LB1 LED (obtained from the STAR-CCM+ simulation), L is the LED characteristic length.

$$Pr = \frac{C_P \, \mu}{k} \tag{6.2}$$

where C_P is specific heat capacity of air (J/kg·K), k is thermal conductivity of the air (W/m·K).

For all cases analyzed, the calculated Re at LB1 LED remains below 2000, confirming laminar flow conditions. The Nu for laminar flow is calculated using the following equation:

$$Nu = 0.664 \, Re^{\frac{1}{2}} Pr^{\frac{1}{3}} \tag{6.3}$$

For natural convention, heat transfer arises from buoyancy forces caused by temperature gradients. The Grashof number (Gr) and Rayleigh number (Ra) are key parameters in determining the convective regime.

$$Gr = \frac{g \, \beta \, \Delta T \, L^3}{v^2} \tag{6.4}$$

where g is gravitational acceleration $\left(\frac{m}{s^2}\right)$, β is coefficient of thermal expansion $(1/K)$, defined as $\beta = \frac{1}{T_{internal\ ambient}}$ for ideal gas, ΔT is temperature different between T_{LED} and $T_{internal\ ambient}$, v is kinematic viscosity (m^2/s). For natural convection, L is defined as:

$$L = \frac{A}{P} \tag{6.5}$$

where A is surface area through which heat transfer occurs, and P is perimeter of the surface exposed to the fluid. Therefore, calculated L for LED under natural convection case is 0.00094 m.

Ra is calculated as:

$$Ra = Gr \cdot Pr \tag{6.6}$$

For the natural convection cases analyzed, the calculated Ra are below 10^4, indicating very weak natural convection. In such cases, the flow remains nearly stagnant, and the Nu is assumed to be $Nu = 1$, indicating that heat transfer is primarily conduction-dominated with negligible convection. These natural convection conditions result in lower Nu compared to forced convection scenarios, where external airflow from fan drive the fluid motion and enhance convective heat transfer. as seen in Table 6.2.

Table 6.2 Comparison of calculated Nu with STAR CCM+ result on LB1 LED

	20°C / 20°C, Fan On	**20°C / 20°C, Fan Off**	**50°C / 50°C, Fan On**	**50°C / 50°C, Fan Off**
Re	946.5	1.4	793.8	1.3
Gr	-	2.9	-	2.2
Ra	-	2.1	-	1.7
Calculated Nu	18.05	1*	16.95	1*
Simulation Generated Nu	18.48	4.10	15.86	3.70
% Error	2%	-	6%	-

**Based on the calculated Ra value, for Ra < 10^4, Nu is assumed to be 1.*

In forced convection cases, the STAR-CCM+ results align closely with calculated Nu, validating the robustness of the CFD model in capturing laminar forced convection phenomena at LB1 LED region.

In natural convection cases, the large discrepancy between simulation-generated Nu and calculated Nu can be attributed to the imperfect boundary layer setup which capture the local heat transfer, exclusion of radiation heat transfer, and discrepancy between reality and the modeling assumptions (Lasance & Poppe, 2014).

6.3 Flow Characteristics of the LED Headlamp

This section analyzes the fluid flow field using three planes, V1, V2, and V3 (refer to Figure 4.6 and Table 4.6), focusing on the flow field near the LB1, cooling fan, and LB2 domains. These planes provide a detailed evaluation of airflow patterns and their interaction with the solid components, including heatsinks, reflector and bezel. By comparing the airflow direction and magnitude around the heatsinks under natural and forced convection conditions, this analysis evaluates convective cooling performance and identifies potential design improvements.

Figure 6.1 illustrates the V1 view with velocity field distribution and stream traces under the Fan On condition. The figures contours in this section use a normalized air velocity value U_{max}, which is defined as the initial velocity at the top surface of the cooling fan, where the airflow is directed upward. In the boundary condition setup, this velocity is specified as 3.56 m/s.

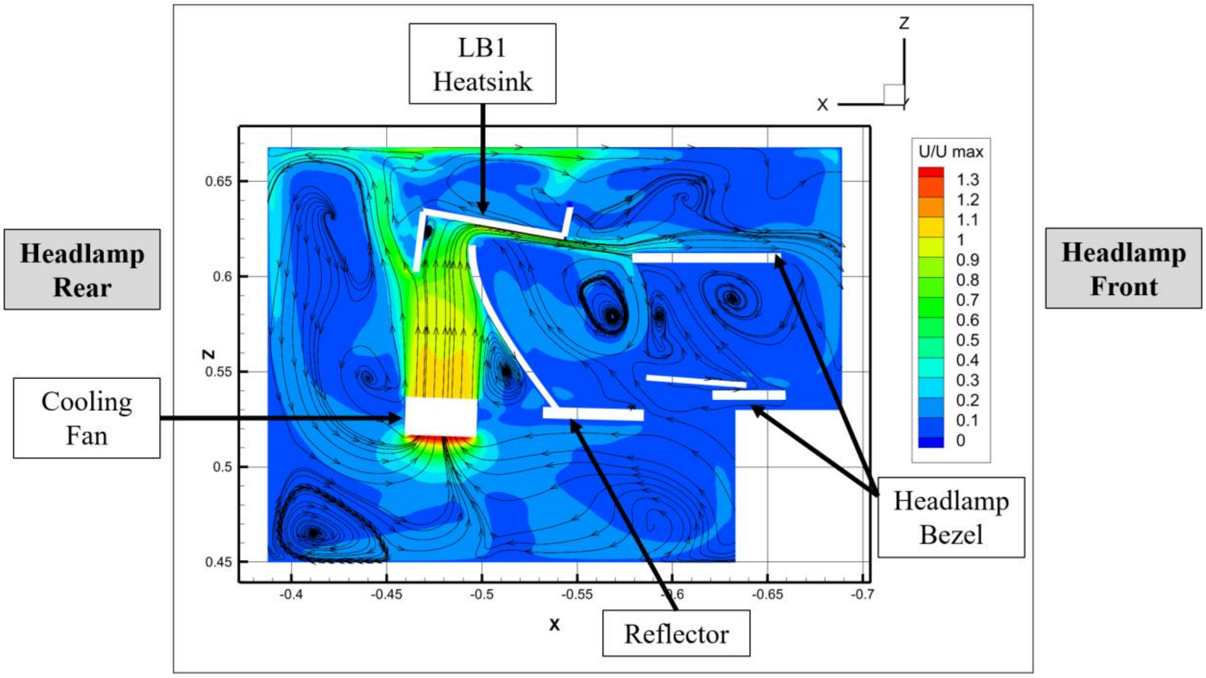

Figure 6.1 Velocity field distribution in the plane V1 [20°C/20°C, Fan On]

The high-velocity airflow efficiently targets the lower surface of the LB1 heatsink, where the PCB and LED are located. The majority of the high-velocity airflow from the cooling fan is directed toward the lower surface of the LB1 heatsink. The narrow gap between the top of the reflector and the LB1 heatsink constrict the airflow causing it to accelerate as it passes through the gap between reflector and heatsink. This creates a localized high-velocity jet in the region, with a velocity of approximately 0.83 U_{max} as the air moves past the LED. This high velocity impinges on the lower surface of the heatsink providing for improved convective heat transfer.

A portion of the fan airflow is distributed to the rear section of the LB1 heatsink. However, due to the heatsink's design and the absence of dedicated flow channels in the headlamp, the velocity field across the upper surface of the heatsink only receives low airflow velocity, approximately

0.36 U_{max}. This low airflow velocity results in diminished cooling efficiency in the top section of the heatsink, limiting its ability to effectively dissipate heat.

Figure 6.2 illustrates the V3 front cross-sectional view of the fluid field, focusing on the interaction between the airflow and both LB1 and LB2 heatsinks. Due to its position closer to the rear of the headlamp, the LB2 heatsink is not visible on the displayed plane. However, its relative location is indicated within the orange box for clarity.

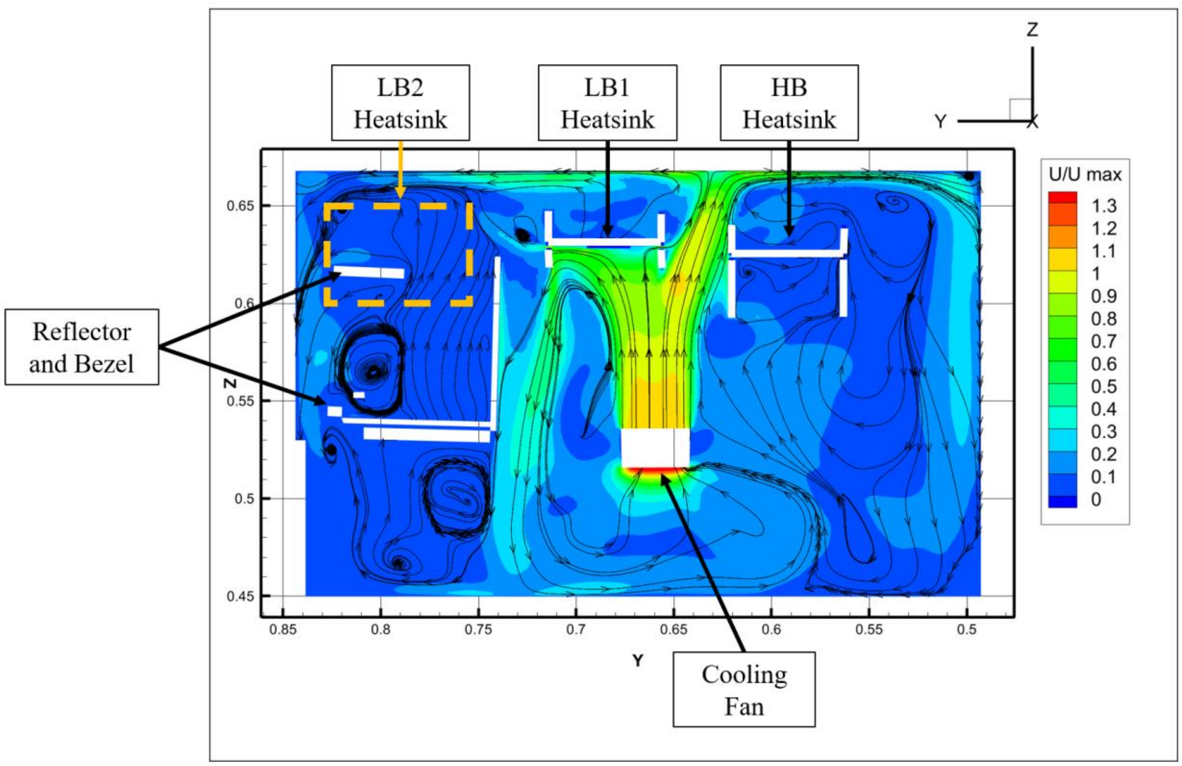

Figure 6.2 Velocity field distribution in plane V3 [20°C/20°C, Fan On]

High-velocity airflow from the cooling fan is directed primarily upward toward the LB1 heatsink. A portion of this airflow is diffused by one of the lower fins on the LB1 heatsink, with some air being guided toward the lower surface of the heatsink. As the airflow passes over the lower surface, its velocity decreases and recirculates toward the lower section of the fluid domain. The remaining airflow diffuses through the gap between the LB1 and HB heatsinks, spreading to the upper sections of the fluid domain and dispersing in multiple directions.

As Figure 6.3 shows, the airflow reaching the LB2 heatsink is significantly obstructed by the reflector and bezel, resulting in reduced and non-uniform velocities near LB2. On the V2 plane, air velocities towards LB2 range reduced to 0.06 U_{max}, compared to 0.8 U_{max} near LB1. Moreover, the positioning and orientation of the cooling fan results in LB2 receiving no direct airflow, further diminishing its *h* and contributing to higher operating temperatures compared to LB1.

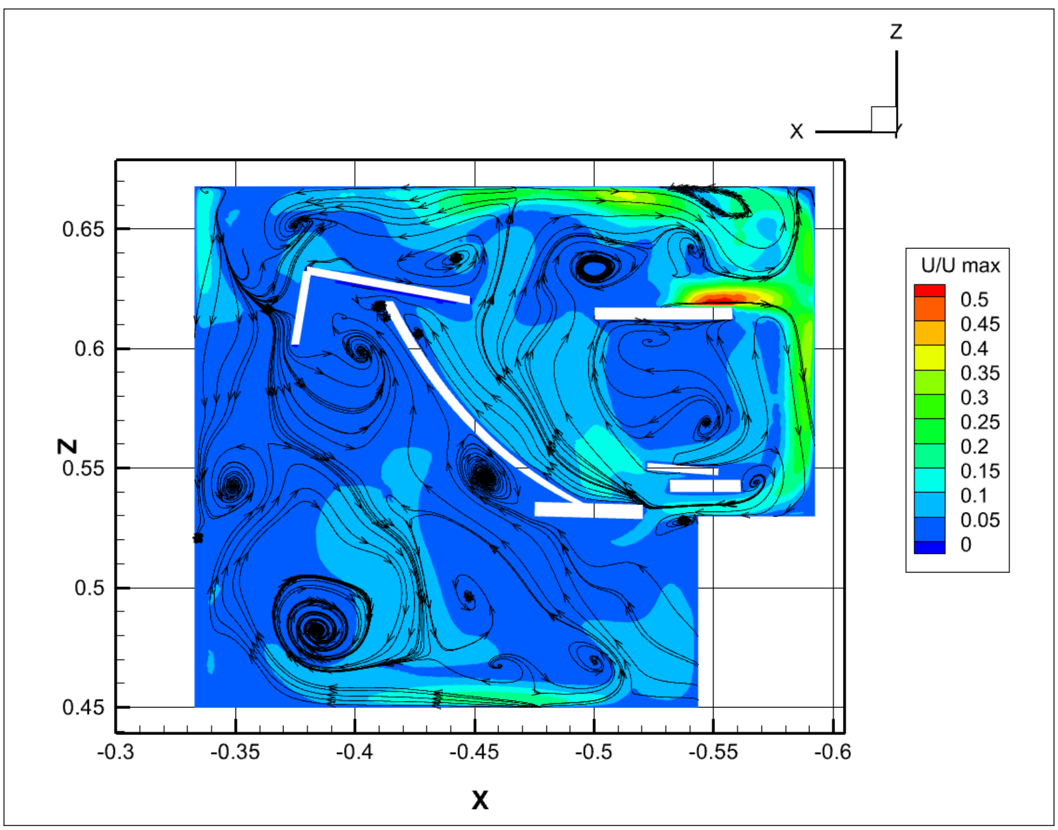

Figure 6.3 Velocity field distribution in the plane V2 [20°C/20°C, Fan On]

To improve the cooling performance of LB2, several strategies can be implemented. Introducing airflow guides or channels can provide direct airflow toward LB2, increasing the air velocity and enhancing its cooling efficiency. Additionally, reducing obstructions caused by the reflector and bezel can minimize velocity drops and ensure more uniform airflow around LB2. Adjusting the fan angle or position, or incorporating a secondary cooling fan, could further balance airflow distribution between LB1 and LB2. These modifications would promote effective and consistent cooling across the system.

Figures 6.4 (a) and (b) illustrate the velocity distribution within the fluid domain around the LB1 and LB2 heatsinks, under the natural convection condition. In the absence of forced convection from the cooling fan, the air velocity across both planes is significantly reduced, with a maximum velocity of 0.04 U_{max} compared to 1.4 U_{max} observed in the Fan On case. The velocity distribution under natural convection is concentrated near the upper section of the heatsink, where thermal buoyancy forces drive airflow. In contrast, the lower region of the fluid domain exhibits near-stagnant conditions, with negligible airflow observed.

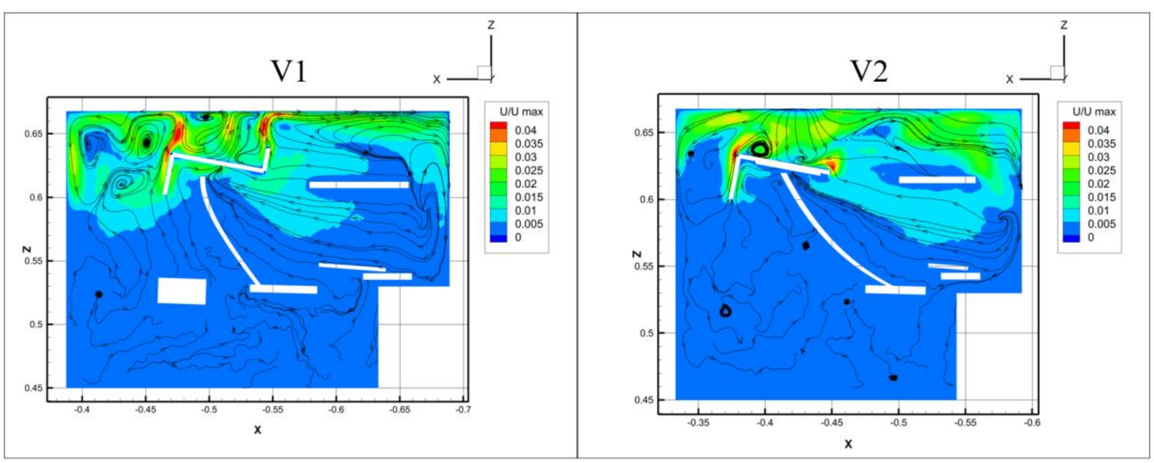

Figure 6.4 Velocity field distributions in (a) plane V1 and (b) V2 [20°C/20°C, Fan On]

Under natural convection, airflow is governed by temperature-induced density variations within the fluid domain. Some air recirculation is observed near the headlamp surrounding moving vertically on heatsink upper surface and travel horizontally from lower heatsink surface toward the front section of the headlamp. However, the velocity magnitudes in this scenario remain much lower compared to the forced convection case, limiting the overall effectiveness of heat dissipation.

In conclusion, the flow field analysis reveals that forced convection is a critical mechanism for enhancing air velocity, leading to higher Nu and heat transfer coefficients ($h_{LB1\ LED}$ = 97.9 $\frac{W}{m^2.K}$), which significantly improves the overall convective cooling performance. The presence of a direct, high-velocity airflow is especially important for maximizing heat dissipation efficiency.

The geometry of the fluid domain strongly influences the magnitude and direction of convective airflow patterns. The interaction between the airflow and the heatsink, particularly at the lower surface of the LB1 heatsink, demonstrates the effectiveness of the cooling fan's positioning in directing airflow toward critical heat-generating areas. However, the LB1 heatsink upper surface and LB2 heatsink suffers from low airflow velocity due to the lack of air channel, resulting in localized stagnation and diminished heat dissipation performance.

These findings present opportunities for design improvement. Modifying the heatsink's perpendicular fin geometry to a more streamlined or rounded design could reduce flow resistance and increase airflow velocity. Additionally, implementing airflow guides or channels could direct high-velocity airflow toward the heatsink's upper surface, improving convective heat transfer. These adjustments would promote uniform and efficient heat dissipation, enhancing the overall thermal management of the headlamp system.

6.4 Thermal Distribution Analysis of the LED Headlamp

This section analyzes the temperature distribution in both the solid components and the surrounding fluid field under f and Fan Off conditions. It examines the temperature distribution on the upper surface s of the heatsinks, provides cross-sectional views of the fluid domain near LB1 and LB2, evaluates the effectiveness of forced and natural convection cooling, and identifies weaknesses in the current design.

Figure 6.5 shows the temperature distribution on the upper surface of the LB1 heatsink under 20°C/20°C Fan On conditions. The temperature distribution reveals that the front sections of the heatsink are significantly hotter than the rear sections, with the highest temperature located directly at the T_{center} measurement point, where is above the LED. This localized heating creates a thermal hotspot in the region above the LED, while the temperature decreases progressively as the distance from the LED increases. The temperature gradient drives the heat transfer from the LED through PCB to the surrounding heatsink area, primarily through thermal conduction, distributing the heat toward the corners of the heatsink. This uneven temperature distribution could be mitigated through design improvements, such as incorporating vertical fins above the LED junction or extended surfaces at the front section of the heatsink to enhance heat dissipation by increasing the surface area for convection and reducing the conduction path length, lowering the thermal resistance. Additionally, selecting high thermal conductivity materials, such as copper with a thermal conductivity of 398 W/m·K (Lasance & Poppe, 2014), could further enhance conductive cooling performance.

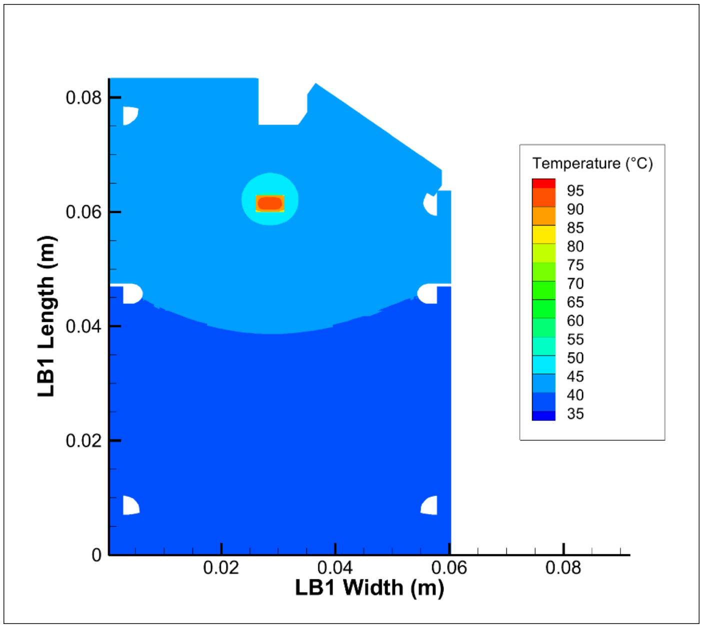

Figure 6.5 LB1 heatsink upper surface thermal distribution [20°C/20°C, Fan On]

Figures 6.6 and 6.7 compare the temperature distribution along both the longitudinal and transverse axes of the LB1 and LB2 heatsinks under 20°C/20°C Fan On and fan off conditions. For the axis locations, refer to Figure 4.7, which illustrates the longitudinal and transverse measurement axes on the heatsink.

Under Fan On conditions, LB1 heatsink exhibits lower overall temperatures than LB2 heatsink, demonstrating the effectiveness of forced convection in reducing LED and heatsink temperatures. This aligns with the conclusions from Chapter 5, which identified LB2 as the thermal hotspot within this LED headlamp design due to the restricted air flow from cooling fan.

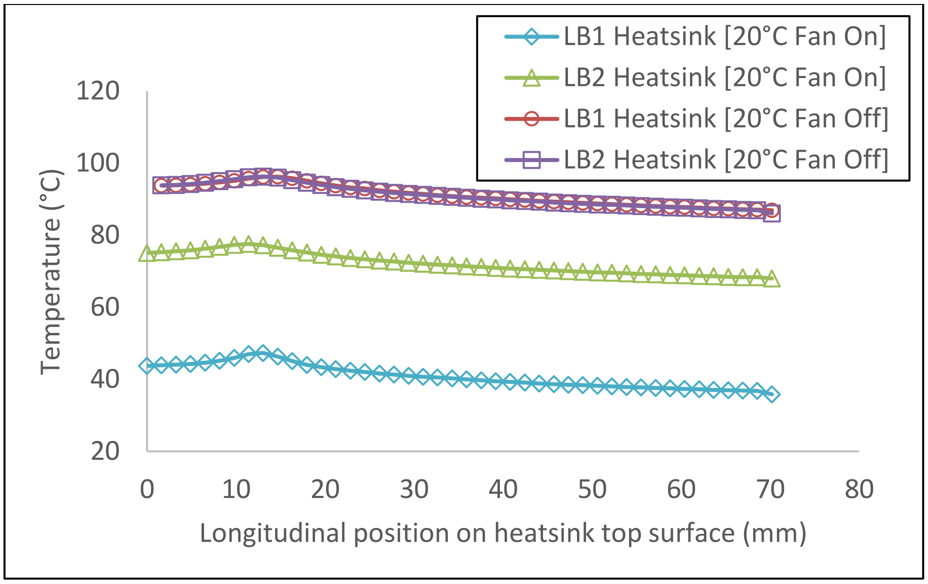

Figure 6.6 Temperature distribution on longitudinal axis of heatsink upper surface [20°C/20°C]

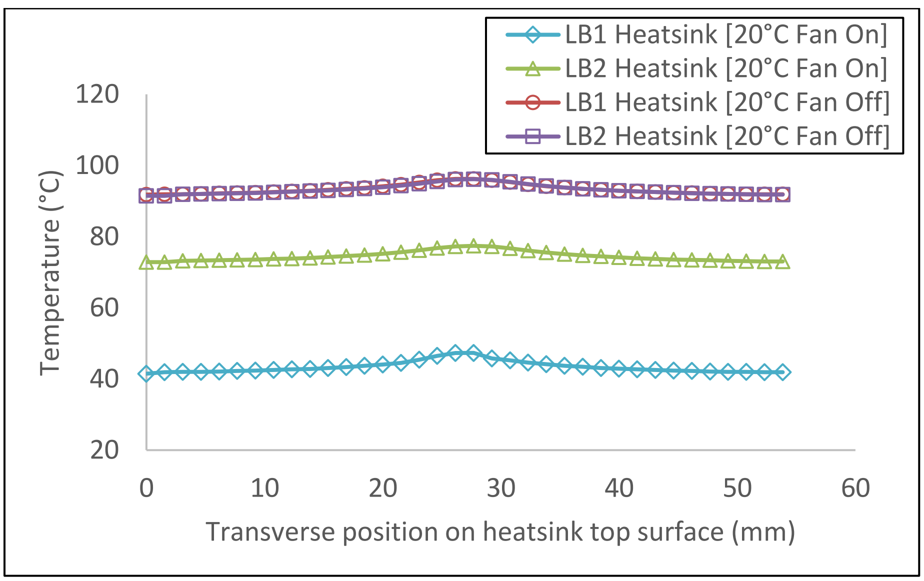

Figure 6.7 Temperature distribution on transverse axis of heatsink upper surface [20°C/20°C]

In contrast, under fan-off conditions, CFD simulations show that both LB1 and LB2 LED units exhibit nearly identical temperature distributions despite their differing positions within the headlamp. Without high-velocity airflow from the cooling fan, the fluid domain remains stagnant, creating a uniform thermal environment around both LB1 and LB2. Heat dissipation is primarily driven by conduction, which operates similarly for both units, and, combined with identical LED heating power, results in similar temperature distributions.

Figures 6.8 and 6.9 present cross-sectional views of the fluid field temperature near LB1 and LB2. These views correspond to the positions identified as V1 and V2 in Figure 4.6 and Table 4.6, illustrating the interaction between the heatsink and the surrounding fluid domain.

In Figure 6.8, under Fan On conditions, the LB1 heatsink temperature closely aligns with the surrounding fluid temperature, exhibiting a reduction of approximately 50°C compared to LB1 heatsink in the Fan Off case. This significant temperature decrease is due to the active air circulation generated by forced convection, which promotes a more uniform heat distribution within the fluid domain. Conversely, under Fan Off conditions, the temperature difference between the heatsink and the surrounding fluid becomes pronounced, reaching up to 70°C. The lack of forced airflow leads to weaker buoyancy-driven fluid motion, significantly reducing convective heat transfer and resulting in localized hot spots on the heatsink.

Figure 6.9 shows the V2 view focusing on the LB2 heatsink fluid region. Under Fan On conditions, the airflow from the cooling fan is significantly restricted near LB2 due to its greater distance from the fan and obstructions caused by the reflector. Consequently, the LB2 heatsink temperature is approximately 50°C higher than LB1, demonstrating the diminished effectiveness of forced convection for LB2. The reduced airflow velocity near LB2 also leads to a less uniform temperature distribution in the surrounding fluid domain. Without sufficient airflow recirculation, the convection heat transfer is weakened, resulting in inefficient heat dissipation and uneven temperature gradients.

Despite the restricted air flow from cooling fan, forced convection still outperforms natural convection in cooling performance. Under Fan Off conditions, the absence of active airflow leads to weaker buoyancy-driven fluid motion, drastically reducing convective heat transfer and causing localized hot spots on the LB2 heatsink. The heated air above the LB2 heatsink rises due to density changes, while cooler, denser air stagnates in the lower section of the fluid domain, further limiting the heat transfer effectiveness.

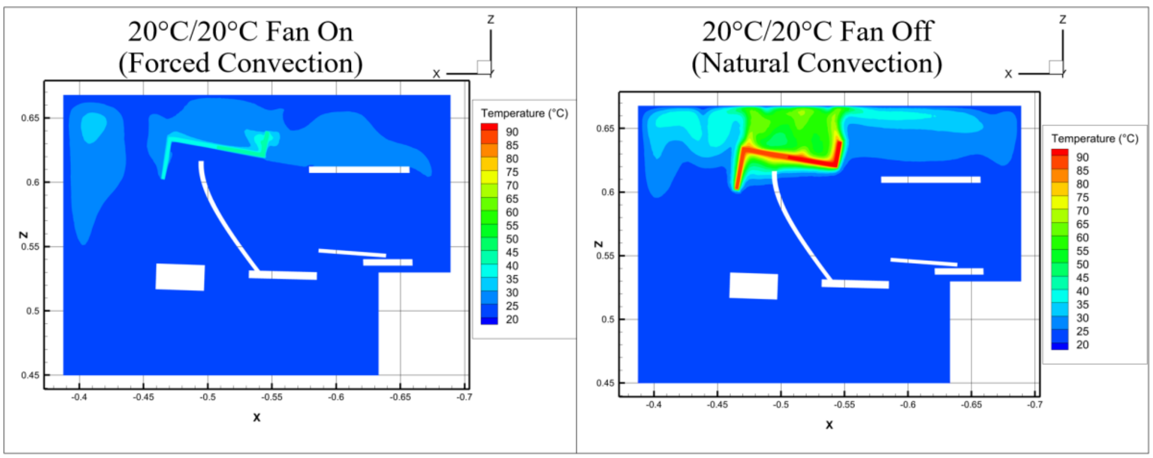

Figure 6.8 Temperature distribution comparison of plan V1 [20°C/20°C]

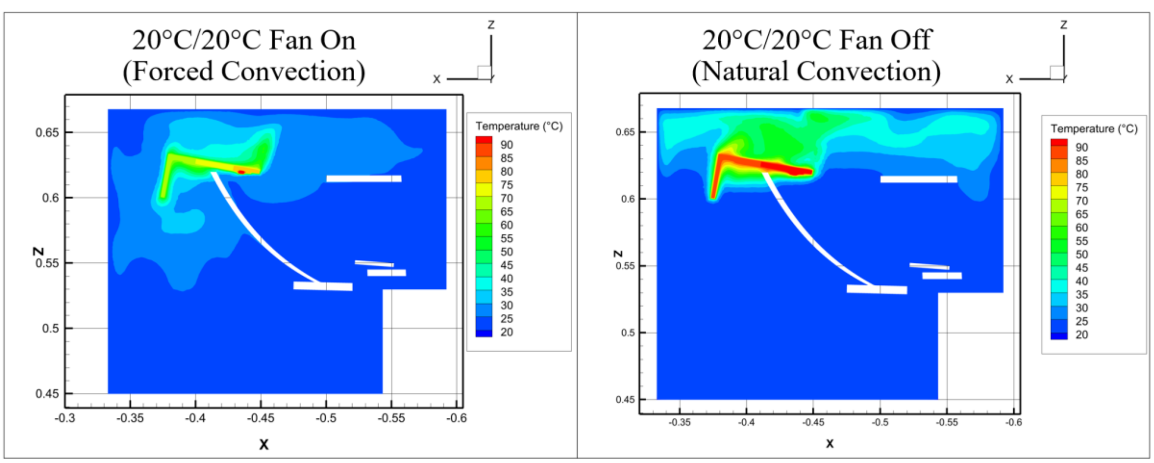

Figure 6.9 Temperature distribution comparison of plan V2 [20°C/20°C]

These findings emphasize the critical role of forced convection in achieving effective thermal management and highlight areas for potential design improvements. Incorporating high-conductivity materials, reducing conduction path lengths, and improving airflow paths can significantly enhance heat dissipation, ensuring optimal performance and longevity for the LED system.

CHAPTER 7 CONCLUSIONS AND RECOMMENDATIONS

7.1 Conclusions

This study investigated the thermal and optical behavior of two identical LED units inside the automotive headlamp using both experiments and CFD simulations. The experiments analyzed the LED headlamp's performance under various environmental temperature conditions, comparing cooling strategies such as natural and forced convection and the use of active LED derating control system. A simplified 3D CFD model was developed using STAR CCM+ commercial software to further examine the temperature distributions and airflow characteristics inside the headlamp. Based on the findings, the following conclusions are drawn:

- High ambient temperatures surrounding the LED headlamp significantly affect heatsink heat dissipation, resulting in elevated LED temperatures.
- Forced convection cooling using a cooling fan significantly improves LED thermal management, reducing the LB1 heatsink temperature by up to 51% compared to natural convection under identical conditions.
- Airflow distribution around the LED heatsinks is strongly influenced by their relative positioning to the cooling fan. Obstructions caused by internal components, such as the reflector, limit airflow to the LB2 heatsink. This creates air stagnation zone surrounding LB2 LED unit and making it the system's thermal hotspot.
- The complexity of the flow field within the headlamp requires careful consideration during CFD model design and setup to ensure accurate simulation results.
- The CFD simulations demonstrate acceptable correlation with experimental results for forced convection cases, with a temperature difference of ±10%. However, larger

discrepancies are observed in natural convection simulations, particularly for the LB2 heatsink temperature.

- Forced derating algorithm from SLM can effectively prevent LED from overheating, but it significantly reduces the light output and creates light flickering, posing safety risks in real applications.

7.2 Recommendations for Future Work

The following recommendations for future work and headlamp cooling design are made to improve the understanding of LED headlamps thermal management.

- During high ambient temperature testing, hot air from heat guns can deform or melt the styrofoam in the thermal chamber. For tests at temperatures 85°C and above, it is recommended to either reduce the hot air inlet temperature or replace the styrofoam with a material that has a higher melting point to ensure reliable testing.
- Some experiments did not reach steady-state conditions due to time constraints, exceeding thermal chamber limitations or LED maximum temperature. Repeating these experiments with extended durations or implementing accurate extrapolation methods to predict quasi-steady state results is recommended.
- Investigate the effects of external airflow on the LED headlamp's thermal performance to replicate real-world conditions when the vehicle is in motion.
- Investigate the effect of humidity on LED headlamp's thermal performance to replicate real-world condition with varying humidity levels.
- Include radiation model in CFD simulation to further improve the accuracy of the simulation.

- Conduct experiments to measure the heating power of the LED at different junction temperatures. Implement a field function in the CFD simulation to account for the temperature-dependent variation in heating power, improving simulation accuracy.
- Perform CFD studies to optimize airflow by changing the position of the cooling fan to enhance the cooling performance of the system.
- Incorporate thermal imaging into experiments to provide a comprehensive overview of the temperature distribution across the headlamp assembly and LED units.

7.3 LED Thermal Management Design Improvements

Based on the findings from experimental and CFD analysis of the LED headlamp of 2021 Jeep Grand Cherokee, the following design improvement ideas are proposed:

- To address the higher temperatures of the LB2 unit, consider adding a secondary cooling fan below the LB2 heatsink to enhance cooling and lower its operating temperature.
- Effective airflow management is essential for efficient convective cooling. Enhancements to the LED heatsink design, such as increasing the number of fins and expanding the surface area, along with incorporating an air diffuser, could improve airflow distribution, minimize obstructions, and enhance convective heat transfer. These improvements would optimize the overall cooling performance of the system.
- Elevated ambient temperatures significantly increase the thermal load on the LED headlamp. Reducing the T_{rear} could be achieved by increasing the distance between the headlamp and the engine or introducing additional cooling mechanisms for the headlamp housing, such as external air vents or thermal insulation.

REFERENCES/BIBLIOGRAPHY

1. *Linkov, J. (2019). LED headlights can be brighter but often lack clear advantages. Consumer Reports. Retrieved February 16, 2023, from https://www.consumerreports.org/headlights/led-headlights-can-be-brighter-but-often-lack-clear advantages/#:~:text=Automakers%20have%20embraced%20light%20emitting,tested%2C%2086%20percent%20had%20LEDs.*

2. *Lasance, C. J. M., & Poppe, A. (Eds.). (2014). Thermal management for LED applications. Solid State Lighting Technology and Application Series 2. Springer Science+Business Media New York. https://doi.org/10.1007/978-1-4614-5091-7_7*

3. *Roberts, S. (2009). Thermal derating of LEDs.*

4. *ams-OSRAM AG. (2022). Thermal management of light sources based on SMD LEDs. https://ams-osram.com/Tang, Z., Fan, J., Chen, W., Li, Y., Mohamed, M. G., & Li, R. (2019).*

5. *Optimal Thermal Design of LED automotive headlamp with the Response Surface Method. 2019 16th China International Forum on Solid State Lighting & 2019 International Forum on Wide Bandgap Semiconductors China (SSLChina: IFWS). https://doi.org/10.1109/sslchinaifws49075.2019.9019807*

6. *Wang, J., Cai, Y.-xi, Zhao, X.-jie, & Zhang, C. (2014). Thermal design and simulation of automotive headlamps using white leds. Microelectronics Journal, 45(2), 249–255. https://doi.org/10.1016/j.mejo.2013.11.011*

7. *Zhao, X.-J., Cai, Y.-X., Wang, J., Li, X.-H., & Zhang, C. (2015). Thermal model design and analysis of the high-power LED automotive headlight cooling device. Applied Thermal Engineering, 75, 248–258. https://doi.org/10.1016/j.applthermaleng.2014.09.066*

8. *Qin, Y., Cai, M., Chen, X., Li, J., Yang, D., & Zhang, G. (2021). Thermal and optical modeling on intelligent LED headlights. 2021 22nd International Conference on Electronic Packaging Technology (ICEPT). https://doi.org/10.1109/icept52650.2021.9568193*

9. *Triyono, B., Muliastri, D., & Eka Septiyani, D. A. (2023). The Characterization of Mechanical and Chemical Properties of Recycled styrofoam Waste Employing Extrusion Process. In Jurnal Rekayasa Mesin (Vol. 18, Issue 2). https://jurnal.polines.ac.id/index.php/rekayasa*

10. *S. Prasad, D. Devaraj, R. Boddula, S. Salla,M.S. AlSalhi, Fabrication, device performance, and MPPT for flexible dye-sensitized solar panel based on gel-polymer phthaloylchitosan based electrolyte and nanocluster CoS2 counter electrode,Mater.Sci.EnergyTechnol.2(2019)319–328.*

11. *Yao, H., Li, Y., Zhang, Y., Lv, Z., Wei, X., Song, H., Qin, H., & Zou, J. (2022). Failure Mechanism and Analysis Diagnosis of LED. MAPAN, 37(1), 195–206. https://doi.org/10.1007/s12647-021-00518-1*

12. *Pattison, P. M., Hansen, M., & Tsao, J. Y. (2018). LED lighting efficacy: Status and directions. C. R. Physique, 19(3), 134-145.*

13. *Kachi, S., Bensouici, F.-z., Ferroudj, N., & Boudebous, S. (2019). Effect of Richardson number on unsteady mixed convection in a square cavity partially heated from below. Fluid Dynamics & Materials Processing, 15(2), 89–105. https://doi.org/10.32604/fdmp.2019.00263*

14. *Huang, D.-S., Chen, T.-C., Tsai, L.-T., & Lin, M.-T. (2019). Design of fins with a grooved heat pipe for dissipation of heat from high-powered automotive LED headlights. Energy Conversion and Management, 180, 550–558. https://doi.org/10.1016/j.enconman.2018.11.021*

15. *Yao, H., Li, Y., Zhang, Y., Lv, Z., Wei, X., Song, H., Qin, H., & Zou, J. (2022). Failure Mechanism and Analysis Diagnosis of LED. MAPAN, 37(1), 195–206. https://doi.org/10.1007/s12647-021-00518-1*

16. *Bridgelux, Inc. (2011, February 4). Effective thermal management of LED arrays. Digi-Key. https://www.digikey.com/en/articles/effective-thermal-management-of-led-arrays*

17. *Chang, W. S., Das, D., Vasan, A. S. S., & Pecht, M. (2011). Junction temperature characterization of high power light emitting diodes. CALCE EPSC Press. Retrieved from https://www.prognostics.umd.edu/calcepapers/11-Chang_Junction_Temp_Char_LED.pdf*

18. *Fan, A., Bonner, R., Sharratt, S., & Ju, Y. S. (2012). An innovative passive cooling method for high-performance light-emitting diodes. 28th IEEE SEMI-THERM Symposium. https://doi.org/10.1109/SEMI-THERM.2012.6188867*

19. *Ribas, X., & Hudson, T. (2022). Using thermal derating to extend automotive LED life expectancy: A simple and cost-effective solution. Monolithic Power Systems. https://media.monolithicpower.com/mps_cms_document/2/0/2021-aip-using-thermal-derating-to-extend-automotive-led-life-expectancy_r1.0.pdf*

20. *Ngo, I. L., Yu, X., Jang, S. K., & Byon, C. (2018). Experimental study on thermal management of surface mount device–LED chips towards applicability in a headlamp of modern cars.*

Applied Thermal Engineering, 128, 1226-1235. https://doi.org/10.1016/j.applthermaleng.2022.119846

21. *Pearce, J., Tucker, D., Izquierdo, C. G., Caballero, R., Ford, T., Williams, P., & Cowley, P. (2022). Correlation Between Insulation Resistance and Temperature Measurement Error in Type K and Type N Mineral Insulated, Metal Sheathed Thermocouples. International Journal of Thermophysics, 43(3). https://doi.org/10.1007/s10765-021-02967-x*

22. *Manjhi, S. K., & Kumar, R. (2019). Transient surface heat flux measurement for short duration using K-type, E-type and J-type of coaxial thermocouples for internal combustion engine. Measurement, 136, 256–268. https://doi.org/10.1016/j.measurement.2018.12.070*

23. *Kozai, T., Fujiwara, K., & Runkle, E. S. (Eds.). (2016). LED Lighting for Urban Agriculture. Springer. https://doi.org/10.1007/978-981-10-1848-0*

24. *Ohno, Y. (1997). NIST Measurement Services: Photometric Calibrations. NIST Special Publication 250-37, Gaithersburg, Maryland, 66 pp.*

25. *Rongier, C., Gilblas, R., Le Maoult, Y., Belkessam, S., & Schmidt, F. (2022). Infrared thermography applied to the validation of thermal simulation of high luminance LED used in automotive front lighting. Infrared Physics & Technology, 120, 103980. https://doi.org/10.1016/j.infrared.2021.103980*

26. *Tang, Z., Fan, J., Chen, W., Li, Y., Mohamed, M. G., & Li, R. (2019). Optimal Thermal Design of LED automotive headlamp with the Response Surface Method. 2019 16th China International Forum on Solid State Lighting & 2019 International Forum on Wide*

Bandgap Semiconductors China (SSLChina: IFWS). https://doi.org/10.1109/sslchinaifws49075.2019.9019807

27. *Wang, J., Cai, Y.-xi, Zhao, X.-jie, & Zhang, C. (2014). Thermal design and simulation of automotive headlamps using white leds. Microelectronics Journal, 45(2), 249–255. https://doi.org/10.1016/j.mejo.2013.11.011*

28. *Zhao, X.-J., Cai, Y.-X., Wang, J., Li, X.-H., & Zhang, C. (2015). Thermal model design and analysis of the high-power LED automotive headlight cooling device. Applied Thermal Engineering, 75, 248–258. https://doi.org/10.1016/j.applthermaleng.2014.09.066*

29. *Qin, Y., Cai, M., Chen, X., Li, J., Yang, D., & Zhang, G. (2021). Thermal and optical modeling on intelligent LED headlights. 2021 22nd International Conference on Electronic Packaging Technology (ICEPT). https://doi.org/10.1109/icept52650.2021.9568193*

30. *Wu, Q., Liang, C., & Huang, L. (2020). Thermal design and simulation of leds automotive headlamps. 2020 21st International Conference on Electronic Packaging Technology (ICEPT). https://doi.org/10.1109/icept50128.2020.9202953*

31. *Treurniet, T. (2014). LED platform development. In C. J. M. Lasance & A. Poppe (Eds.), Thermal management for LED applications (pp. 449–465). Springer Science+Business Media. https://doi.org/10.1007/978-1-4614-5091-7_12*

32. *van Driel WD, Yuan CA, Koh S, Zhang GQ (2011) LED system reliability, thermal, mechanical and multi-physics simulation and experiments in microelectronics and microsystems (EuroSimE), 12th international conference on pp 1/5–5/5*

33. *Liu L, Yang D, Zhang GQ, You Z, Hou F, Liu D (2011) Thermal performance analysis of photoelectric parameters on high power led packaging modules, thermal, mechanical and multi-physics simulation and experiments in microelectronics and microsystems (EuroSimE),12th international conference on, pp 1/5–5/5*

34. *Liu, J., Tam, W. S., Wong, H., & Filip, V. (2009). Temperature-dependent light-emitting characteristics of InGaN/GaN diodes. Microelectronics Reliability, 49(1), 38–41. https://doi.org/10.1016/j.microrel.2008.09.013*

35. *Chang, M.-H., Das, D., Varde, P. V., & Pecht, M. (2012). Light-emitting diodes reliability review. Microelectronics Reliability, 52(5), 762–782. https://doi.org/10.1016/j.microrel.2011.07.063*

36. *Bergman, T. L., & Levine, A. S. (2019). Fundamentals of heat and mass transfer. John Wiley & Sons, Inc.*

Appendix A COOLING FAN SPECIFICATION

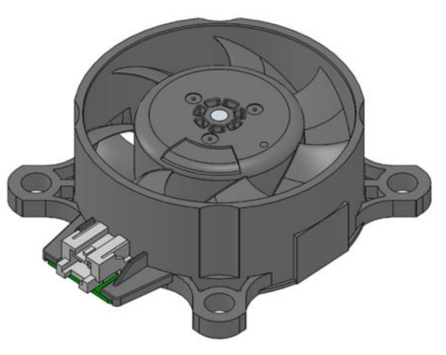

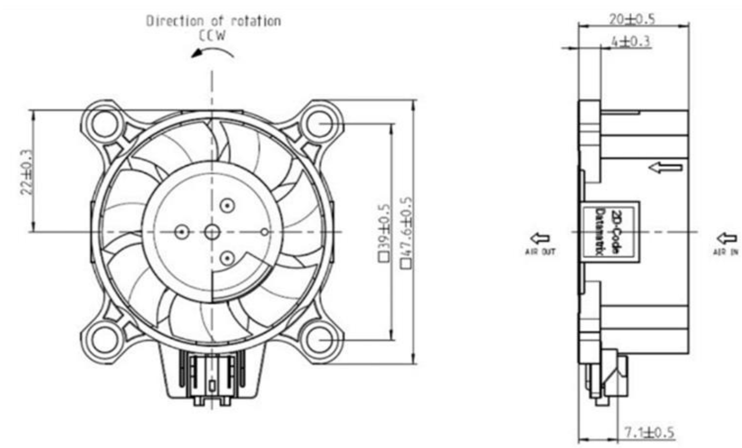

Figure A.1 Drawing of cooling fan (unit: mm)

Appendix B EXPERIMENT PROCEDURES

This section explains the experiment procedures, starting and stopping criteria for the LED headlamp thermal and optical measurement experiment.

Starting and Stopping Criteria

To accurately record the dynamic response of LED headlamp system to temperature changes, the starting criteria of experiment need to be controlled.

The camera-based photometry system is calibrated at the beginning of every experiment day to maintain accurate light measurements. The wiring connections, thermocouple attachments, and thermal chamber integrity are checked to verify secure connections and that the chamber is sealed and intact.

Before starting the experiment and collecting light output and temperature data, the internal air of thermal chamber and the testing headlamp must be heated by heat guns to the target temperature.

The targeting temperature of air inside of thermal chamber is the designated ambient temperature (T_{front} /T_{rear}) based on testing scenarios. It takes longer for the headlamp surface to reach the designated temperature than air. The experiment initiates when two starting criteria are met:

- Front and rear section of thermal chamber reached target temperature (T_{front} /T_{rear}) .
- Front and rear headlamp housing surface temperature (T3 – T8) are within ±5°C of the target temperature.

There are two types of stopping criteria for the thermal chamber experiment: safety stops and quasi-steady-state stops.

Safety Stop means the experiment must abort to prevent permanent damage to the testing apparatus, including thermal chamber and LED headlamp.

The thermal chamber wall is made of expanded polystyrene foam (EPF). When the temperature increases, EPF may deform, creating panel gaps which lose the thermal insulation and causing error for the experiment. Furthermore, during the high temperature testing, EPF creates an odor which may not be safe to inhale. Therefore, it is important to monitor the temperature and condition of EPE. During the 50°C / 85°C scenario, the EPF starts to deform and unable to maintain the testing temperature, therefore, the experiment must abort.

The maximum T_j of the testing LED is 130°C. Exceed the maximum T_j may cause irreversible damage. Since direct measurement of T_j is not feasible during system-level testing, the heatsink center temperature (located above the LED) is used as a proxy. To prevent irreversible damage of the testing LED, the experiment stops when the heatsink center temperature reaches 105°C.

If there are no safety concerns, the experiment continues until the system reaches quasi-steady-state conditions. At quasi-steady-state, any fluctuations in temperature are minimal and do not significantly affect the system's overall behavior. The quasi- steady-state is defined as a rate of temperature change (dT/dt) of less than 0.1°C/min.

Experiment Procedures

1. Remove the top cover of the thermal chamber. Connect the headlamp to the power supply and attach the wires to the experimental headlamp and the "dummy headlamp" according to the specified testing scenarios. Ensure all thermocouples are securely positioned and in proper contact with their designated surfaces.

2. Launch the Chrysler Diagnostic Tool software. Connect it to the SLM, enable the LB LEDs, and disable all other lights (e.g., DRL, position lights). Verify that the headlamp is operating correctly.

3. Activate the data collection software and confirm stable temperature readings from all 14 thermocouples.

4. Turn off the headlamp and allow the LEDs to stabilize at ambient temperature.

5. Install the thermal chamber's top cover. Seal any gaps with tape to ensure the chamber is airtight.

6. If it is the initial experiment of the day, calibrate the camera-based photometry system.

7. Install the heat guns on the top cover. Set the target temperature and switch the heat guns to the "LOW" setting.

8. Monitor the headlamp housing surface temperature readings (T3 – T8) until the thermal chamber reaches the starting criteria.

9. Configure the screen capture tool to record screenshots of luminous flux readings at 30-second intervals.

10. Create a folder for all data collection files, including screen recordings, temperature logs, and light measurement records.

11. Turn on the headlamp to begin the experiment. Start recording temperature and luminous flux data.

12. Monitor the LED heatsink thermocouple temperature (T9 & T11). Terminate the experiment immediately if the temperature exceeds the predefined stopping criteria.

13. Once the experiment reaches the defined quasi-steady-state conditions ($\frac{dT}{dt} < 0.1°\mathrm{C/min}$), stop the data recordings, and turn off the headlamp. Save the data recordings.

14. Deactivate the heat guns and disconnect them from the power source.

15. Open the top lid of the thermal chamber to cool down the headlamp. Inspect the placement of thermocouples and the integrity of wiring connections. Be caution with hot air and surface of experiment apparatus.

16. Once the thermal chamber and LEDs are cooled, adjust the wiring and all experimental setups in preparation for the next testing scenario.

Appendix C LUMINOUS FLUX REGRESSION MODEL

Figure C.1 and C.2 shows the relationship between LED luminous flux and heatsink center temperature of LB1 and LB2. As the heatsink temperature increases, the luminous flux of the LED decreases, exhibiting a downward trend due to natural derating. These relationships are modeled using second-degree polynomial regression equations, which allow for interpolation of luminous flux at various temperatures within the tested range.

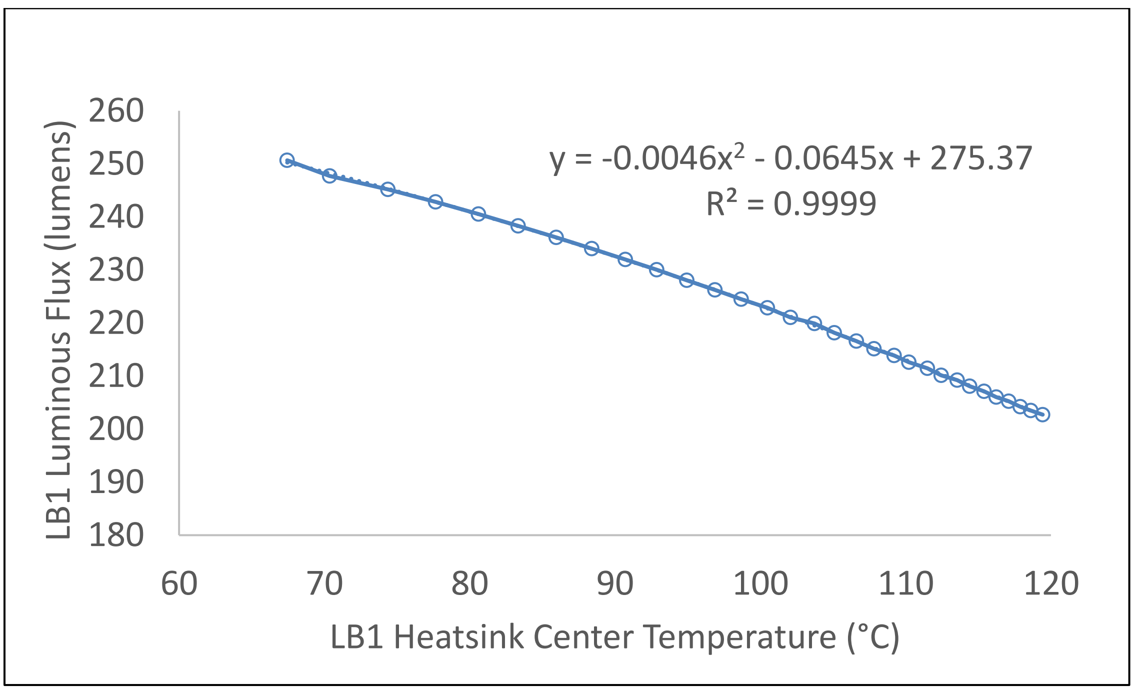

Figure C.1 Regression model of LB1 luminous flux as a function of heatsink center temperature

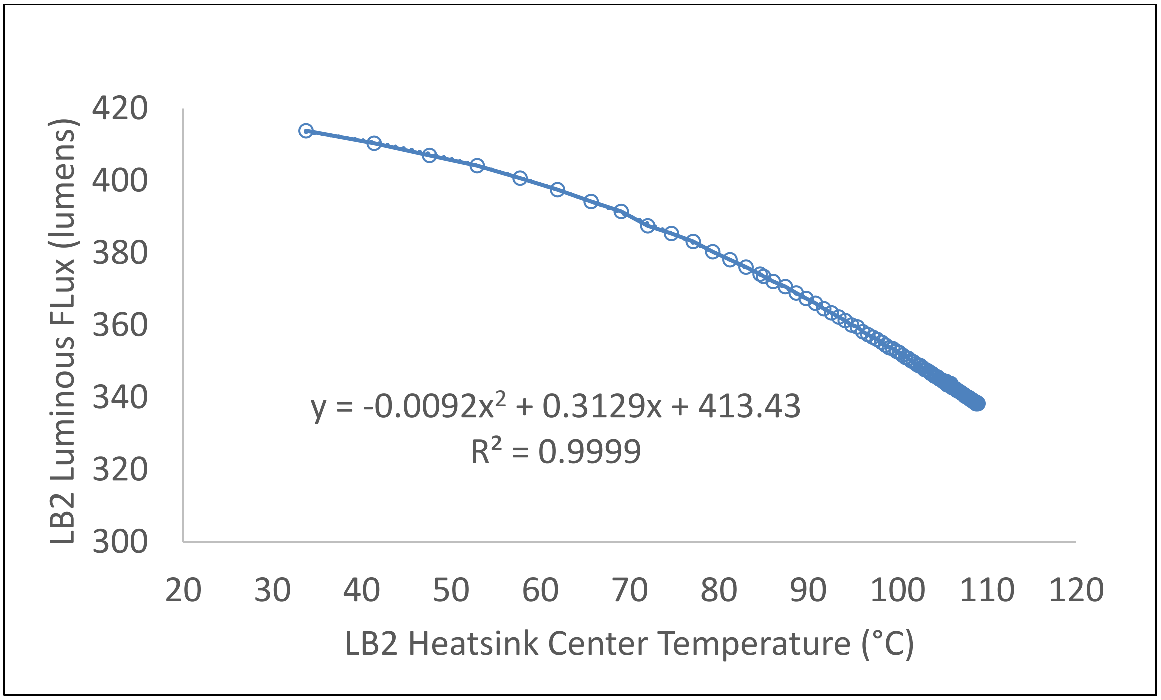

Figure C.2 Regression model of LB2 luminous flux as a function of heatsink center temperature

The regression equation for LB1 is given by:

$$\Phi_{LB1} = -0.0046 T_{LB1\ heatsink}{}^{2} - 0.0645 T_{LB1\ heatsink} + 275.37 \qquad (B.1)$$

$$T_{LB1\ heatsink}(°C) \in [67°C, 120°C]$$

where $T_{LB1\ heatsink}$ is the LB1 heatsink center location temperature, measured in degrees Celsius (°C), and the temperature range for LB1 is $T_{LB1\ heatsink}$∈[67°C,120°C].

Similarly, the relationship for LB2 is expressed as:

$$\Phi_{LB2} = -0.0092\, T_{LB2\ heatsink}{}^{2} + 0.312\, T_{LB2\ heatsink} + 413.43 \qquad (B.2)$$

$$T_{LB2\ heatsink} \in [30°C, 110°C]$$

These polynomial equations provide an interpolation, allowing for the calculation of luminous flux values at any temperature within the specified ranges. The second-degree polynomial models capture the non-linear relationship between temperature and luminous flux, offering a reasonably accurate representation of the observed behavior.

The coefficient of determination (R^2) values indicates the accuracy of the fit. The R^2 value for both LB1 and LB2 regression model is 0.9999, indicating an almost perfect fit between the experimental data and the regression curve. This high R^2 value suggests that the polynomial model accurately describes the relationship between the heatsink temperature and luminous flux for LB1 and LB2, with minimal variance in the data.

Appendix D THERMAL IMAGE OF LED

During the LED temperature measurement experiment, thermal images of the heatsink's upper and lower surfaces were captured when the LED temperature reached quasi-steady-state. However, the accuracy of the temperature readings is uncertain due to potential instrument error and the thermal camera's settings. As a result, the thermal images are primarily used for visualizing the temperature distribution of heatsink surface.

Thermal images of the heatsink were taken under the following temperature conditions:

- Room temperature condition
- 20°C /20°C, Fan Off case
- 50°C /50°C, Fan Off case

The thermal images are presented in Figures D.1 to D.5.

Room Temperature Condition

Figure D.1 Heatsink upper surface thermal image [room temperature]

Figure D.2 Heatsink lower surface thermal image [room temperature]

20°C /20°C, Fan Off Case

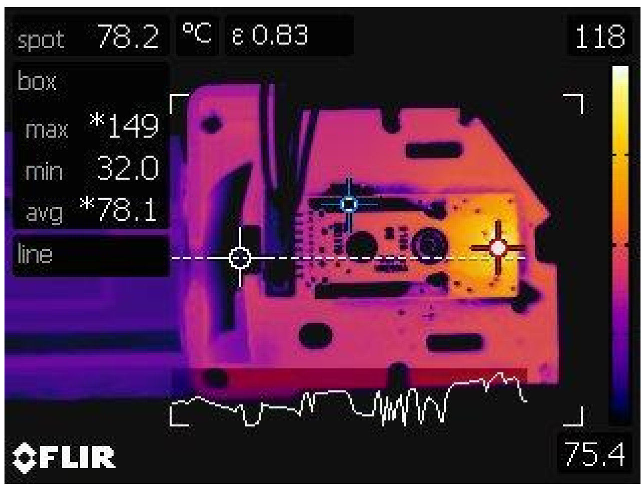

Figure D.3 Heatsink lower surface thermal image [20°C /20°C, Fan Off]

50°C /50°C, Fan Off Case

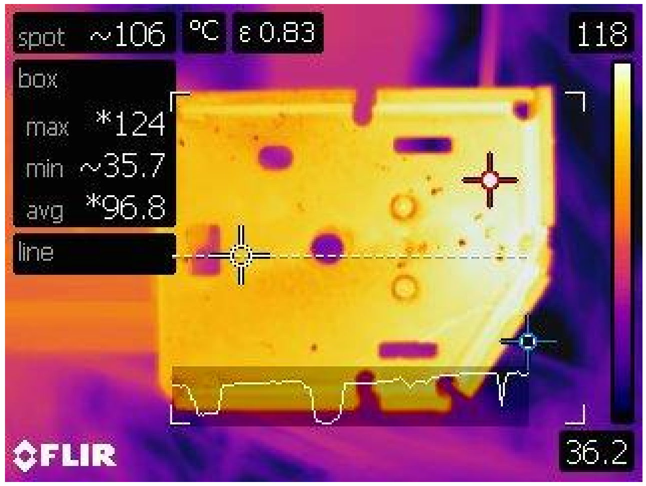

Figure D.4 Heatsink upper surface thermal image [50°C /50°C, Fan Off]

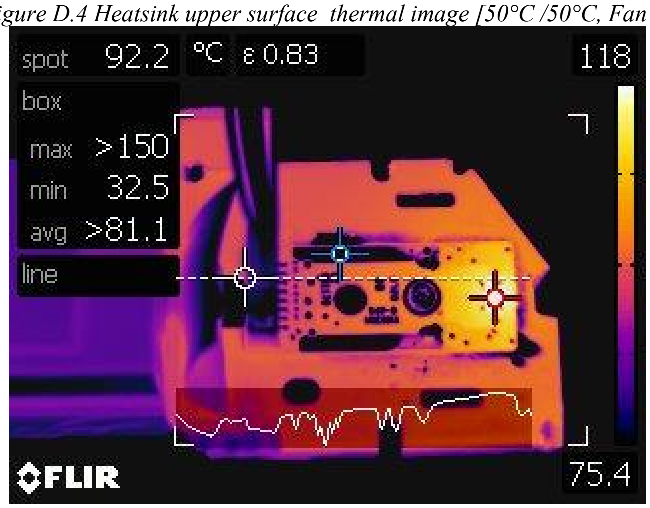

Figure D.5 Heatsink lower surface thermal image [50°C /50°C, Fan Off]

Table D.1 lists the LED and heatsink temperature measurement results obtained from the thermal camera readings. For high LED temperatures that exceeded the thermal camera's range, measurements were taken using a K-type thermocouple.

Several thermal camera settings contribute to potential inaccuracies in the readings, including:

- The emissivity of the heatsink
- Ambient humidity
- Focal distance
- Angle
- Thermal camera temperature calibration

These uncertainties may result in deviations from the actual temperature values.

Table D.1 LED and heatsink temperature measurement results using thermal camera and K-type thermocouple

Experiment case	**Heatsink in the room environment**	**20°C /20°C, Fan Off**	**50°C /50°C, Fan Off**
Heatsink surrounding air temperature	20.0°C	50°C	77°C
LED temperature	108°C	150°C*	172.5°C*
Heatsink center	60.6°C	86.6°C	111.3°C
Heatsink corner	-	77.6°C	101.5°C

**: Measured by K-type thermocouple*